Thesis

# Theoretical study on spin and orbital fluctuations and pairing mechanisms of iron-based superconductors

Jun Ishizuka

Graduate School of Science and Technology,

Niigata University

# Contents

# Chapter 1

# Overview

The discovery of the iron-based superconductors [1] has triggered an intense research effort to investigate their electronic state and superconducting mechanism. Numerous experiments and theories have been reported and various issues remain under debate. In present chapter, we provide an overview of the iron-based compounds. In Sec. 1.1, we explain experimental results of the iron-based superconductors. We introduce FeSe system in Sec. 1.1.5, which is helpful to read Chap. 3 and Chap. 4. In Sec. 1.2, we illustrate theoretical studies on the superconducting states and the pairing mechanism in iron-based superconductors.

## 1.1 Experiment

### 1.1.1 Phase diagram

Phase diagram for $SmFeAsO_{1-x}F_x$ and $SmFeAsO_{1-x}H_x$ determined by the resistibly measurements is shown in the top panel of Fig. 1.1 [2]. Note $F^-(H^-)$ substitution to the site of $O^{2-}$ ions indicates the electron-doping. SmFeAsO on doping $x = 0$ shows the structural transition at $T_s \sim 150\,\mathrm{K}$, and stripe-type antiferromagnetic order at $T_N \sim 140\,\mathrm{K}$. For increase $x$, two transitions are gradually suppressed, and vanished at $x = 0.05$. The superconductivity occurs in $0.03 < x < 0.46$, and shows the maximum transition temperature $T_c \sim 55\,\mathrm{K}$ at $x \sim 0.2$. For LaFeAsO, similar $T$ versus $x$ phase diagram is observed in low doping region. $T_c$ first increases for increasing $x$, and then decreases slightly before rising again. The maximum $T_c \sim 36\,\mathrm{K}$ is realized at $x \sim 0.3$, having a double superconducting dome. An antiferromagnetic phase is observed for $x \gtrsim 0.50$, and then the superconducting dome lies between two antiferromagnetic phases.

### 1.1.2 Spin fluctuation

Ning *et al.* [4] using the nuclear magnetic resonance found that the spin relaxation rate $1/T_1T$ in $Ba(Fe_{1-x}Co_x)_2As_2$ is enhanced toward $T_N$ (see left panel of Fig. 1.2), and the enhancement is suppressed by the electron doping. The superconductivity is realized at $x = 0.05$, and $T_c \sim 22\,\mathrm{K}$ at $x = 0.08$. The spin fluctuation is indeed enhanced near the superconducting phase. However, it did not grow at $x = 0.14$, where the superconductivity is vanished. It indicates that the spin fluctuation has deeply influence on evolution of the superconductivity. When the superconducting pairing is mediated by the spin fluctuation, it is known that the imaginary part of the dynamical

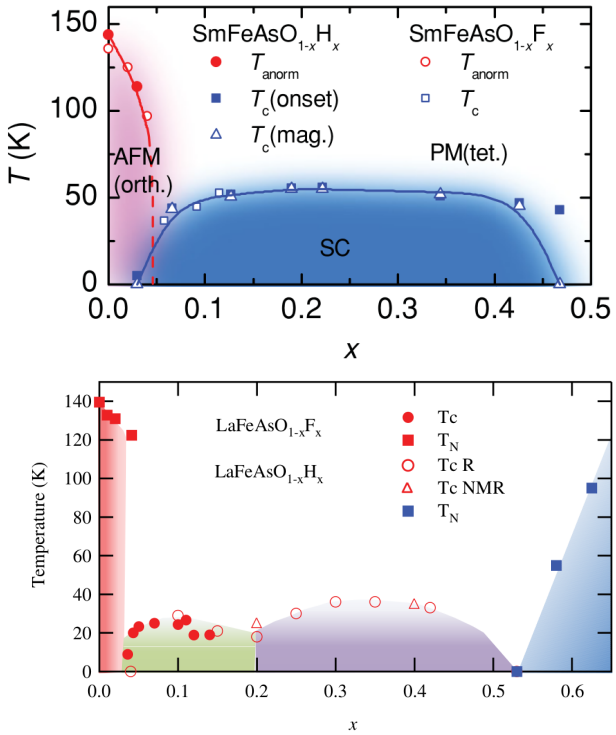


Figure 1.1: (top panel) Phase diagram for $SmFeAsO_{1-x}F_x$ and $SmFeAsO_{1-x}H_x$ determined by the resistibly measurements [2]. (bottom panel) Phase diagram for $LaFeAsO_{1-x}F_x$ and $LaFeAsO_{1-x}H_x$ determined by the resistibly and the nuclear magnetic resonance measurements [3].

spin susceptibility $\chi^s(\boldsymbol{q},\omega)|_{\boldsymbol{q}=\boldsymbol{Q}}$ ($\boldsymbol{Q}$ is the nesting vector) shows a prominent resonance peak. Indeed, this peak is observed in the copper oxide superconductors and the heavy-electron superconductors [5, 6, 7], which have been known to be the spin-fluctuation-mediated superconductors. It is shown in the right panel of Fig. 1.2 that $\chi^s(\boldsymbol{q},\omega)|_{\boldsymbol{q}=(\pi,\pi)}$ [$\boldsymbol{q}=(\pi,0)$ for the Fe-Fe axis] has a hump peak at the low energy state in the superconducting phase.

### 1.1.3 Orbital fluctuation

The ultrasonic measurement can observe charge or orbital fluctuations via the temperature dependences of shear elastic constants. Fernandes *et al.* found that the shear elastic constant of $C_{66}$ reveals considerable softening below the room temperature [9, 10, 11]. Generally, the shear elastic constant associated with an elastic strain as an external field is defined as $C_{66} = \rho\tilde{v}_{\rm ac}^2$. Here, $\rho$ is density, $\tilde{v}_{\rm ac}$ is the velocity of renormalized acoustic phonon. The phenomenon "softening" is a decrease in the velocity by decreasing temperature. When there is the electron-phonon interaction $-g_{\rm ac}(\boldsymbol{k})\hat{O}_{x^2-y^2}(\boldsymbol{k})\varepsilon_\theta(\boldsymbol{k})$ between the acoustic phonon inducing the orthorhombic strain and the electronic charge-quadrupole, comparing the Green's function of the acoustic phonon and the quadrupole

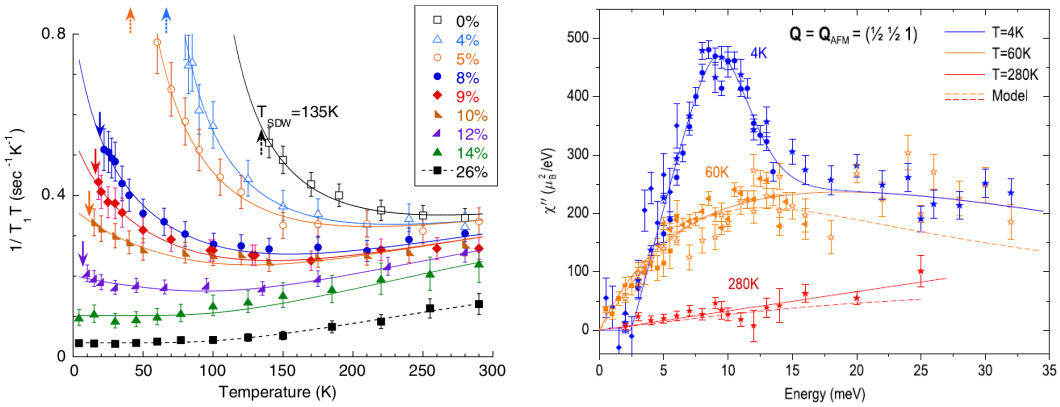


Figure 1.2: (left panel) Temperature dependence of the spin relaxation rate $1/T_1T$ in $Ba(Fe_{1-x}Co_x)_2As_2$ [4]. (right panel) the dynamical spin susceptibility in $BaFe_{1.85}Co_{0.15}As_2$ determined by the inelastic neutron scattering experiment [8].

susceptibility $\chi_{x^2-y^2}(\boldsymbol{k},\omega)$, a inverse of the shear elastic constant is written as

$$C_{66}^{-1} = C_{66,0}^{-1}[1 + \lim_{\boldsymbol{k}\to\boldsymbol{0}} \frac{2g_{\rm ac}^2(\boldsymbol{k})}{\omega_0(\boldsymbol{k})}\chi_{x^2-y^2}(\boldsymbol{k},0)], \tag{1.1}$$

where $g_{\rm ac}$ is the electron-phonon coupling constant, $\hat{O}_{x^2-y^2}$ is the quadrupole operator of $x^2-y^2$ quadrupole, $\varepsilon_\theta$ is the external strain, $\chi_{x^2-y^2}$ is the quadrupole susceptibility combined with the acoustic phonon. Therefore, $\chi_{x^2-y^2}(\boldsymbol{k},\omega)|_{\omega=0,\boldsymbol{k}\to 0}$ corresponds to the inverse of the shear elastic constant $C_{66}^{-1}$.

Alternatively, Yoshizawa *et al.* [12] using the ultrasonic measurement for several doping rate found that the softening of $C_{66}$ toward the structural transition temperature $T_s$ is suppressed by the carrier doping, resulting in the appearance of the superconductivity (see left panel of Fig. 1.3). Note this softening is observed even for $x = 0.08$ with $T_c > 0\,\mathrm{K}$ and $T_s < 0\,\mathrm{K}$. This indicates that the fluctuation same as the diverged orbital fluctuation toward the structural transition is also enhanced toward the superconducting phase. Note the hardening behavior in the superconducting phase may be due to the appearance of the energy gap on the Fermi surface. Moreover, Phonon softening near the $T_s$ in $BaFe_2As_2$ is observed by inelastic x-ray scattering [13] (see also an inelastic neutron scattering study [14]).

### 1.1.4 Electronic correlation effect on single-particle state

In the potassium- (hole-) doped $Ba_{1-x}K_xFe_2As_2$ system, a large deviation between the angle-resolved photoemission spectroscopy (ARPES) spectral intensity and LDA band dispersion was observed by Ding *et al.* [15] (see Fig. 1.4). The ARPES spectral intensity could not be deduced from rescaling the LDA band structure (the gray solid line in the right panel), since the outer-hole band shows the significantly narrow spectral intensity. The estimated effective masses are $m_\beta^* \sim 9.0$, $m_\alpha^* \sim 4.8$, and $m_{\gamma,\delta}^* \sim 1.3$. Moreover, the heavily hole-doped superconductor $KFe_2As_2$ ($T_c \sim 3.5K$), which shows the huge Sommerfeld parameter for the electronic specific heat $\gamma \sim 103$ mJ mol$^{-1}$K$^{-2}$, reveals the

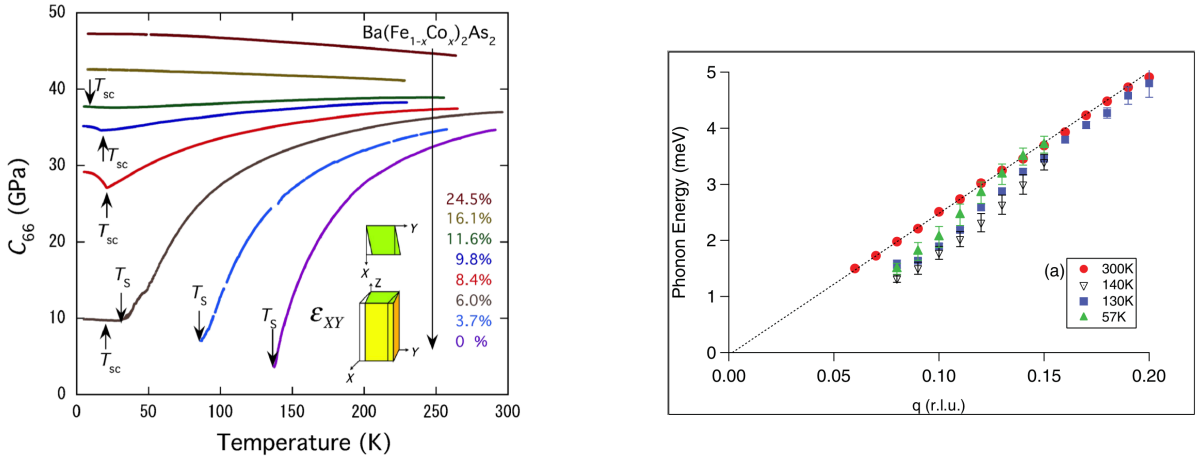


Figure 1.3: (left panel) Temperature dependence of the shear elastic constant $C_{66}$ in $Ba(Fe_{1-x}Co_x)_2As_2$ [12]. (right panel) Dispersion of the transverse acoustic phonon at 300 K, 140 K, 130 K, and 57 K in $BaFe_2As_2$ [13].

emergence of the heavy-electron superconductivity. In turn, Yi *et al.* [16] pointed out using the ARPES measurement in $K_xFe_{2-y}Se_2$ ($x = 0.76$, $y = 0.28$) that the band mainly composed of the $d_{xy}$ orbital component becomes to disappear by increasing temperature, which is understood as a temperature-induced crossover from a metallic state at low temperature to an orbital-selective Mott phase at high temperature. In the orbital-selective Mott phase, some orbitals are localized while others remain itinerant.

These band (orbital) dependence of the quasiparticle renormalization might be caused by the complexly tangled band structures of the strongly correlated Fe-3$d$ electrons.

### 1.1.5 FeSe system

FeSe shows the structural transition $T_s \sim 90$ K from tetragonal ($P4/nmm$) to orthorhombic ($Cmma$) as similar to another compound such as the 1111 systems and the 122 systems. The superconductivity is stabilized in orthorhombic phase at $T_c \sim 9$ K without the carrier doping. One of the most intriguing property is that the magnetic transition is absent down to the zero temperature. The strength of the antiferromagnetic fluctuation is very weak above the $T_s$, revealed by the NMR experiment (see the right panel of Fig. 1.6) [17]. The absence of the low energy spin fluctuation might be inconsistent with the spin-nematic scenario recognized as a mechanism of a structural transition [9]. Below $T_s$, it starts to increase toward $T_c$, and then the temperature dependence of $1/T_1T$ seems to be consistent with the spin fluctuation pairing.

Unusual correlation effects have been observed in FeSe [19]. In the high temperature above $T_s$, $\alpha$ and $\beta$ hole bands shallowly cross the Fermi level at $Z$ point, while the $\epsilon$ electron band has the large intensity at $M$ point. these three bands have mainly $d_{zx}$ or $d_{yz}$ orbital character. Note the degeneracy of the $d_{zx}$ and $d_{yz}$ orbitals are lifted by the spin-orbit interaction, and then only $\alpha$ hole pocket was observed at $\Gamma$ point as shown in Fig. 1.7 (g). The $\gamma$ hole band, which consists of the $d_{xy}$ orbital character, exists below the Fermi level $\sim -50$ meV at $Z$ point. In stark contrast, this hole band crosses the Fermi level in other iron-based superconductors. The effect of electronic correlations

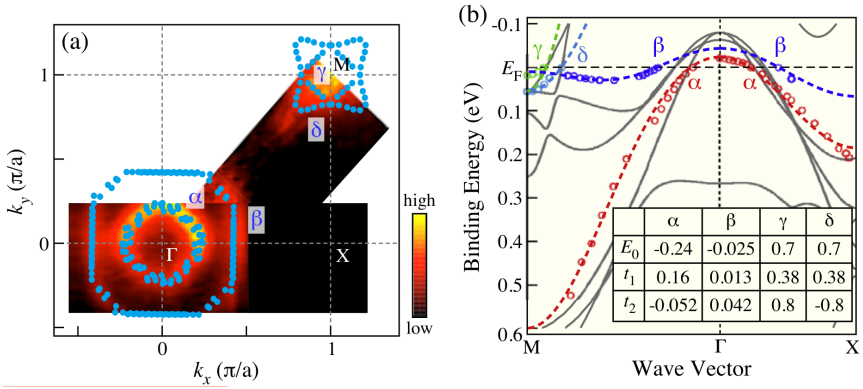


Figure 1.4: (left panel) Fermi surface in $Ba_{0.6}K_{0.4}Fe_2As_2$ obtained by the ARPES experiment [15]. (right panel) Energy spectrum of $Ba_{0.6}K_{0.4}Fe_2As_2$ [15]. The band dispersion of the LDA calculation normalized by a factor of 2 is depicted as gray solid line.

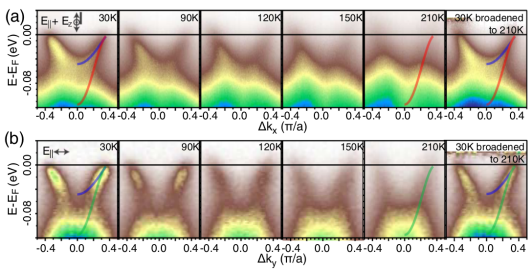


Figure 1.5: Energy spectrum of $K_xFe_{2-y}Se_2$. red solid line, green solid line, and blue solid line represent $d_{zx}$, $d_{yz}$, and $d_{xy}$ orbital, respectively [16].

was estimated by comparing band calculations with the ARPES spectral intensity in the $A$-$Z$-$A$ line. The effective masses for $\alpha$, $\beta$, and $\gamma$ bands are $\sim 3.2$, 2.1, and 8, respectively. In turn, the extremal Fermi surface areas at the low temperature have been studied by quantum oscillation measurement [19]. Four quantum oscillation frequencies lower than 1 kT was detected, which are smaller than the one of other iron-based compounds. Two-dimensional natures of the frequencies in Fig. 1.7(e) are consistent with the ARPES studies. Moreover, the $F_3$ frequency predicts the existence of an electron band in addition to the $\epsilon$ band observed in the ARPES measurement. Suzuki *et al.* [20] pointed out as shown in Fig. 1.7(f)-(h) that the orbital order has momentum-dependent sign-inversion as $E_{yz}(\Gamma) - E_{zx}(\Gamma) \sim -10$ meV and $E_{yz}(M) - E_{zx}(M) \sim +50$ meV.

Phase diagram as a function of pressure in FeSe determined by the resistibly measurements is shown in Fig. 1.8 [21]. $T_s$ is quickly suppressed by pressure up to $P \sim 1$ GPa, while $T_m$ is stabilized in a wide pressure region ($1 < P < 6$ GPa) with a dome shape for $\sim 45$ K at $P \sim 4.8$ GPa. $T_c$ can be first enhanced by pressure, and then drops down slightly before arising again, and finally reaches to $\sim 37$ K at $P \sim 6.5$ GPa. Several issues remain under debate, for instance, the superconductivity and the antiferromagnetic phase are in coexistence or not. The four-rotational symmetry of the crystalline structure is broken in the antiferromagnetic phase in a low $T$ at least.

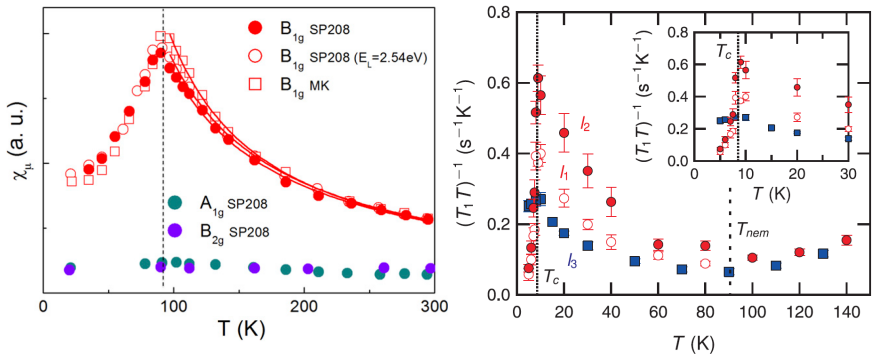


Figure 1.6: (left panel) Temperature evolution of the Raman nematic susceptibility determined by the Raman scattering measurement in FeSe [18]. (right panel) Temperature dependence of the spin-lattice relaxation rate $1/T_1T$ in FeSe [17].

## 1.2 Theory

### 1.2.1 First-principles calculation

In this subsection, we provide an overview of the band structure derived from the first-principles band calculation, which is essential for a discussion of the electronic state and the superconductivity.

All iron-based superconductors have the same conduction plane composed by irons-pnictogens or irons-chalcogens layer. Thus, the electronic structure and the Fermi surface are roughly similar to the other compounds [22, 23, 24, 25, 26, 27, 28, 29, 30, 31, 32]. As shown in Fig. 1.9, the ten conduction bands are composed of the iron $3d$ orbitals located near the Fermi level, and are tangled intricately. Note there are two iron atoms in a unit cell. The valence bands below the conduction bands have pnictogen or chalcogen $p$ orbitals. Note the 1111 systems such as LaFePO and LaFeAsO has twelve bands since the oxygen $p$ orbitals contribute to the valence bands. The entanglement of the conduction bands is attributable to the orbital degrees of freedom and the tetrahedral structure of irons-pnictogens (-chalcogens) layer. In the tetrahedral structure, the crystalline electric field effects at iron sites are comparably smaller than the perovskite structure, and then energy splitting is considerably weak. In particular, the $d_{xy}$, $d_{zx}$, and $d_{yz}$ orbitals makes the bands at low energy region, while $d_{3z^2-r^2}$ and $d_{x^2-y^2}$ has large component at high energy region in conduction bands.

Miyake *et al.* [32] derived the low-energy $d$, $dp$ (for the 122, 111, and 11 systems), $dpp$ (for the 1111 systems) models by a combined constrained random-phase approximation (cRPA) and maximally localized Wannier functions method. The extent of the Wannier functions are significantly large values in the $d$ model, $\langle r^2\rangle - \langle r\rangle^2 = 5.37\text{Å}^2$ for $d_{x^2-y^2}$ orbital of LaFeAsO, for instance. Moreover, the Wannier orbitals show strongly orbital-dependent spreads in the $d$ models, the most extended orbital is twice larger than the smallest one for LaFeAsO. All $d$ orbitals for the $d$ models contain considerable pnictogen or chalcogen $p$ orbital components, and then the hybridization makes the Wannier functions delocalized and anisotropic. In stark contrast, the spread of Wannier orbitals are efficiently suppressed in the $dp$ or $dpp$ models with the small orbital dependence. Moreover, the constructions of Wannier orbitals are similar to the atomic orbitals. Next let us turn to the screened Coulomb interaction of the $dp$ or $dpp$ models. Fig. 1.10 obtained by Miyake *et al.* [32] shows the on-site screened Coulomb interaction $U$ and screened exchange interaction $J$. The average of the

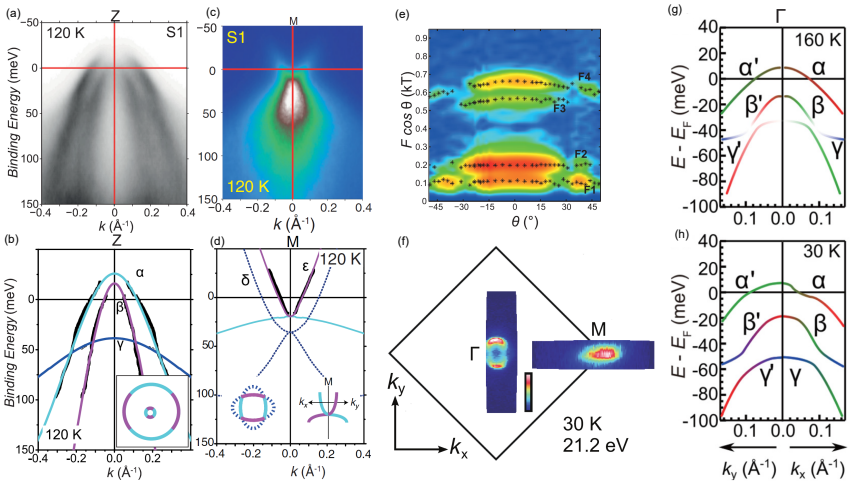


Figure 1.7: ARPES spectral intensities and extracted band dispersion of FeSe along high symmetry direction (a)-(b) $A$-$Z$-$A$ and (c)-(d) $\Gamma$-$M$-$\Gamma$ obtained by Watson *et al.* [19]. (e) Quantum oscillation frequencies as a function of angle $\theta$ of applied magnetic field with respect to the $c$ axis [19]. (f) Fermi surface of FeSe in orthorhombic phase determined by ARPES study on detwinned single crystal obtained by Suzuki *et al.* [20]. (g)-(h) Schematic band dispersions at $T = 160\,\mathrm{K}$ and $30\,\mathrm{K}$ obtained by ARPES study on detwinned single crystal [20].

intra-orbital terms $\bar{U}$ is smallest in the 1111 systems, and the value increases in the 111 and 11 systems. However, the ratio $\bar{J}/\bar{U}$ is largest in the 1111 systems, and is considerably smaller in 122 and 11 systems, $\bar{J}/\bar{U} = 0.134$ for LaFeAsO and $\bar{J}/\bar{U} = 0.0945$ for FeSe, for instance. The orbital dependences are smaller than the $d$ models, and indicate the isotropic Coulomb matrices, namely $\bar{U} = \bar{U}' + 2\bar{J}$ approximately satisfied.

### 1.2.2 Pairing mechanism

Since the superconductivity was found in the proximity of the structural transition and the antiferromagnetic ordered phase in many of the iron-based superconductors, spin driven scenario [33, 34, 35, 36, 37, 38, 39, 40, 41, 42, 43, 44, 45, 46, 47, 48] and orbital driven scenario [9, 49, 50, 51, 52, 53, 54, 55, 56, 57, 58] have been proposed. The spin configuration indicates the stripe-type arrangement, and is corresponding to the nesting wave vector $\boldsymbol{Q}_{\mathrm{AF}} = (\pi, 0), (0, \pi)$ between the hole and electron Fermi surface. The superconducting state is obtained by solving the gap equation, which is written by the effective pairing interaction $V(\boldsymbol{q})$. When the spin fluctuation with wave vector $\boldsymbol{q} \sim \boldsymbol{Q}_{\mathrm{AF}}$ mediates the pairing, $V(\boldsymbol{q})$ is repulsive, and results in the sign change of the gap function. Mazin *et al.* [33] immediately proposed this "$s_{\pm}$-wave" pairing mediated by spin fluctuation, where the microscopic calculation from first-principles band calculation on the $s_{\pm}$ state was presented by Kuroki *et al.* [34] for the first time. In the case of spin fluctuation pairing, superconducting gap involves sign change of the order parameter, and hence cannot gain the pairing interaction on a part of Fermi surface. This yields a direct $T_c$ decrease. However, when Fermi surface consists of disconnected pieces such as iron-based superconductors, the sign change can take place without any nodes, and then high-$T_c$ pairing can be expected. This mechanism has been recognized in the early stage of high-$T_c$ mech-

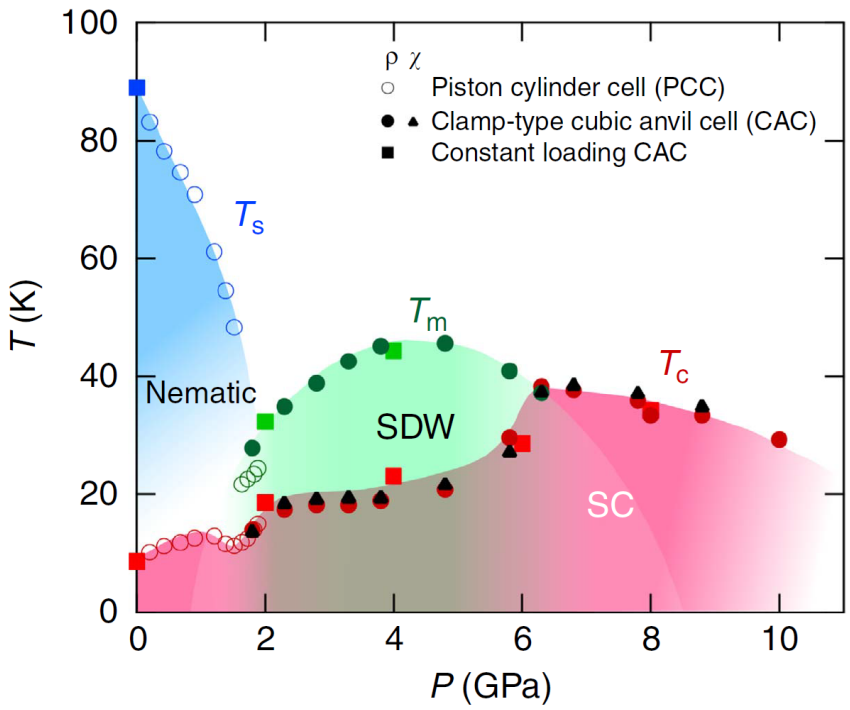


Figure 1.8: Pressure versus temperature phase diagram in FeSe determined by the resistibly measurements [21].

anism [59, 60]. Moreover, $s_{\pm}$ pairing is consistent with the measurement of low-energy excitation, suggesting the node-less gap structure and the low-energy spin response. However, It seems to be inconsistent with the impurity scattering experiment, since $s_{\pm}$ is fragile against the non-magnetic impurity.

Alternatively, Yanagi *et al.* [52] found that the $s_{\pm}$-pairing is mediated by the magnetic fluctuation near the antiferromagnetic order for $U > U'$ (here, $U$ and $U'$ is the intra- and inter-orbital Coulomb interaction, respectively), while the $s_{++}$-pairing is mediated by the orbital fluctuation near the ferro-orbital order for $U < U'$. Note the $s_{++}$-pairing without the sign change of the gap function is robust against the non-magnetic impurity, consistency with experiment. Although the region of $U < U'$ is unrealistic parameter, they considered the electron-phonon coupling $g$ with the orthorhombic mode [54], which directly coupled with the softening of $C_{66}$ observed in ultrasonic experiment. The ferro-orbital fluctuation for $\boldsymbol{q} \sim \boldsymbol{0}$ was found to be enhanced by this interaction $g$ [54] and/or the mode-coupling [51, 55], where the antiferro-orbital fluctuation for $\boldsymbol{q} \sim \boldsymbol{Q}_{\mathrm{AF}}$ was also enhanced owing to the nesting effect [54, 51, 55, 50, 53]. When $V(\boldsymbol{q}) < 0$ for $\boldsymbol{q} \sim \boldsymbol{Q}_{\mathrm{AF}}$ mediated by the antiferro-orbital fluctuation overcomes the repulsive one by the antiferromagnetic fluctuation for the same wave vector, the $s_{++}$-wave pairing was found to be realized with the cooperation of $V(\boldsymbol{q}) < 0$ for $\boldsymbol{q} \sim \boldsymbol{0}$ by the ferro-orbital fluctuation [54, 51, 55, 50, 53]. At present, it is unclear which fluctuation is dominant for $\boldsymbol{q} \sim \boldsymbol{Q}_{\mathrm{AF}}$, that is crucial in determining the $s_{\pm}$ or $s_{++}$ pairing, since the antiferro-orbital fluctuation has not been explicitly observed in experiments so far [61]. In either case, the antiferromagnetic and the antiferro-orbital fluctuations compete in the pairing interaction, and hence result in a suppression

of $T_c$ as compared to the case with either fluctuation alone.

We proposed another mechanism of the ferro-orbital fluctuation enhancement [62] due to the inter-site Coulomb interaction between Fe $d$ and pnictogen $p$ electrons. A recent experiment has indeed provided evidence for strong coupling of Fe and pnictogen orbital polarizations (OPs) [63]. Then, we employ realistic 16 band $d$-$p$ model which explicitly includes Fe $3d$ and As $4p$ orbitals reproducing the band structure of LaFeAsO and has been extensively studied focusing on the effects of the $d$-$d$ interaction [64, 52] and/or the electron-phonon interaction [53, 54, 58]. The effect of the $d$-$p$ interaction has also been investigated and found to enhance the charge fluctuation which mediates the $s_{\pm}$- or the $s_{++}$-wave pairing depending on the parameters [65]. However, the interaction between the Fe and As OPs depending on relative direction of $d$ and $p$ orbitals has not been considered there [see Fig. 1.11(A)]. We find that the $d$-$p$ OP interaction enhances the ferro-orbital fluctuation responsible for the $C_{66}$ softening without enhancing the antiferro-orbital one resulting in the $s_{\pm}$-wave superconductivity in collaboration with the antiferromagnetic fluctuation enhanced by the $d$-$d$ interaction [see Fig. 1.11(B) and (C)]. In this case, the experimentally observed two fluctuations cooperatively enhance $T_c$ without any competition by virtue of the $\boldsymbol{q}$-space segregation.

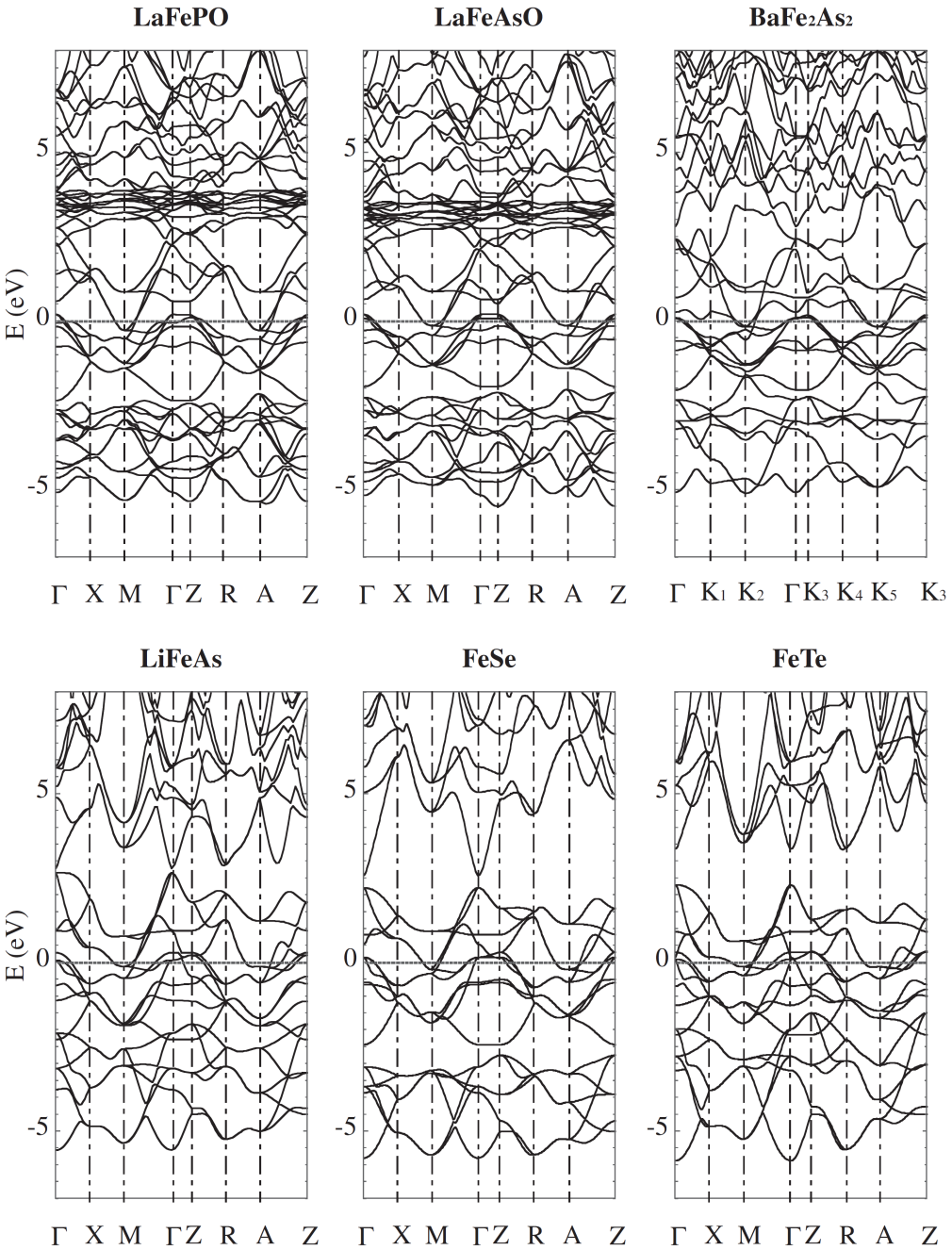


Figure 1.9: Band structure of iron-based superconductors obtained by Miyake *et al.* [32].

| LaFePO | $U$ | | | | | | $J$ | | | | |
|---|---|---|---|---|---|---|---|---|---|---|---|
| | $xy$ | $yz$ | $3z^2-r^2$ | $zx$ | $x^2-y^2$ | | $xy$ | $yz$ | $3z^2-r^2$ | $zx$ | $x^2-y^2$ |
| $xy$ | 4.72 | 3.09 | 2.97 | 3.09 | 3.47 | $xy$ | | 0.63 | 0.72 | 0.63 | 0.35 |
| $yz$ | 3.09 | 3.99 | 3.25 | 2.85 | 2.81 | $yz$ | 0.63 | | 0.43 | 0.54 | 0.55 |
| $3z^2-r^2$ | 2.97 | 3.25 | 4.25 | 3.25 | 2.72 | $3z^2-r^2$ | 0.72 | 0.43 | | 0.43 | 0.62 |
| $zx$ | 3.09 | 2.85 | 3.25 | 3.99 | 2.81 | $zx$ | 0.63 | 0.54 | 0.43 | | 0.55 |
| $x^2-y^2$ | 3.47 | 2.81 | 2.72 | 2.81 | 3.71 | $x^2-y^2$ | 0.35 | 0.55 | 0.62 | 0.55 | |
| LaFeAsO | $U$ | | | | | | $J$ | | | | |
| | $xy$ | $yz$ | $3z^2-r^2$ | $zx$ | $x^2-y^2$ | | $xy$ | $yz$ | $3z^2-r^2$ | $zx$ | $x^2-y^2$ |
| $xy$ | 4.66 | 3.09 | 2.99 | 3.09 | 3.57 | $xy$ | | 0.63 | 0.74 | 0.63 | 0.37 |
| $yz$ | 3.09 | 4.08 | 3.31 | 2.90 | 2.91 | $yz$ | 0.63 | | 0.45 | 0.56 | 0.59 |
| $3z^2-r^2$ | 2.99 | 3.31 | 4.33 | 3.31 | 2.81 | $3z^2-r^2$ | 0.74 | 0.45 | | 0.45 | 0.67 |
| $zx$ | 3.09 | 2.90 | 3.31 | 4.08 | 2.91 | $zx$ | 0.63 | 0.56 | 0.45 | | 0.59 |
| $x^2-y^2$ | 3.57 | 2.91 | 2.81 | 2.91 | 3.98 | $x^2-y^2$ | 0.37 | 0.59 | 0.67 | 0.59 | |
| $BaFe_2As_2$ | $U$ | | | | | | $J$ | | | | |
| | $xy$ | $yz$ | $3z^2-r^2$ | $zx$ | $x^2-y^2$ | | $xy$ | $yz$ | $3z^2-r^2$ | $zx$ | $x^2-y^2$ |
| $xy$ | 5.40 | 3.95 | 3.84 | 3.95 | 4.40 | $xy$ | | 0.68 | 0.78 | 0.68 | 0.39 |
| $yz$ | 3.95 | 5.19 | 4.33 | 3.86 | 3.81 | $yz$ | 0.68 | | 0.49 | 0.64 | 0.66 |
| $3z^2-r^2$ | 3.84 | 4.33 | 5.45 | 4.33 | 3.71 | $3z^2-r^2$ | 0.78 | 0.49 | | 0.49 | 0.75 |
| $zx$ | 3.95 | 3.86 | 4.33 | 5.19 | 3.81 | $zx$ | 0.68 | 0.64 | 0.49 | | 0.66 |
| $x^2-y^2$ | 4.40 | 3.81 | 3.71 | 3.81 | 4.97 | $x^2-y^2$ | 0.39 | 0.66 | 0.75 | 0.66 | |
| LiFeAs | $U$ | | | | | | $J$ | | | | |
| | $xy$ | $yz$ | $3z^2-r^2$ | $zx$ | $x^2-y^2$ | | $xy$ | $yz$ | $3z^2-r^2$ | $zx$ | $x^2-y^2$ |
| $xy$ | 5.98 | 4.60 | 4.49 | 4.60 | 5.14 | $xy$ | | 0.67 | 0.77 | 0.67 | 0.39 |
| $yz$ | 4.60 | 5.89 | 5.01 | 4.55 | 4.58 | $yz$ | 0.67 | | 0.48 | 0.63 | 0.67 |
| $3z^2-r^2$ | 4.49 | 5.01 | 6.08 | 5.01 | 4.46 | $3z^2-r^2$ | 0.77 | 0.48 | | 0.48 | 0.77 |
| $zx$ | 4.60 | 4.55 | 5.01 | 5.89 | 4.58 | $zx$ | 0.67 | 0.63 | 0.48 | | 0.67 |
| $x^2-y^2$ | 5.14 | 4.58 | 4.46 | 4.58 | 5.87 | $x^2-y^2$ | 0.39 | 0.67 | 0.77 | 0.67 | |
| FeSe | $U$ | | | | | | $J$ | | | | |
| | $xy$ | $yz$ | $3z^2-r^2$ | $zx$ | $x^2-y^2$ | | $xy$ | $yz$ | $3z^2-r^2$ | $zx$ | $x^2-y^2$ |
| $xy$ | 7.21 | 5.76 | 5.56 | 5.76 | 6.30 | $xy$ | | 0.74 | 0.83 | 0.74 | 0.42 |
| $yz$ | 5.76 | 7.25 | 6.18 | 5.75 | 5.73 | $yz$ | 0.74 | | 0.53 | 0.71 | 0.74 |
| $3z^2-r^2$ | 5.56 | 6.18 | 7.23 | 6.18 | 5.52 | $3z^2-r^2$ | 0.83 | 0.53 | | 0.53 | 0.83 |
| $zx$ | 5.76 | 5.75 | 6.18 | 7.25 | 5.73 | $zx$ | 0.74 | 0.71 | 0.53 | | 0.74 |
| $x^2-y^2$ | 6.30 | 5.73 | 5.52 | 5.73 | 7.09 | $x^2-y^2$ | 0.42 | 0.74 | 0.83 | 0.74 | |
| FeTe | $U$ | | | | | | $J$ | | | | |
| | $xy$ | $yz$ | $3z^2-r^2$ | $zx$ | $x^2-y^2$ | | $xy$ | $yz$ | $3z^2-r^2$ | $zx$ | $x^2-y^2$ |
| $xy$ | 6.09 | 4.81 | 4.60 | 4.81 | 5.42 | $xy$ | | 0.69 | 0.78 | 0.69 | 0.41 |
| $yz$ | 4.81 | 6.29 | 5.23 | 4.85 | 4.91 | $yz$ | 0.69 | | 0.50 | 0.69 | 0.72 |
| $3z^2-r^2$ | 4.60 | 5.23 | 6.18 | 5.23 | 4.69 | $3z^2-r^2$ | 0.78 | 0.50 | | 0.50 | 0.81 |
| $zx$ | 4.81 | 4.85 | 5.23 | 6.29 | 4.91 | $zx$ | 0.69 | 0.69 | 0.50 | | 0.72 |
| $x^2-y^2$ | 5.42 | 4.91 | 4.69 | 4.91 | 6.37 | $x^2-y^2$ | 0.41 | 0.72 | 0.81 | 0.72 | |

Figure 1.10: Effective Coulomb interaction at $3d$ orbitals on the same iron site in the *dpp* or *dp* model (in eV) obtained by Miyake *et al.* [32].

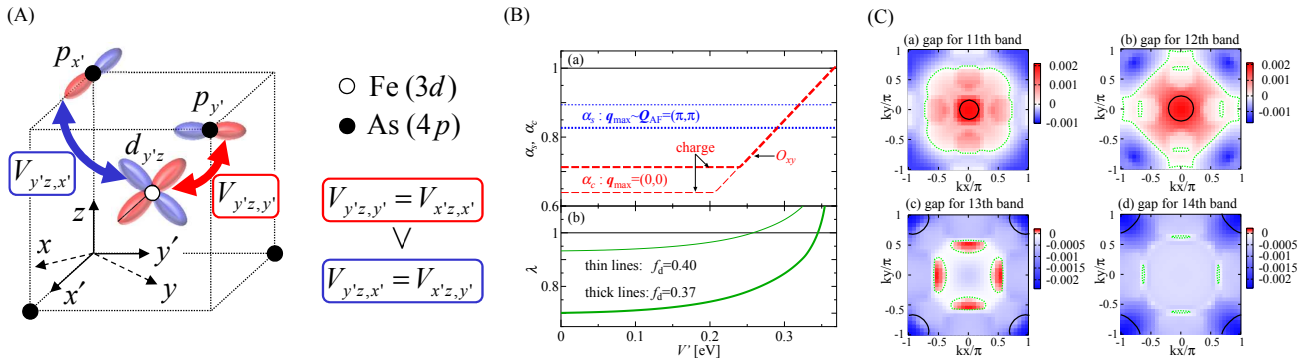


Figure 1.11: (A) The origin of the $d$-$p$ orbital polarization interaction $V' = (V_{x'z,x'} - V_{x'z,y'})/2$ due to the orbital dependence of Coulomb integrals between neighboring Fe and As sites with $V_{y'z,y'}(= V_{x'z,x'}) > V_{y'z,x'}(= V_{x'z,y'})$, where $x'$, $y'$ ($x$, $y$) refer to the direction along the nearest (second nearest) Fe-Fe bonds. (B) The spin and charge-orbital Stoner factors $\alpha_s$ (dotted lines) and $\alpha_c$ (dashed lines) for $\boldsymbol{q}_{\max}$ (a), and the eigenvalue of the Eliashberg equation $\lambda$ (b) for the $d$-$d$ interaction reduction factor $f_d = 0.37$ (thick lines) and $f_d = 0.40$ (thin lines) as functions of the $d$-$p$ orbital polarization interaction $V'$. (C) The band representation of the gap function $\hat{\Delta}(\boldsymbol{k}, i\pi T)$ for the 11th (a) and 12th (b) (hole) bands and the 13th (c) and 14th (d) (electron) bands in the Brillouin zone corresponding to two FeAs per unit cell for $f_d = 0.37$ and $V' = 0.345$eV with $\lambda = 1$, where black solid and green dotted lines represent the Fermi surfaces and the nodes of the gap functions, respectively. [62]

# Chapter 2

# Vertex correction and hole-$s_{\pm}$ state

In present chapter, we provide the detailed analysis of the five-orbital Hubbard model for iron-based superconductors, using the dynamical mean-field theory combined with the Eliashberg equation to clarify the local correlation effects on the electronic states and the superconductivity. In the specific case where the antiferromagnetic and antiferro-orbital fluctuations are comparably enhanced, the orbital dependence of the vertex function is significantly large, while that of the self-energy is small. It is in contrast to the antiferromagnetic fluctuation-dominated case where the vertex function (the self-energy) shows a small (large) orbital dependence. The orbital-dependent vertex function together with the nesting between the inner and outer hole Fermi surfaces results in the enhancement of the inter-orbital ferromagnetic fluctuation in addition to the antiferromagnetic and antiferro-orbital fluctuations. In this case, the hole-$s_{\pm}$-wave pairing with the sign change of the two-hole Fermi surfaces is mediated by the coexisting three fluctuations as expected to be observed in the specific compound LiFeAs.

The organization of this chapter is as follows. In Sec. 2.1, we overview a theoretical and experimental aspect in iron-pnictides. Present theoretical approach, called the DMFT+Eliashberg approach, is formulated in Sec. 2.2. The five-orbital Hubbard model is also reviewed. We review our previous study [66] about the spin or orbital fluctuation dominant case in Sec. 2.3 and 2.4, with additional results. In Sec. 2.5, we provide numerical results such as renormalization factor (Sec. 2.5.1), vertex function (Sec. 2.5.2), Stoner factor (Sec. 2.5.3), susceptibility (Sec. 2.5.4), and superconducting gap function (Sec. 2.5.5). The characteristic properties of strongly correlated electronic system are pointed out by means of multi-orbital physics in these subsections. Our main results are discussed in Sec. 2.5.2 and Sec. 2.5.5. In Sec. 2.5.2, we find the imbalanced renormalization of vertex functions with strong orbital dependence. In Sec. 2.5.5, we argue that these vertex function results in the novel superconducting pairing symmetry, called hole-$s_{\pm}$ state. We summarize the present chapter with some discussions in Sec. 2.6.

## 2.1 Introduction

Since the discovery of superconductivity with a high transition temperature in $LaFeAsO_{1-x}F_x$ [1], numerous investigations have been carried out for the iron-based superconductors categorized into four families: the 1111 system such as LaFeAsO, the 122 system such as $BaFe_2As_2$, the 111 system such as LiFeAs, and the 11 system such as FeSe [67, 68]. Most of the 1111 and 122 systems show the stripe-type antiferromagnetic (AFM) transition at $T_N$ and the tetragonal-orthorhombic structural transition

at $T_s$ just above $T_N$. Correspondingly, the AFM fluctuation diverges towards $T_N$ and the ferro-orbital (FO) fluctuation responsible for the softening of the elastic constant $C_{66}$ [9, 10, 12] diverges towards $T_s$. Therefore, the AFM and the FO fluctuations have been discussed as key ingredients for the pairing mechanisms.

In contrast to the systems mentioned above, the 111 system LiFeAs shows superconductivity without any structural transitions and magnetic orders [69]. The absence of the structural transition accompanied by elastic softening seems to be consistent with the above-mentioned FO fluctuation mechanism since the As-$p$ orbital weights on the FSs for LiFeAs are certainly smaller than those for the other systems exhibiting the structural transitions. Although the magnetic order is absent, the incommensurate magnetic fluctuation nearly to the AFM one was observed in the inelastic neutron scattering experiments [70, 71], which is well accounted for by the nesting between the hole and electron FSs observed in the angle-resolved photoemission spectroscopy (ARPES) experiment [72]. In addition, the FM fluctuation was also observed in the $\mu$SR measurement [73]. A recent NMR experiment also revealed the FM fluctuation for the 122 systems over a wide doping range [74]. Therefore, the existence of the FM fluctuation may be a common feature of iron-based superconductors, as predicted from the first-principles band calculation [33]. On the other hand, the existence of the AFO fluctuation has been suggested since the AFO-fluctuation-mediated superconducting gap structure on FSs is in good agreement with the experimental observations, while the AFM-fluctuation-mediated one is not [75]. Although the AFO fluctuation has not been explicitly observed experimentally so far, such fluctuation may be enhanced by electron-phonon coupling [50, 53] or mode coupling correction [75]. Therefore, the theoretical study of the electron correlation caused by the coexistence of the AFM and AFO fluctuations is important.

As a possible pairing symmetry of LiFeAs, the spin-triplet $p$-wave state with the nodes of the gap function on the hole FS mediated by the FM fluctuation was proposed on the basis of the effective three-orbital Hubbard model, where the FM fluctuation is largely enhanced relative to the AFM one because of the poor nesting between the hole and electron FSs together with the flatness of the hole band top, which yields the large density of states near the Fermi level responsible for the Stoner enhancement of the magnetic susceptibility [76]. A more realistic five-orbital Hubbard model for LiFeAs was investigated on the basis of the dynamical mean-field theory (DMFT), which includes the local correlation effects sufficiently and found to show the orbital antiphase $s_\pm$-wave pairing mediated by the AFM fluctuation observed to be much larger than the FM one, in which the gap function changes its sign between the hole FSs and has nodes on the electron FSs owing to the strong repulsion between the $d_{zx(yz)}$ and $d_{xy}$ orbitals [77]. In addition, several authors have proposed the hole-$s_\pm$-wave pairing with the sign change between the hole FSs without any nodes mediated by the AFM fluctuations with $\boldsymbol{q} \sim (\pi, \pi)$ in addition to $\boldsymbol{q} \sim (\pi, 0)$ [78] and by the AFO fluctuation, which is enhanced comparably to the AFM one by taking into account the electron-phonon interaction or the mode coupling effect [75].

In our previous work [66], the five-orbital Hubbard model for iron-based superconductors was studied using the DMFT combined with the Eliashberg equation, in which the effective pairing interactions mediated by the spin, charge, and orbital fluctuations are obtained from the corresponding DMFT susceptibilities, to discuss the superconductivity in the strong correlation regime where the magnetic and/or orbital orders take place. We found that the $s_\pm$-wave pairing is realized for $U > U'$ where the magnetic fluctuation dominates over the orbital one, while the $s_{++}$-wave pairing is realized for $U < U'$ where the orbital fluctuation dominates over the magnetic one. All of the critical interactions towards the magnetic, orbital, and superconducting instabilities are suppressed as compared

with the results of the random phase approximation (RPA), but the $s_{++}$-wave phase is largely expanded as compared with the RPA result in contrast to the $s_{+-}$-wave phase, which is reduced owing to the different renormalization effects between the spin and charge-orbital vertices.

In this Chapter, we investigate the five-orbital Hubbard model for iron-based superconductors using the DMFT, focusing on the specific case with $U \sim U'$ where the AFM and AFO fluctuations are comparably enhanced. Then, we discuss the pairing symmetry in the case with the cooperating AFM and AFO fluctuations as expected to be realized in LiFeAs [75]. Although the case with $U \sim U'$ is unrealistic, the AFO fluctuation is largely enhanced by the electron-phonon interaction and possibly dominates over the AFM one even in the realistic case with $U > U'$ [50, 53]. In fact, a kink structure of the single-particle dispersion around the $\Gamma$ point is observed experimentally in LiFeAs and is considered to be due to the effect of the strong electron-phonon coupling [79]. Thus, we expect that the present results with $U \sim U'$ are realized also for the realistic parameter with $U > U'$ by taking into account the suitable electron-phonon interaction, although it is found that the electron-phonon coupling estimated from the first-principles band calculation for LaFeAsO is smaller than the one that gives the strong enhancement of the AFO fluctuation $\sim -0.4$ eV [80].

## 2.2 Model and Formulation

The five-orbital Hubbard model for iron pnictides is given by the Hamiltonian

$$H = H_0 + H_{\rm int}, \tag{2.1}$$

where the kinetic part $\hat{H}_0$ is determined so as to reproduce the first-principles band structure and its FSs for LaFeAsO [34], as shown in Fig. 2.1, where the weights of orbitals on the FSs are also plotted. In Eq. (2.1), the Coulomb interaction part $H_{\rm int}$ includes the multi-orbital interaction on Fe sites: the intra- and inter-orbital direct terms $U$ and $U'$, the Hund's rule coupling $J$, and the pair transfer $J'$, and is explicitly given by

$$\begin{aligned} H_{\rm int} &= \frac{1}{2}U \sum_i \sum_l \sum_{\sigma\neq\bar{\sigma}} d^\dagger_{il\sigma} d^\dagger_{il\bar{\sigma}} d_{il\bar{\sigma}} d_{il\sigma} \\ &+ \frac{1}{2}U' \sum_i \sum_{l\neq\bar{l}} \sum_{\sigma,\sigma'} d^\dagger_{il\sigma} d^\dagger_{i\bar{l}\sigma'} d_{i\bar{l}\sigma'} d_{il\sigma} \\ &+ \frac{1}{2}J \sum_i \sum_{l\neq\bar{l}} \sum_{\sigma,\sigma'} d^\dagger_{il\sigma} d^\dagger_{i\bar{l}\sigma'} d_{il\sigma'} d_{i\bar{l}\sigma} \\ &+ \frac{1}{2}J' \sum_i \sum_{l\neq\bar{l}} \sum_{\sigma\neq\bar{\sigma}} d^\dagger_{il\sigma} d^\dagger_{il\bar{\sigma}} d_{i\bar{l}\bar{\sigma}} d_{i\bar{l}\sigma}, \end{aligned} \tag{2.2}$$

where $d_{il\sigma}$ is the annihilation operator for Fe-3$d$ electrons with spin $\sigma$ in the orbital $l$ at the site $i$. In this section, we set $d_{3Z^2-R^2}, d_{ZX}, d_{YZ}, d_{X^2-Y^2}$, and $d_{XY}$ orbitals as 1, 2, 3, 4, and 5, where the $x, y$ axes ($X, Y$ axes) are along the nearest Fe-Fe (Fe-As) directions.

To solve the model Eq. (2.1), we use the DMFT [82] in which the lattice model is mapped onto the impurity Anderson model embedded in an effective medium that may be described by the frequency-dependent effective action. In the actual calculations with the DMFT, we solve the effective five-orbital impurity Anderson model, where the Coulomb interaction at the impurity site is given by

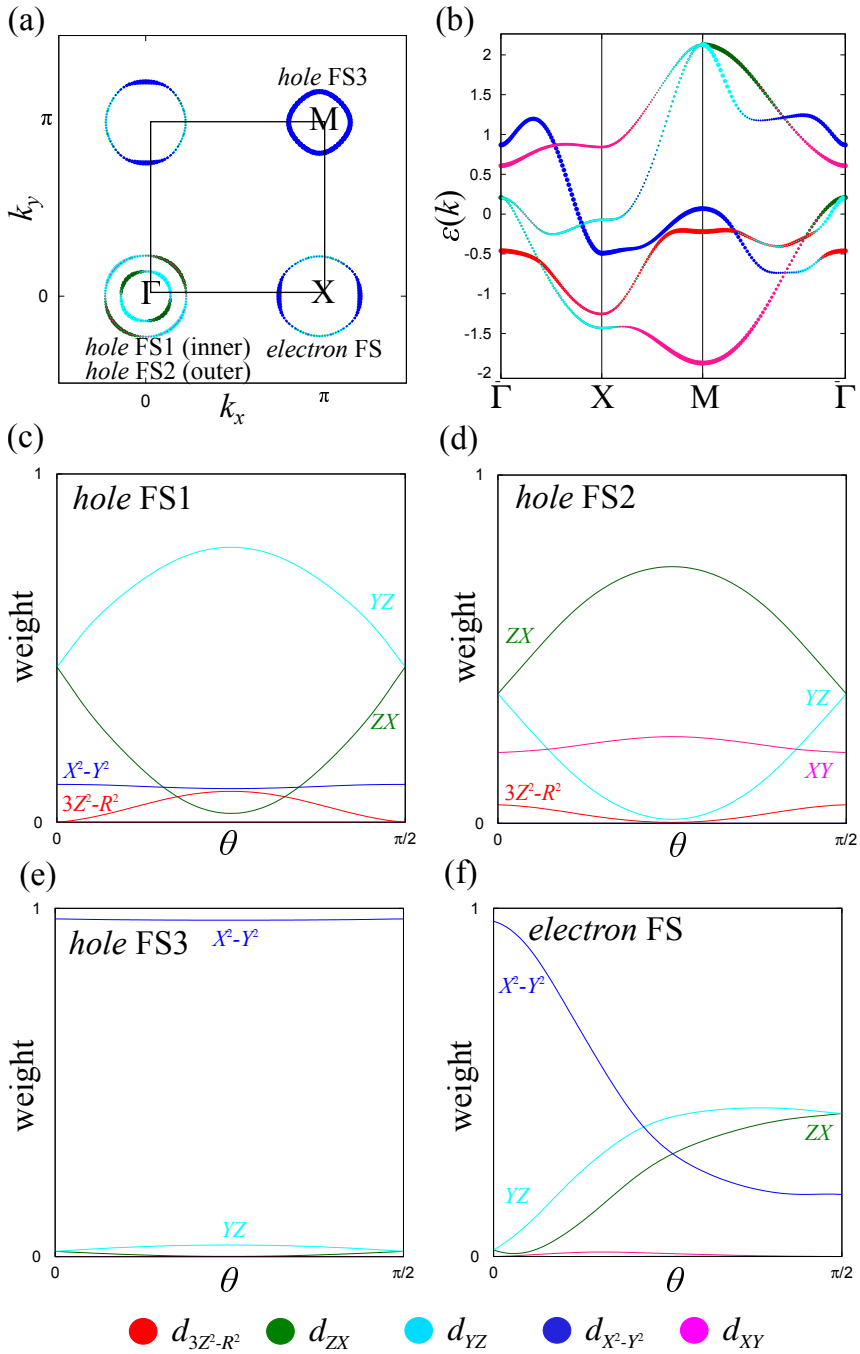


Figure 2.1: (a) FSs of the five-orbital model. (b) Dispersion of the band structure. (c)-(f) Weights of $d$ orbitals on the FSs, where the horizontal axis is $\theta = \tan^{-1}(k_y/k_x)$. We set the Fe-3$d$ orbitals as follows: (1) $d_{3Z^2-R^2}$ (red), (2) $d_{ZX}$ (green), (3) $d_{YZ}$ (cyan), (4) $d_{X^2-Y^2}$ (blue), and (5) $d_{XY}$ (pink) [81].

the same form as $\hat{H}_{\rm int}$ with the site $i$, and the kinetic energy responsible for the bare impurity Green's function $\hat{\mathcal{G}}$ in the $5 \times 5$ matrix representation is determined to satisfy the self-consistency condition. We use the exact diagonalization (ED) method for a finite-size cluster as an impurity solver to obtain the local quantities such as the self-energy $\hat{\Sigma}$. To avoid CPU-time-consuming calculation, we employ clusters with the site number $N_s = 4$ within a restricted Hilbert space, as used in our previous paper [66], where we approximate the clusters with those of $d_{3Z^2-R^2}$ and $d_{XY}$ orbitals by $N_s = 2$ since the two orbitals are far from the Fermi energy in contrast to the other three orbitals. We have confirmed that the results with $N_s = 4$ are qualitatively consistent with those with $N_s = 2$ [83] and quantitatively improved especially for the intermediate interaction regime. Moreover, the studies using the slave-spin mean field [16, 84, 85], the slave-boson mean field (Gutzwiller) [86] approximations, and also the DMFT with the continuous-time quantum Monte Carlo method (CT-QMC) [87] give similar results over our approach. Then, we expect that the present calculation is sufficiently accurate at least up to the intermediate regime.

Within the DMFT, the spin (charge-orbital) susceptibility is given in the $25 \times 25$ matrix representation as

$$\hat{\chi}_{s(c)}(q) = \left[1 - (+)\hat{\chi}_0(q)\hat{\Gamma}_{s(c)}(i\omega_n)\right]^{-1} \hat{\chi}_0(q), \tag{2.3}$$

with $\hat{\chi}_0(q) = -(T/N)\sum_k \hat{G}(k+q)\hat{G}(k)$, where $\hat{G}(k) = [(i\varepsilon_m + \mu) - \hat{H}_0(\boldsymbol{k}) - \hat{\Sigma}(i\varepsilon_m)]^{-1}$ is the lattice Green's function, $\hat{H}_0(\boldsymbol{k})$ is the kinetic part of the Hamiltonian with the wave vector $\boldsymbol{k}$, $\hat{\Sigma}(i\varepsilon_m)$ is the lattice self-energy, which coincides with the impurity self-energy obtained in the impurity Anderson model, and $k = (\boldsymbol{k}, i\varepsilon_m)$, $q = (\boldsymbol{q}, i\omega_n)$. Here, $\varepsilon_m = (2m+1)\pi T$ and $\omega_n = 2n\pi T$ are the fermionic and bosonic Matsubara frequencies, respectively. In Eq. (2.3), $\hat{\Gamma}_{s(c)}(i\omega_n)$ is the local irreducible spin (charge-orbital) vertex function in which only the external frequency ($\omega_n$) dependence is considered as a simplified approximation [66, 88] and is explicitly given by

$$\hat{\Gamma}_{s(c)}(i\omega_n) = -(+)\left[\hat{\chi}^{-1}_{s(c)}(i\omega_n) - \hat{\chi}^{-1}_0(i\omega_n)\right], \tag{2.4}$$

with $\hat{\chi}_0(i\omega_n) = -T\sum_{\varepsilon_m} \hat{G}(i\varepsilon_m + i\omega_n)\hat{G}(i\varepsilon_m)$, where $\hat{\chi}_{s(c)}(i\omega_n)$ is the local part of spin (charge-orbital) susceptibility. When the largest eigenvalue $\alpha_s(\boldsymbol{q})$ [$\alpha_c(\boldsymbol{q})$] of $(-)\hat{\chi}_0(q)\hat{\Gamma}_{s(c)}(i\omega_n)$ in Eq. (2.3) for a wave vector $\boldsymbol{q}$ with $i\omega_n = 0$ reaches unity, the instability towards the magnetic (charge-orbital) order with the corresponding $\boldsymbol{q}$ takes place, and then $\alpha_s(\boldsymbol{q})$ [$\alpha_c(\boldsymbol{q})$] is called the spin (charge-orbital) Stoner factor. After the convergence of the DMFT self-consistent loop, the quantity $\hat{\chi}_{s(c)}(i\omega_n)$ in Eq. (2.4) is obtained using the continued fraction algorithm [82].

The effective pairing interaction mediated by the spin and charge-orbital fluctuations is written using the spin (charge-orbital) susceptibility in Eq. (2.3) and the spin (charge-orbital) vertex in Eq. (2.4), and is explicitly given for the spin-singlet state as

$$\begin{aligned}\hat{V}(q) = &\frac{3}{2}\hat{\Gamma}_s(i\omega_n)\hat{\chi}_s(q)\hat{\Gamma}_s(i\omega_n) - \frac{1}{2}\hat{\Gamma}_c(i\omega_n)\hat{\chi}_c(q)\hat{\Gamma}_c(i\omega_n) \\ &+ \frac{1}{2}\left(\hat{\Gamma}^{(0)}_s + \hat{\Gamma}^{(0)}_c\right)\end{aligned} \tag{2.5}$$

with the bare spin (charge-orbital) vertex: $[\hat{\Gamma}^{(0)}_{s(c)}]_{lll l} = U(U)$, $[\hat{\Gamma}^{(0)}_{s(c)}]_{ll'll'} = U'(-U'+2J)$, $[\hat{\Gamma}^{(0)}_{s(c)}]_{ll'l'} = J(2U'-J)$, and $[\hat{\Gamma}^{(0)}_{s(c)}]_{ll'l'l} = J'(J')$, where $l' \neq l$ and the other matrix elements are 0. Substituting

the effective pairing interaction in Eq. (2.5) into the linearized Eliashberg equation

$$\lambda\Delta_{ll'}(k) = -\frac{T}{N}\sum_{k'}\sum_{l_1l_2l_3l_4} V_{ll_1,l_2l'}(k-k') \times G_{l_3l_1}(-k')\Delta_{l_3l_4}(k')G_{l_4l_2}(k'), \tag{2.6}$$

we obtain the gap function $\Delta_{ll'}(k)$ with the eigenvalue $\lambda$, which becomes unity at the superconducting transition temperature $T = T_c$. To solve Eq. (2.6), we neglect the frequency dependence of the vertex $\hat{\Gamma}_{s(c)}(i\omega_n) \approx \hat{\Gamma}_{s(c)}(i\omega_n = 0)$ for simplicity of the numerical calculations; however, the effect of the frequency dependence will be discussed later. Note that Eq. (2.6) yields the RPA result of $\Delta_{ll'}(k)$ when we replace $\hat{\Gamma}_{s(c)}$ with $\hat{\Gamma}_s^{(0)}$ and neglect $\hat{\Sigma}$, and then, is a straightforward extension of the RPA to include the vertex and the self-energy corrections within the DMFT [66].

All calculations are performed for the electron number $n = 6.0$ corresponding to the non-doped case at $T = 0.02$ eV except for the ED calculation in the impurity Anderson model where we calculate the self-energy at $T = 0$ as the explicit $T$-dependence is expected to be small at low temperature $T = 0.02$ eV in the intermediate correlation regime with $Z \gtrsim 0.5$. We use $32 \times 32$ $\boldsymbol{k}$-point meshes and 1024 Matsubara frequencies in the numerical calculations with the fast Fourier transformation. Here and hereafter, we measure the energy in units of eV.

## 2.3 Spin Fluctuation Dominant Case

In this section, we overview the our previous work [66], with a new data of the vertex functions. In the previous RPA study [52], it was found that the $s_\pm$-pairing is mediated by the magnetic fluctuation near the AFM order for $U > U'$, while the $s_{++}$-pairing is mediated by the orbital fluctuation near the FO order for $U < U'$, where the superconductivity is investigated in the wide parameter space by treating $U$, $U'$, $J$ and $J'$ as independent parameters apart from the condition satisfied in the isolated atom: $U = U' + 2J$ and $J = J'$. Correspondingly, we consider the two specific cases with $U > U'$ and $U < U'$ to elucidate the correlation effects beyond the RPA on the magnetic and orbital orders and those fluctuations mediated superconductivity.

First, we consider the case with $U > U'$, where the magnetic fluctuation dominates over the orbital fluctuation. In Figs. 2.2, 2.3, and 2.4, several physical quantities are plotted as functions of $U$ with $U = U' + 2J$, $J/U = 0.1$ and $J = J'$. Fig. 2.2(a) shows the renormalization factor defined by: $Z_l = \left[1 - \frac{d\Sigma_l(\varepsilon)}{d(\varepsilon)}\big|_{\varepsilon\to 0}\right]^{-1}$ with orbital $l = d_{XY}, d_{3Z^2-R^2}, d_{ZX}, d_{YZ}$ and $d_{X^2-Y^2}$. When $U$ increases, all of $Z_l$ monotonically decrease with increasing the variance of $Z_l$. We find that $Z_l$ for $l = d_{X^2-Y^2}$ is the smallest for all $U$ and finally becomes zero at $U_c \sim 5$ while $Z_l$ for $l \neq d_{X^2-Y^2}$ are finite revealing the OSMT [89], as recently discussed in $K_xFe_{2-y}Se_2$ [16] and $KFe_2As_2$ [86] where the ARPES experiments are well accounted for by the slave-spin mean-field [16, 90] and the slave-boson mean-field (Gutzwiller) [86] approximations yielding the OSMT with $Z_{d_{X^2-Y^2}} \to 0$. We note that, even in the intermediate correlation regime away from the OSMT, the large orbital dependence of $Z_l$ results in the significant change in the band dispersion [89] which is consistent with the recent high-resolution ARPES measurements for $Ba_{0.6}K_{0.4}Fe_2As_2$ [15]. Figs. 2.2(b) and (c) show the $U$ dependence of the largest eigenvalues $\alpha_s$ and $\alpha_c$ for several wave vectors $\boldsymbol{q}$, where $\alpha_{s(c)}$ shows a maximum at $\boldsymbol{q} = \boldsymbol{q}_{\max}$. When $U$ increases, both $\alpha_s$ and $\alpha_c$ increase with $\alpha_s > \alpha_c$ and $\alpha_s$ becomes unity at $U_c^{\rm AFM} \sim 2.40$ where the magnetic susceptibility with $\boldsymbol{q} \sim (\pi, 0)$ corresponding to the stripe-type AFM diverges. The largest eigenvalue $\lambda$ of the Eliashberg equation (2.6) is also plotted in

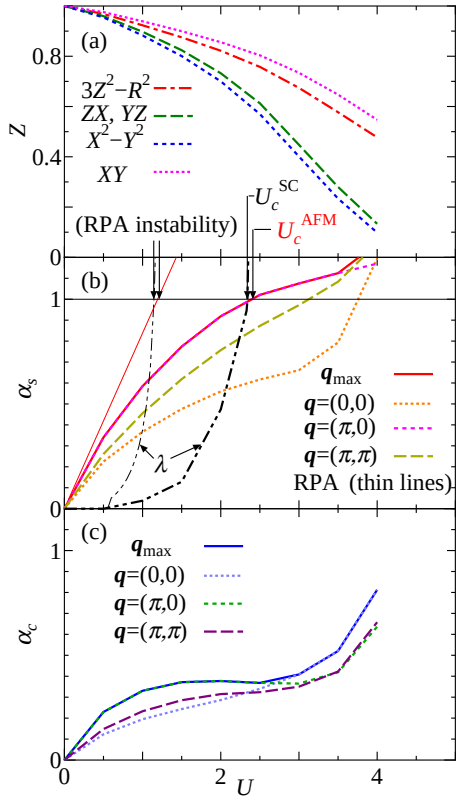


Figure 2.2: (Color online) (a) The renormalization factor $Z_l$ with $l = d_{XY}, d_{3Z^2-R^2}, d_{ZX}, d_{YZ}$ and $d_{X^2-Y^2}$ (b) and (c) the largest eigenvalues $\alpha_s$ and $\alpha_c$ for several $\boldsymbol{q}$ and $\lambda$ which reach unity towards the magnetic, charge-orbital and superconducting instabilities, respectively, as functions of $U$ with $U = U' + 2J$, $J/U = 0.1$ and $J = J'$ for $n = 6.0$ and $T = 0.02$. The RPA results of $\alpha_s$ for $\boldsymbol{q}_{\max}$ and $\lambda$ are also plotted by thin lines in (b) [66].

Fig. 2.2(b) and is found to increase with increasing $\alpha_s$ and finally reaches unity at $U_c^{\rm SC} \sim 2.34$ where the superconducting instability occurs. For comparison, we also plot the RPA results of $\alpha_s$ for $\boldsymbol{q}_{\max}$ and $\lambda$ in Fig. 2.2(b) and find that the critical interactions $U_c^{\rm AFM}$ and $U_c^{\rm SC}$ from the DMFT are about twice larger than those from the RPA [34] due to the correlation effects beyond the RPA and are consistent with the values of the effective Coulomb interactions derived from the downfolding scheme based on first-principles calculations [32].

Next, we discuss the spin and charge-orbital irreducible vertex functions with the lowest Matsubara frequency $i\omega_n = 0$, $\Gamma^{s(c)}_{l_1l_2l_3l_4} \equiv [\hat{\Gamma}_{s(c)}(i\omega_n = 0)]_{l_1l_2l_3l_4}$, where the orbital-diagonal components $\Gamma^s_{lll}$ and the orbital-off-diagonal components $\Gamma^s_{ll'll'}$ $(l \neq l')$ are compared with the corresponding nonzero components of the bare vertices $[\hat{\Gamma}^{(0)}_{s(c)}]_{lll}$ and $[\hat{\Gamma}^{(0)}_{s(c)}]_{ll'll'}$ defined in the text below Eq. (2.5). Figures 2.3(a) and 2.3(b) show the spin vertex functions $\Gamma^s_{lll}$ and $\Gamma^s_{ll'll'}$ for various $l$ and $l'(\neq l)$ values together with the corresponding bare vertices $[\hat{\Gamma}^{(0)}_s]_{lll} = U$ and $[\hat{\Gamma}^{(0)}_s]_{ll'll'} = U'$, respectively. We find that $\hat{\Gamma}_s$ is renormalized as $U$ increases owing to the correlation effect and shows a orbital dependence slightly. As shown in Fig. 2.3(a), the orbital-diagonal components $\Gamma^s_{lll}$ for $l = X^2 - Y^2, ZX/YZ$ are considerably

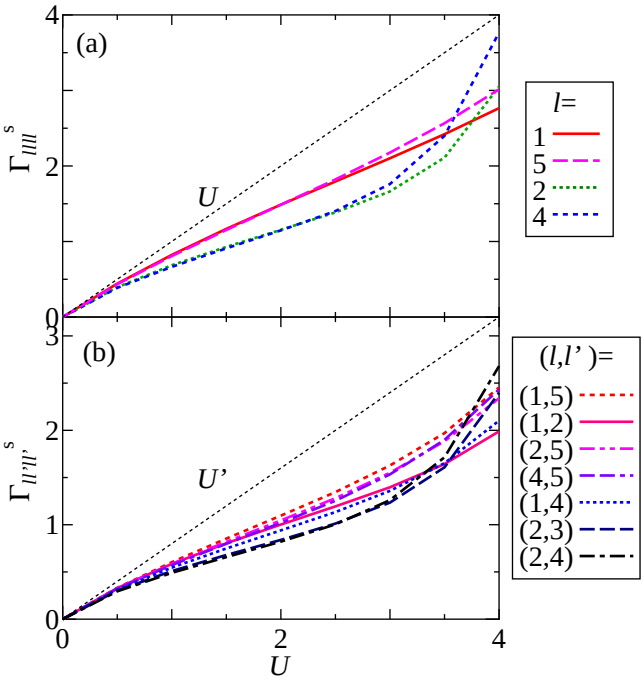


Figure 2.3: (Color online) Spin vertex functions for the orbital-diagonal components $\Gamma^s_{lll}$ (a) and the orbital-off-diagonal components $\Gamma^s_{ll'll'}$ (b) as functions of $U$ with $U = U' + 2J$, $J/U = 0.1$ and $J = J'$ for $n = 6.0$ and $T = 0.02$. The bare vertices are also plotted by thin dotted lines [66].

reduced, while those for $l = XY, 3Z^2 - R^2$ are less reduced. This is considered to be due to the difference between the weights of each $d$ orbital at the FSs: those are large for $l = X^2 - Y^2, ZX/YZ$, while small for $l = XY, 3Z^2 - R^2$, as shown in Figs. 2.1(c)–2.1(f). However, these reduction is less crucial than that of $Z_l$, and this is strike contrast to the spin and orbital fluctuations-competing case, as will be discussed in the Sec. 2.5. The moderately reduction of the spin vertex together with strong correction of $Z_l$ for $l = X^2 - Y^2, ZX/YZ$ with the large orbital weights at the FSs may result in the suppression of the magnetic order due to the correlation effect, as shown in Fig. 2.2. In contrast to those of the spin vertex, the orbital-diagonal components of the charge vertex $\Gamma^c_{lll}$ become larger than those of the corresponding bare vertex $[\hat{\Gamma}^{(0)}_c]_{lll} = U$, as shown in Fig. 2.3(a), resulting in the suppression of the charge susceptibility due to the correlation effect. On the other hand, the orbital-off-diagonal components of the charge vertex $\Gamma^c_{ll'll'}$ are reduced, as shown in Fig. 2.3(b). The significant increase of the spin vertices for $U > 2.4$ may attributable to the proximity of a Mott phase, although the long-range magnetic order and the superconductivity have taken place $\sim 2.40$, and then this vertex correction cannot contribute to these instabilities.

## 2.4 Orbital Fluctuation Dominant Case

Next, we consider the case with $U < U'$, where the orbital fluctuation dominates over the magnetic fluctuation. Figs. 2.5 (a)-(c) show the renormalization factor $Z_l$ and the largest eigenvalues $\alpha_s$, $\alpha_c$

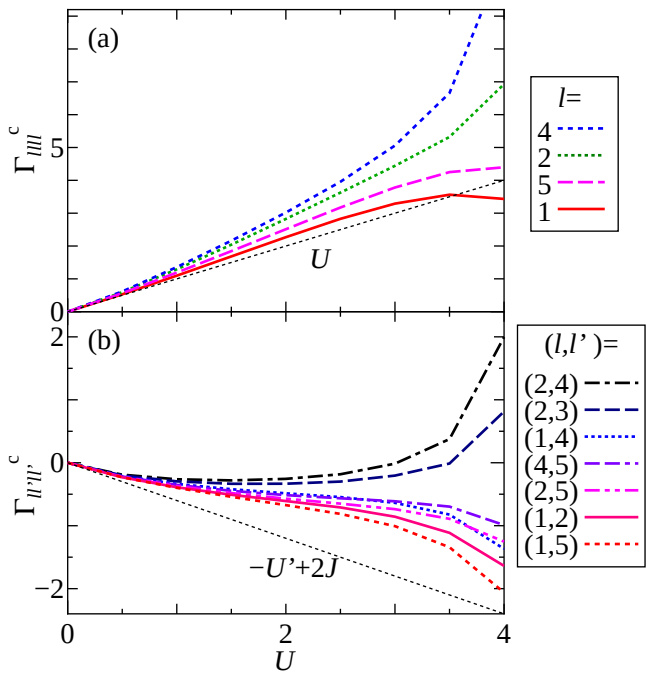


Figure 2.4: (Color online) Charge-orbital vertex functions for the orbital-diagonal components $\Gamma^c_{lll}$ (a) and the orbital-off-diagonal components $\Gamma^c_{ll'll'}$ (b) as functions of $U$ with $U = U' + 2J$, $J/U = 0.1$ and $J = J'$ for $n = 6.0$ and $T = 0.02$. The bare vertices are also plotted by thin dotted lines [66].

and $\lambda$ as functions of $U'$ with $U = 0.25U' + 2J$, $J/U = 0.1$ and $J = J'$. When $U'$ increases, $Z_l$ for all $l$ monotonically decrease with keeping the smallest value for $l = d_{X^2-Y^2}$, similar to the case of Fig. 2.2 (a). When $U'$ increases, both $\alpha_s$ and $\alpha_c$ increase with $\alpha_s < \alpha_c$ and $\alpha_c$ becomes unity at $U_c^{\rm FO} \sim 2.28$ where the orbital susceptibility with $\boldsymbol{q} \sim (0,0)$ corresponding to the FO diverges. We note that $\boldsymbol{q}_{\rm max} = (0, \pi/4)$ just below $U_c^{\rm FO}$ with $\alpha_c = 0.98$ and $\boldsymbol{q}_{\rm max} = (0,0)$ just above $U_c^{\rm FO}$ with $\alpha_c = 1.03$, while it is difficult to determine $\boldsymbol{q}_{\rm max}$ precisely at $U_c^{\rm FO}$ with $\alpha_c = 1$ within the present numerical resolution as $\chi_c$ diverges almost simultaneously for $\boldsymbol{q} \sim (0,0)$ and then we call the FO in a broad sense. With increasing $\alpha_c$, $\lambda$ increases and finally reaches unity at $U_c^{\rm SC} \sim 1.54$ where the superconducting instability occurs. For comparison, we also plot the RPA results of $\alpha_c$ for $\boldsymbol{q}_{\rm max}$ and $\lambda$ in Fig. 2.5 (c), and find that $U_c^{\rm FO}$ and $U_c^{\rm SC}$ from the DMFT are larger than those from the RPA due to the correlation effects beyond the RPA. Remarkably, the DMFT result of the $s_{++}$-pairing phase with $U_c^{\rm SC} < U < U_c^{\rm FO}$ is largely expanded as compared to the RPA result, in contrast to the case with the $s_{\pm}$-pairing phase which is reduced [see Fig. 2.2 (b)].

## 2.5 Spin and Orbital Fluctuations-competing Case)

In the previous section, we investigated the model Eq. (2.1) using the DMFT combined with the Eliashberg equation as mentioned in Sec. 2.2, and found that the $s_{\pm}$-wave pairing is realized for $U > U'$ where the magnetic fluctuation dominates over the orbital one, while the $s_{++}$-wave pairing is realized for $U < U'$ where the orbital fluctuation dominates over the magnetic one. In this section, we

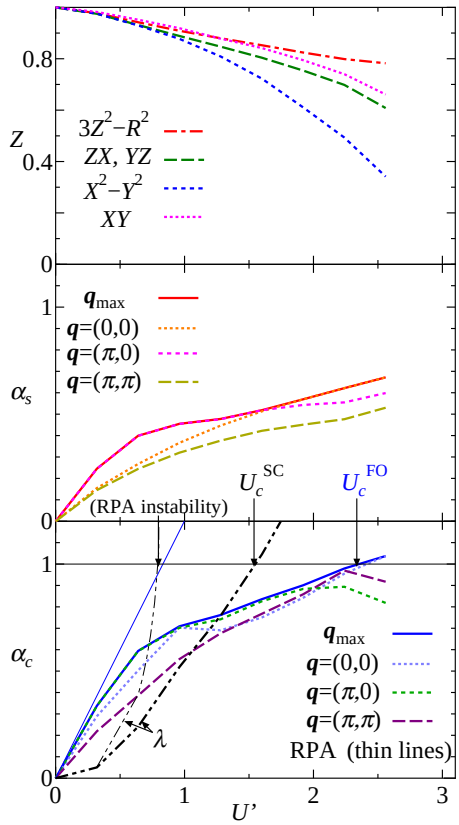


Figure 2.5: (Color online) (a) The renormalization factor $Z_l$ with $l = d_{XY}, d_{3Z^2-R^2}, d_{ZX}, d_{YZ}$ and $d_{X^2-Y^2}$, (b) and (c) the largest eigenvalues $\alpha_s$ and $\alpha_c$ for several $\boldsymbol{q}$ and $\lambda$ which reach unity towards the magnetic, charge-orbital and superconducting instabilities, respectively, as functions of $U'$ with $U = 0.25U' + 2J$, $J/U = 0.1$ and $J = J'$ for $n = 6.0$ and $T = 0.02$. The RPA results of $\alpha_c$ for $\boldsymbol{q}_{\max}$ and $\lambda$ are also plotted by thin lines in (c).

focus on the typical parameter with $U \sim U'$ and vary $U$ while keeping $U = U' - 0.2$ and $J = J' = 0.15$ to simulate the specific case where the magnetic and orbital fluctuations are comparably enhanced in the intermediate region of $U > U'$ and $U < U'$.

### 2.5.1 Renormalization factor

First, we discuss the self-energy correction. Figure 2.8 shows $Z_l$ as a function of $U$. $Z_l$ is almost independent of $l$ and gradually decreases with increasing $U$. As previously discussed by several authors [91, 92, 85], the orbital dependence of $Z_l$ becomes large in the case with a large $J$ and/or $U/U'$, where the magnetic fluctuation is dominated over the orbital one, and the orbital selective Mott transition, in which $Z_l$ with a specific $l$ exclusively becomes zero, may occur. More generally, the imbalance between the magnetic and orbital fluctuations is considered to be critical for enhancing the orbital dependence of $Z_l$. Actually, the exclusively small $Z_l$ with $l = X^2 - Y^2$ was found for both sides of the magnetic-fluctuation-dominated case with $U > U'$ and the orbital-fluctuation-dominated

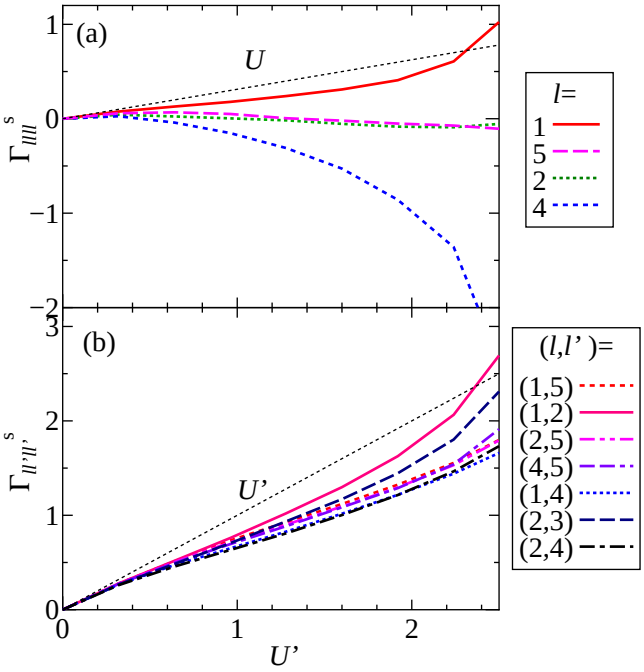


Figure 2.6: (Color online) Spin vertex functions for the orbital-diagonal components $\Gamma^s_{lll}$ (a) and the orbital-off-diagonal components $\Gamma^s_{ll'll'}$ (b) as functions of $U'$ with $U = 0.25U' + 2J$, $J/U = 0.1$ and $J = J'$ for $n = 6.0$ and $T = 0.02$. The bare vertices are also plotted by thin dotted lines [66].

case with $U < U'$ [66]. This is a striking contrast to the present case with $U \sim U'$, where the magnetic and orbital fluctuations compete with each other, resulting in the almost orbital-independent $Z_l$, as shown in Fig. 2.8.

### 2.5.2 Vertex function

Figures 2.9(a) and 2.9(b) show the spin vertex functions $\Gamma^s_{lll}$ and $\Gamma^s_{ll'll'}$ for various $l$ and $l'(\neq l)$ values, respectively, where the zeroth-order contribution of the vertex is depicted as thin-dot lines. We reveal that $\hat{\Gamma}_s$ is strongly renormalized as $U$ increases owing to a characteristic correlation effect and shows a significant orbital dependence. We show in Fig. 2.9(a) that, as with the spin fluctuation dominant case, the orbital-diagonal components $\Gamma^s_{lll}$ for $l = X^2 - Y^2, ZX/YZ$ are largely reduced, while those for $l = XY, 3Z^2 - R^2$ are less reduced. The strong reduction of the spin vertex for $l = X^2 - Y^2, ZX/YZ$ with the large orbital weights at the FSs may result in the suppression of the magnetic order due to the correlation effect, which will be discussed in the next subsection.

$\Gamma^c_{lll}$ is enhanced by the correlation effect [Fig. 2.9(a)] which makes the charge fluctuation smaller. The enhancement is qualitatively consistent with the single-orbital DMFT+ED study [93]. On the other hands, $\Gamma^c_{ll'll'}$ is strongly renormalized similar to the case of the spin vertex [Fig. 2.10 (b)], resulting in the suppression of the orbital order due to the correlation effect, which is similar to that of the magnetic order but is relatively smaller than the latter, as explicitly shown in the next subsection.

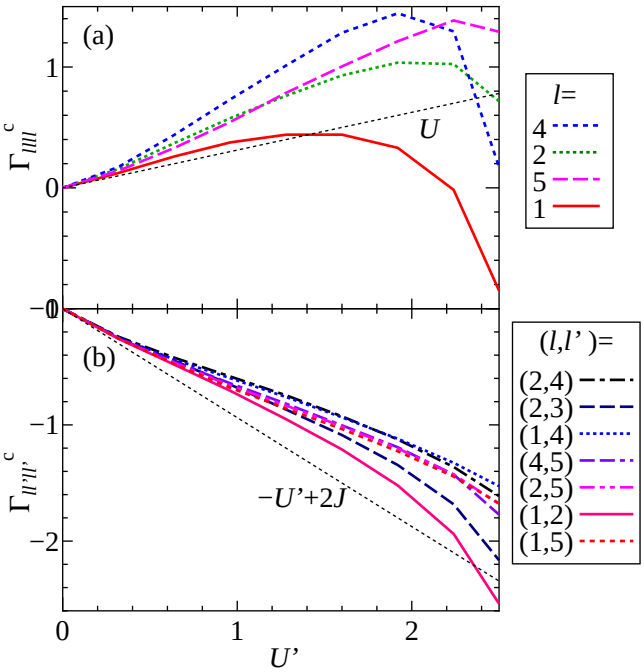


Figure 2.7: (Color online) Charge-orbital vertex functions for the orbital-diagonal components $\Gamma^c_{lll}$ (a) and the orbital-off-diagonal components $\Gamma^c_{ll'll'}$ (b) as functions of $U'$ with $U = 0.25U' + 2J$, $J/U = 0.1$ and $J = J'$ for $n = 6.0$ and $T = 0.02$. The bare vertices are also plotted by thin dotted lines [66].

The opposite renormalization effects between the spin and charge vertices were previously discussed in the single-orbital Hubbard model on the basis of the DMFT [93] and the self-consistent fluctuation theory [94], including the correlation effects beyond the RPA. It was found that $\Gamma_s < \Gamma^{(0)} < \Gamma_c$, resulting in the suppression of both the spin and charge susceptibilities, consistent with the present results for the orbital-diagonal components of the spin and charge-orbital vertices. The orbital-off-diagonal components as well as the orbital dependence of the vertices, however, could not considered in the single-orbital model and are firstly discussed in this thesis. Note that the large orbital dependence of the vertex [see Figs. 2.9 and 2.10] together with the small orbital dependence of the renormalization factor [see Fig. 2.8] is a specific feature of the present case with $U \sim U'$, where the AFM and the AFO fluctuations are comparably enhanced. This is a striking contrast to the case with $U > U'$ ($U < U'$), where the AFM (AFO) fluctuation dominates over the AFO (AFM) one, and the small orbital dependence of the vertex together with the large orbital dependence of the renormalization factor responsible for the orbital selective Mott transition in the strong correlation regime is observed [66].

### 2.5.3 Spin and charge-orbital Stoner factors

Figures 2.11(a) and 2.11(b) show the $U$-dependences of the spin and charge-orbital Stoner factors $\alpha_s(\boldsymbol{q})$ and $\alpha_c(\boldsymbol{q})$, respectively, for the wave vectors $\boldsymbol{q} = (\pi, 0)$, $(0, 0)$, and $(\pi, \pi)$. The critical value towards the magnetic instability is found to be $U_c \sim 4.9$ and is largely suppressed as compared with

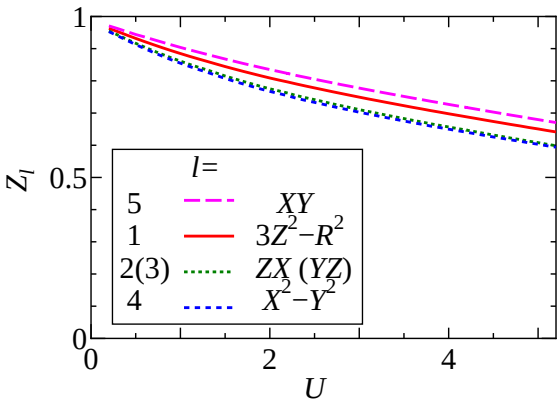


Figure 2.8: Renormalization factor $Z_l$ with $l = d_{3Z^2-R^2}, d_{ZX}, d_{YZ}, d_{X^2-Y^2}$, and $d_{XY}$ as functions of $U$ with $U = U' - 0.2$, $J = 0.15$, and $J = J'$ for $n = 6.0$ and $T = 0.02$ [81].

the RPA result $U_c^{\rm RPA} \sim 0.8$ due to the self-energy and the vertex corrections within the DMFT. For small $U$, the stripe-type AFM and AFO fluctuations with $\boldsymbol{q} = (\pi, 0)$ are dominant over the other fluctuations. However, when $U$ increases, the FM fluctuation with $\boldsymbol{q} = (0, 0)$ becomes competitive with the AFM and AFO fluctuations, and finally overcomes those just below $U_c$, where the FM instability takes place. The FM fluctuation originates from the $\boldsymbol{q} \sim (0, 0)$ nesting between the inner-hole FS1 with the large $ZX/YZ$ orbital weights [see Fig. 2.1(c)] and the outer-hole FS2 with the large $XY$ orbital weight [see Fig. 2.1(d)], and is enhanced by the inter-orbital Coulomb interaction between the $ZX/YZ$ and the $XY$ orbitals. This enhancement becomes significant for a large $U$ as the renormalization of the $d_{ZX/YZ}$-$d_{XY}$ orbital-off-diagonal spin vertex is relatively smaller than that of the $d_{X^2-Y^2}$ and $d_{ZX/YZ}$ orbital-diagonal spin (charge-orbital) vertices [see Figs. 2.9 and 2.10], which enhance the AFM (AFO) fluctuation as shown in the next subsection.

To clarify the effects of the vertex corrections on the magnetic and orbital fluctuations more explicitly, we estimate the spin and charge-orbital Stoner factors using the approximate vertex in stead of the full DMFT vertex $\hat{\Gamma}_{s(c)}$ in Eq. (2.3) as follows (see Table 2.1): (i) When we approximately use the bare vertex $\hat{\Gamma}_{s(c)} \approx \hat{\Gamma}^{(0)}_{s(c)}$, the AFM fluctuation is exclusively enhanced similar to the case with the RPA. (ii) When we average over the orbital as $\hat{\Gamma}_{s(c)} \approx \langle \hat{\Gamma}_{s(c)} \rangle$, the AFO fluctuation is enhanced comparably to the AFM one owing to the different renormalization between the spin and charge-orbital vertices, but the enhancement of the FM fluctuation is relatively small as the orbital dependence of the spin vertex, which is crucial for the FM fluctuation enhancement as mentioned above, is neglected. (iii) When we use the full DMFT vertices $\hat{\Gamma}_{s(c)}$, the AFM, FM, and AFO fluctuations are comparably enhanced owing to the orbital dependence of the vertices together with the difference in renormalization between the spin and the charge-orbital vertices.

### 2.5.4 Susceptibility and effective pairing interaction

Figures 2.12(a) and 2.12(b) show the orbital-diagonal and orbital-off-diagonal components of the spin susceptibilities $\chi^s_{l,l;m,m}$ and $\chi^s_{l,m;l,m}$ as a function of the wave vector $\boldsymbol{q}$ with the lowest Matsubara frequency $i\omega_n = 0$ for $U = 4.5$, where the spin Stoner factor is $\alpha_s = 0.958$. The $d_{X^2-Y^2}$ intra-orbital

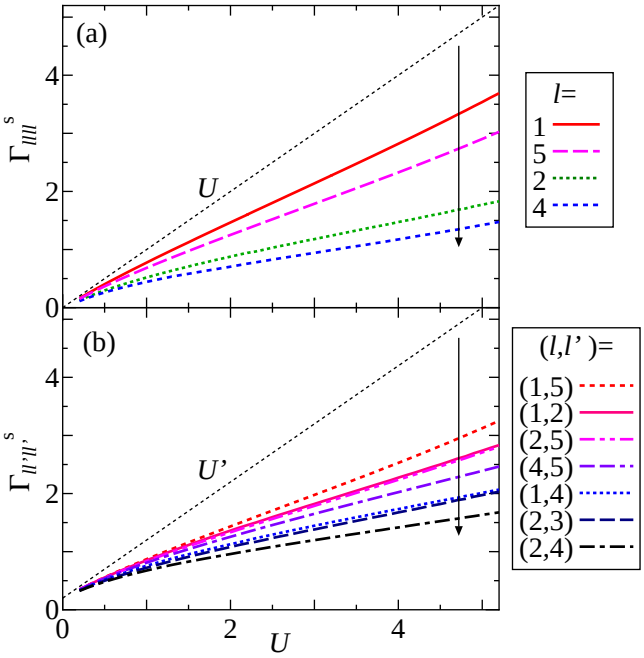


Figure 2.9: Spin vertex functions for the orbital-diagonal components $\Gamma^s_{lll}$ (a) and the orbital-off-diagonal components $\Gamma^s_{ll'll'}$ (b) as functions of $U$. The bare vertices are also plotted by thin dotted lines [81].

spin susceptibility $\chi^s_{4,4;4,4}$ is largely enhanced around $\boldsymbol{q} \sim (\pi, 0)$ [see Fig. 2.12(a)] owing to the effect of the intra-orbital nesting between the hole FS3 and the electron FS, where the weight of the $d_{X^2-Y^2}$ component is large in both FSs, as shown in Figs. 2.1(e) and 2.1(f). Then, the $d_{X^2-Y^2}$ orbital is mainly responsible for the spin susceptibility $\sum_{l,m} \chi^s_{l,l;m,m}$ around $\boldsymbol{q} \sim (\pi, 0)$. Note that the inter-orbital spin susceptibility $\chi^s_{2,4;2,4}$ is also enhanced for $\boldsymbol{q} \sim (\pi, 0)$ [see Fig. 2.12(b)] owing to the effect of the inter-orbital ($d_{ZX/YZ}$-$d_{X^2-Y^2}$) nesting between the hole FS2 and the electron FS.

In addition to the intra- and inter-orbital spin susceptibilities with $\boldsymbol{q} \sim (\pi, 0)$, the inter-orbital spin susceptibility $\chi^s_{2,5;2,5}$ around $\boldsymbol{q} \sim (0, 0)$ is largely enhanced owing to the inter-orbital ($d_{ZX/YZ}$-$d_{XY}$) nesting between the inner (FS1) and the outer (FS2) hole FSs, as shown in Fig. 2.12(b). As mentioned earlier, the orbital-dependent spin vertex with a relatively large value of the $d_{ZX/YZ}$-$d_{XY}$ orbital-off-diagonal component is crucial for the FM fluctuation enhancement, which is a remarkable correlation effect beyond the RPA.

Figure 2.12(c) shows several components of the charge-orbital susceptibility as functions of $\boldsymbol{q}$ with the lowest Matsubara frequency $i\omega_n = 0$ for $U = 4.5$, where the charge-orbital Stoner factor is $\alpha_c = 0.958$. As with the spin susceptibility, both the intra- and inter-orbital charge-orbital susceptibilities are largely enhanced around $\boldsymbol{q} \sim (\pi, 0)$ owing to the intra- and inter-orbital nesting effects. In the present case, one observes $\chi^c_{4,4;4,4} \approx \chi^c_{2,4;2,4}$ for $\boldsymbol{q} \sim (\pi, 0)$.

In Fig. 2.12(d), several components of the effective pairing interaction $\hat{V}(q)$ are plotted as functions of $\boldsymbol{q}$ with the lowest Matsubara frequency $i\omega_n = 0$ for $U = 4.5$. The inter-orbital component $V_{2,5;2,5}$ becomes very large around $\boldsymbol{q} \sim (0, 0)$ owing to the inter-orbital FM fluctuation [see Fig. 2.12(b)].

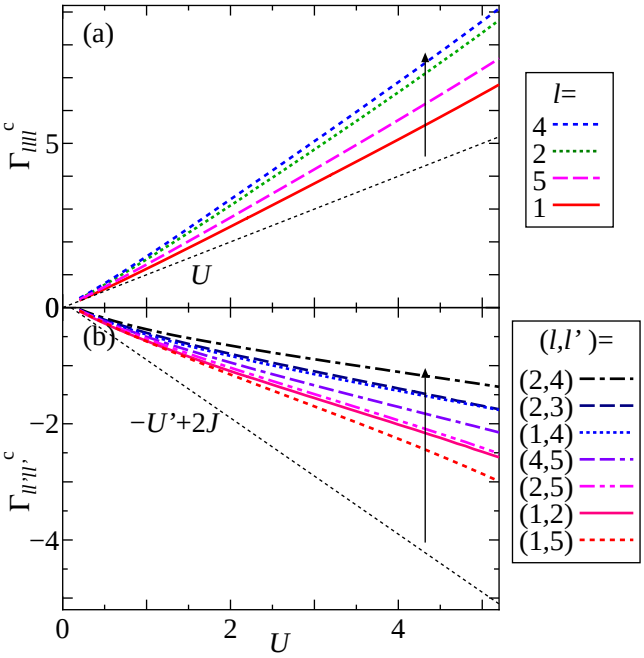


Figure 2.10: Charge-orbital vertex functions for the orbital-diagonal components $\Gamma^c_{lll}$ (a) and the orbital-off-diagonal components $\Gamma^c_{ll'll'}$ (b) as functions of $U$. The bare vertices are also plotted by thin dotted lines [81].

Various components of $\hat{V}(q)$ show peaks at $\boldsymbol{q} \sim (\pi, 0)$, where the AFM-fluctuation-mediated repulsive pairing interaction is partially canceled by the AFO-fluctuation-mediated attractive one, as seen from the 1st and 2nd terms of r.h.s. in Eq. (2.5), resulting in the moderate peak of $\hat{V}(q)$ at $\boldsymbol{q} \sim (\pi, 0)$ in contrast to the large peak at $\boldsymbol{q} \sim (0, 0)$ where the FO fluctuation is not so enhanced [see Fig. 2.12(c)] and such a cancellation effect is small.

### 2.5.5 Superconducting gap function

Finally, we discuss the superconductivity when the FM, AFM, and AFO fluctuations are comparably enhanced. In Figs. 2.13(a)-2.13(c), we show the gap functions $\Delta_s(\boldsymbol{k})$ in the band representation for the band $s = 2 - 4$ with the lowest Matsubara frequency $i\varepsilon_m = i\pi T$ for $U = 4.5$. We observe a specific hole-$s_\pm$-wave pairing, where the gap function changes its sign between the inner-hole FS1 and the outer-hole FS2 owing to the large repulsive pairing interaction $V_{2,5;2,5}$ around $\boldsymbol{q} \sim (0, 0)$ mediated by the FM fluctuation, and also changes between the inner-hole FS1 and the electron FS owing to the moderate repulsive pairing interaction around $\boldsymbol{q} \sim (\pi, 0)$ mediated by the AFM fluctuation [see Fig. 2.12(d)]. Note that we also observe the sign change of the gap function in the orbital representation between the $ZX/YZ$ and $XY$ orbitals (not shown). The obtained hole-$s_\pm$-wave state has the same sign between the hole FS2, hole FS3, and electron FS, and the sign of the gap function of each FS is summarized as $(\Delta_{h1}, \Delta_{h2}, \Delta_{h3}, \Delta_e) = (-, +, +, +)$, which is different from the pairing states previously proposed for LiFeAs with $(\Delta_{h1}, \Delta_{h2}, \Delta_{h3}, \Delta_e) = (+, +, -, +)$, $(-, +, -, +)$, $(+, +, -, -)$ [77, 75, 78], where the correlation-induced FM fluctuation, which is crucial for the present

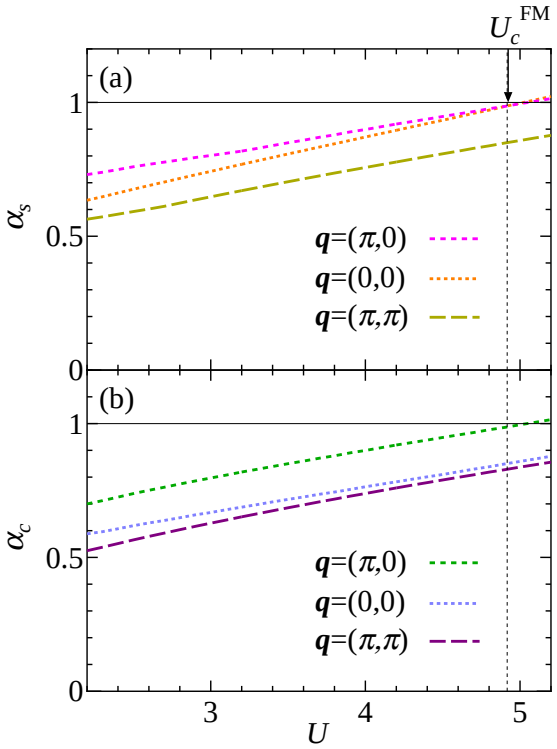


Figure 2.11: $U$-dependences of the spin and charge-orbital Stoner factors $\alpha_s(\boldsymbol{q})$ (a) and $\alpha_c(\boldsymbol{q})$ (b), respectively, for several $\boldsymbol{q}$ values, which reach unity towards the magnetic and charge-orbital instabilities. $U_c^{\mathrm{FM}}$ is the critical value towards the FM instability and is slightly smaller than the critical values towards the AFM and AFO instabilities [81].

| | vertex | $\alpha_s^{\mathrm{AFM}}$ | $\alpha_s^{\mathrm{FM}}$ | $\alpha_c^{\mathrm{AFO}}$ | $\alpha_c^{\mathrm{FO}}$ |
|---|---|---|---|---|---|
| (i) | bare | 1.000 | 0.498 | 0.727 | 0.586 |
| (ii) | orbital-averaged | 1.000 | 0.766 | 0.966 | 0.785 |
| (iii) | full DMFT | 1.000 | 1.003 | 1.001 | 0.863 |

Table 2.1: Spin and charge-orbital Stoner factors, $\alpha_s(\boldsymbol{q})$ and $\alpha_c(\boldsymbol{q})$, respectively, for $\boldsymbol{q} = (\pi, 0)$ and $\boldsymbol{q} = (0, 0)$, in the cases with (i) the bare vertex $\hat{\Gamma}_{s(c)} \approx \hat{\Gamma}^{(0)}_{s(c)}$, (ii) the orbital-averaged vertex $\hat{\Gamma}_{s(c)} \approx \langle \hat{\Gamma}_{s(c)} \rangle$, and (iii) the full DMFT vertex $\hat{\Gamma}_{s(c)}$, where we set (i) $U = 0.76$, (ii) $U = 2.66$, and (iii) $U = 5.05$ so as to fix $\alpha_s^{\mathrm{AFM}} = 1$ in all cases [81].

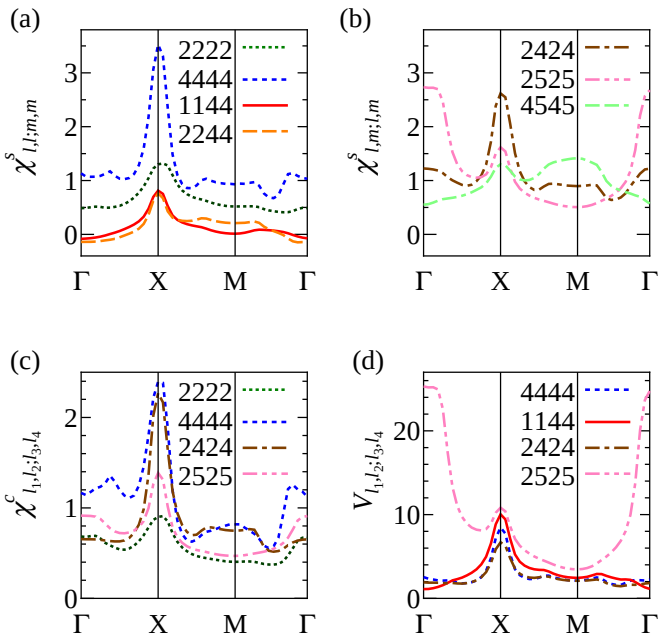


Figure 2.12: Orbital-diagonal and orbital-off-diagonal components of the spin susceptibility, $\chi^s_{l,l;m,m}$ (a) and $\chi^s_{l,m;l,m}$ (b), respectively, several components of the charge-orbital susceptibility $\hat{\chi}^c$ (c), and several components of the pairing interaction $\hat{V}$ (d) as functions of $\boldsymbol{q}$ with the lowest Matsubara frequency $i\omega_n = 0$ for $U = 4.5$, where $\alpha_s = 0.958$ and $\alpha_c = 0.958$ [81].

result, is not taken into account.

In general, the FM fluctuation is considered to mediate the spin-triplet pairing. As for iron pnictides, Brydon *et al.* discussed the spin-triplet $p$-wave pairing mediated by the nearly FM fluctuation within the RPA for the three-orbital Hubbard model [76]. Thus, let us discuss the possibility of the spin-triplet pairing in the present model Eq. (2.1) on the basis of the DMFT combined with the Eliashberg equation, where the effective pairing interaction for the spin-triplet state:

$$\hat{V}(q) = -\frac{1}{2}\hat{\Gamma}_s(i\omega_n)\hat{\chi}_s(q)\hat{\Gamma}_s(i\omega_n) - \frac{1}{2}\hat{\Gamma}_c(i\omega_n)\hat{\chi}_c(q)\hat{\Gamma}_c(i\omega_n) + \frac{1}{2}\left(\hat{\Gamma}_s^{(0)} + \hat{\Gamma}_c^{(0)}\right), \tag{2.7}$$

is substituted into Eq. (2.6) instead of that for the spin-singlet state given in Eq. (2.5). Here, we consider only the $p_x$-wave state, because the present model is symmetric under rotation in spin space, and all $p$-wave states are degenerate in principle. The largest eigenvalues of the Eliashberg equation $\lambda$ for the singlet and triplet states are plotted in Fig. 2.14. When $U$ increases, $\lambda$ for the triplet state increases with increasing FM fluctuation as expected, but is always smaller than $\lambda$ for the singlet state, which is a specific feature of the present multi-orbital model in the case with competing FM, AFM, and AFO fluctuations. Thus, we conclude that the expected pairing state is the spin-singlet hole-$s_{\pm}$-wave.

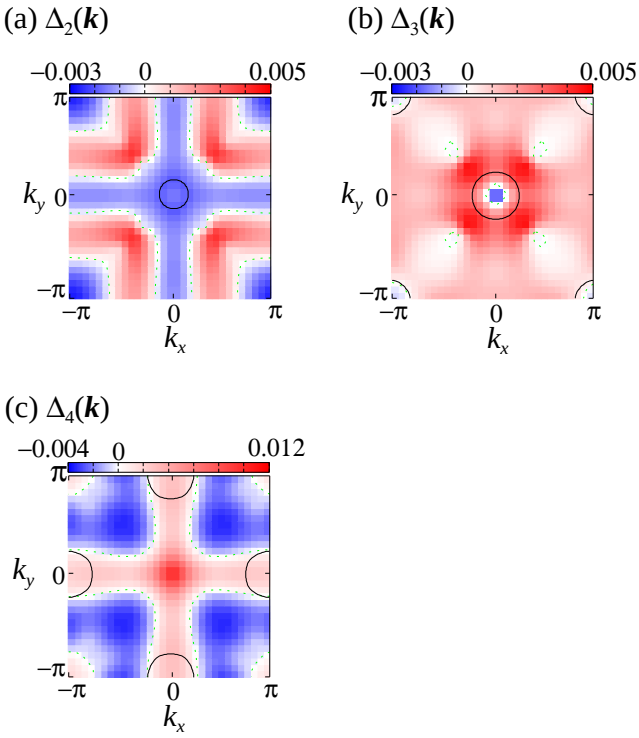


Figure 2.13: Band representation of the superconducting gap functions $\Delta_s(\boldsymbol{k})$ on the $\boldsymbol{k}$-plane for the band $s = 2-4$ with the lowest Matsubara frequency $i\varepsilon_m = i\pi T$ for $U = 4.5$, where the largest eigenvalue of the Eliashberg equation is $\lambda = 1.07$, together with the FSs (solid lines): hole FS1 in (a), hole FS2 and FS3 in (b), and electron FS in (c) [81].

## 2.6 Summary and Discussion

In summary, we have investigated the electronic states and the superconductivity in the five-orbital Hubbard model for iron-based superconductors by using the DMFT combined with the Eliashberg equation to clarify the strong correlation effects, especially focusing on the specific case with $U$ being slightly smaller than $U'$ where the AFM and AFO fluctuations are comparably enhanced. When $U$ increases, the renormalization factor $Z_l$ obtained from the self-energy monotonically decreases almost independently of the orbital $l$ even for a large $U$ in contrast to the previously discussed case with $U > U'$ ($U < U'$), where the AFM (AFO) fluctuation dominates over the AFO (AFM) one and the large $l$-dependence of $Z_l$ responsible for the orbital selective Mott transition for large $U$ is observed [66]. On the other hand, the $l$-dependences of the spin and charge-orbital vertices are large in contrast to the previous case where they are small [66]. The renormalization of the $d_{ZX/YZ}$-$d_{XY}$ orbital-off-diagonal spin vertex responsible for the FM fluctuation enhancement is relatively smaller than that of the $d_{X^2-Y^2}$ and $d_{ZX/YZ}$ orbital-diagonal spin (charge-orbital) vertices responsible for the AFM (AFO) fluctuation enhancement. Therefore, the FM fluctuation is largely enhanced than the AFM and AFO ones and finally overcomes those for large $U$, where the FM instability takes place at $U_c$ just below the AFM and AFO instabilities. In this case, the effective pairing interaction $\hat{V}(q)$ shows

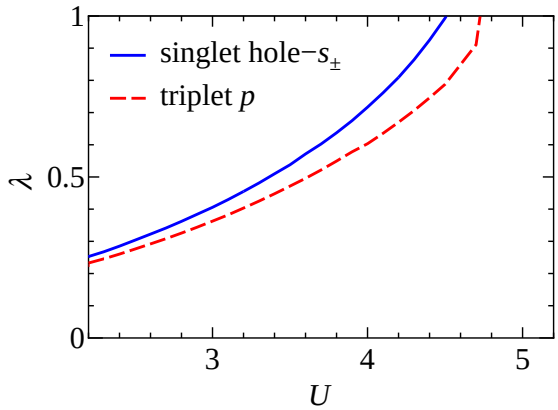


Figure 2.14: Largest eigenvalues of the Eliashberg equation $\lambda$ for the spin-singlet and spin-triplet states as functions of $U$ [81].

a large repulsion at $\boldsymbol{q} \sim (0,0)$ and a small one at $\boldsymbol{q} \sim (\pi,0)$, where the effects of the AFM and AFO fluctuations compete with each other, resulting in a remarkable hole-$s_\pm$-wave pairing with the sign change of the gap function between the inner and the outer hole FSs.

Previously, several authors [77, 75, 78] proposed the orbital antiphase $s_\pm$-wave and hole-$s_\pm$-wave symmetries as promising pairing states for LiFeAs, but the relative signs of the gap function on the FSs are different from the present result. The most significant difference between the previous and present hole-$s_\pm$-wave states is the pairing mechanism: the most dominant pairing interaction in the present theory is a repulsive interaction between the inner and the outer hole FSs at $\boldsymbol{q} \sim (0,0)$ mediated by the largely enhanced FM fluctuation, which was not taken into account in the previous theories but was observed in the $\mu$SR experiment [73]. The nodeless gap structure in LiFeAs observed in the ARPES experiment [79] seems to be consistent with the hole-$s_\pm$-wave states as well as with the other $s$-wave states such as the $s_\pm$- and $s_{++}$-wave states, but it is difficult to distinguish between the various $s$-wave states immediately because of the difficulty in determining the relative sign of the gap function on the different FSs [95, 96, 97].

The enhanced FM fluctuation was previously obtained in the three-orbital Hubbard model for LiFeAs, where the flatness of the hole band top yields a large density of states near the Fermi level responsible for the Stoner enhancement of the magnetic susceptibility within the RPA, and was considered to mediate the spin-triplet $p$-wave pairing with nodes of the gap function on the hole band [76]. This is in striking contrast to the present theory where the strong correlation effect is crucial for enhancing the orbital-off-diagonal FM fluctuation, which mediates the spin-singlet hole-$s_\pm$-wave pairing without nodes consistent with the ARPES experiment [79] mentioned above. In addition, the NMR measurements for LiFeAs [98, 99, 100], where the Knight shift decreases with decreasing $T$ below $T_c$, also seems to be consistent with the spin-singlet pairing.

Finally, we briefly discuss the frequency dependence of the vertex functions, including the retardation effect of the pairing interaction, which is known to enhance the superconducting transition temperature [101, 102]. Although the frequency dependence of the vertex functions was neglected to solve the linearized Eliashberg equation in this section, we have also made some preliminary calculations with the frequency-dependent vertex functions, which are largely renormalized as

$\hat{\Gamma}_{s(c)}(i\omega_n) \sim \hat{\Gamma}_{s(c)}(0)$ for a small $\omega_n$ while the vertex functions are approximately given by the bare vertices as $\hat{\Gamma}_{s(c)}(i\omega_n) \sim \hat{\Gamma}^{(0)}_{s(c)}$ for a large $\omega_n$, and have found that the obtained $\lambda$ is indeed enhanced as compared with the results without the frequency dependence. To be more conclusive, we need to obtain precise vertex functions depending on not only the external frequency but also the internal ones, which were not taken into account in this thesis but are considered to play important roles especially in the strong correlation regime [93], and is an important issue to calculate their frequency dependence.

# Chapter 3

# Electronic state of FeSe in ambient pressure

In present chapter, we address the electronic state on FeSe in ambient pressure. Recently, the angular resolved photoemission spectroscopy (ARPES) and the quantum oscillations (QO) study of FeSe single crystals revealed that hole pocket around the $\Gamma$ point due to the $d_{xy}$ orbital is pushed downward under the Fermi energy. To address this issue, we investigate the correlation effects on the self-energy, the magnetic and orbital fluctuations and its derived superconductivity in 16-band $d$-$p$ model on FeSe within the dynamical mean-field theory. We find that the dissipation of a shallow hole pocket occurs by on-site Coulomb interaction, which corresponds to the orbital-dependent band lifting observed by the recent ARPES and the QO experiments. Furthermore, inter-site orbital-polarization Coulomb interaction between iron $d$ orbital and selenium $p$ orbital drives an electric orbital order in absence of the low-energy commensurate spin response. We also calculate the superconducting gap structure in orbital ordered phase by using the linearized Eliashberg equation, and find that $s_{\pm}$-wave pairing is realized where the $d_{zx(yz)}$ orbital component of spin fluctuation is the cause of superconductivity.

## 3.1 Introduction

Understanding the interplay of strongly interacting electrons and phase transition is one of the main targets for high-$T_c$ superconducting materials theory. Mott transition, spin density wave (SDW), charge density wave (CDW) and orbital order often occur with on-site or long-range Coulomb interaction in strongly correlated electron materials. The SDW appears in the two-dimensional Hubbard model and relates to Mott-insulating state which can be described in terms of local correlations. The phase separation has been observed also in the Hubbard model by introducing the non-local correlations or the inter-site Coulomb interaction. On the other hands, it has been clarified that the properties of these important electronic phenomena strongly depend on the lattice structure. If electronic system has holelike and electronlike Fermi surfaces, interaction between hole and electron in the Fermi surfaces tends to induce SDW or CDW with wave vector $\boldsymbol{q}$ which spans the FS nesting vector. In addition, the FS nesting between different orbital components may drives the orbital-dependent SDW, CDW, and orbital ordering. Thus, the consistency between the effective tight-binding model and the experimental electronic picture is highly desired.

The surprising phase diagram of FeSe has attracted much attention to investigate the origin of

superconductivity and nematicity in iron-based superconductors. This material shows a structural transition at $T_s \sim 90$K and the superconducting transition at $T_c \sim 9$K without long-range magnetic order. $T_s$ ($T_c$) is decreased (increased) by isovalent doping in both $Fe(Se_xS_{1-x})$ [103, 104] and $Fe(Se_xTe_{1-x})$ [105] or by applying pressure [106], while both $T_s$ and $T_c$ are suppressed by nonmagnetic impurity (Co) doping [107]. Toward $T_s$, the softening of share modulus $C_{66}$ [11] and the enhancement of Raman nematic susceptibility $\chi_{x^2-y^2}$ [18] are observed. These results clearly indicate the existence of ferro-orbital fluctuation and electronic ferro-orbital order, as is recognized in other materials of the iron-based superconductors, both theoretically [9, 55, 54, 62] and experimentally [10, 12, 108]. The most remarkable feature of FeSe is observed in the temperature dependence of the spin-lattice relaxation rate $1/T_1T$ in NMR experiment [17, 109]. With decreasing temperature, $1/T_1T$ decreases and reaches to the minimum at $T \sim T_s$. With further decreasing temperature, $1/T_1T$ becomes to increase toward the superconducting temperature. The temperature dependence of $1/T_1T$ together with NMR Knight shift is interpreted by the low-energy properties of the effective tight-binding model derived in Ref. [110], using a priori information of recent angular-resolved photoemission spectroscopy (ARPES) and quantum oscillation (QO) measurements. As mentioned in Ref. [110], the spin-nematic picture for FeSe may be unclear without the strong low-energy spin fluctuation.

Above $T_s$, the recent ARPES experiment [111, 19, 112, 20] found that the hole FS consists of two small pockets of mainly $d_{zx}$ and $d_{yz}$ character around the $\Gamma$-$Z$ line. The narrow $d_{xy}$ hole band exists in about 50 meV below the Fermi level. Orbital-dependent mass enhancement is estimated as $d_{zx/yz} \sim 3$ and $d_{xy} \sim 8$. The ARPES study also found a small electron FS at the $M$ point of mainly $d_{zx}$ and $d_{yz}$ character. Unfortunately, it is difficult to observe the $d_{xy}$ band in ARPES at the $M$ point. However, the QO measurement [19] performed at low temperature detects a presence of the $d_{xy}$ electron pocket. Below $T_s$, ARPES observed the large band splitting of $\sim$50 meV at the $M$ point, which corresponds to orbital order breaking the degeneracy of the $d_{zx}$ and $d_{yz}$ orbitals. By using the detwinned crystal [20], the orbital order has momentum-dependent sign-inversion as $E_{yz}(\Gamma) - E_{zx}(\Gamma) \sim -10$ meV and $E_{yz}(M) - E_{zx}(M) \sim +50$ meV that is interpreted by the orbital order scenario [113, 114] of Aslamazov-Larkin vertex corrections.

To elucidate the electronic correlation effects on FeSe, theoretical studies have been performed intensively [115, 116, 117, 32, 118]. The constrained random phase approximation (cRPA) [32] combined with the *ab initio* calculation scheme indicates that correlation strength plays important rules to understand the material dependence of the iron-based superconductors. The Coulomb interaction of Fe $d$ orbital of FeSe is larger than that of LaFeAsO. Thus, the detail of electronic structure together with the Coulomb interaction parameter are the key information in the iron-based materials. However, DMFT studies [116, 117] found that three hole FS at the $\Gamma$ point as well as the first-principles band calculation whereas ARPES found the two hole FS.

In this chapter, we use the model of FeSe in ambient pressure derived from the first-principles and solve this model using the DMFT to investigate the unusual correlation. We show how $d_{xy}$ hole band exists below the Fermi level predicted by several experiments, and elucidate the origin of orbital-energy shift. The orbital-energy shift is characterized by the orbital dependence of screened Coulomb interaction, which is estimated from first-principles. Consequently, the spin fluctuation due to the $xy$ orbital is clearly suppressed. Moreover, we show the orbital fluctuation enhancement by introducing an "orbital polarization $d$-$p$ Coulomb interaction" [62], which is not attributable to the spin degrees of freedom.

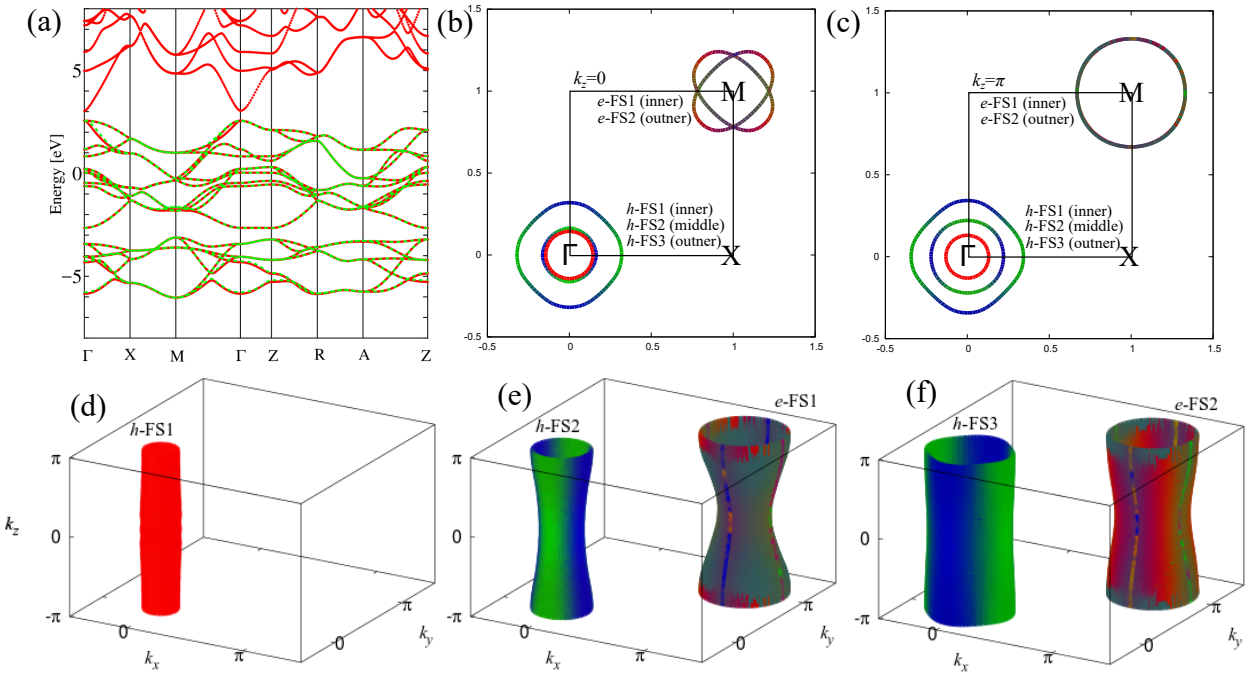


Figure 3.1: Band structures of FeSe (a). Green dash lines and red dotted lines represent the data obtained from the density functional calculation and the derived tight-binding Hamiltonian, respectively. Fermi surface of FeSe (b)-(f).

## 3.2 Model and Method

In this section, we illustrate a DMFT+Eliashberg approach for multi-orbital $d$-$p$ model on FeSe system.

First, we introduce a 16-band $d$-$p$ model including the multi-orbital Coulomb interaction $H_{dd}$ between $3d$ electrons on Fe site, $H_{pp}$ between $4p$ electrons on Se site, and the inter-site Coulomb interaction $H_{dp}$ between $3d$ and $4p$ electrons

$$H = H_0 + H_{dd} + H_{pp} + H_{dp}. \tag{3.1}$$

$H_0$ is the tight-binding Hamiltonian derived from first-principles using maximally localized Wannier functions [119, 120, 121, 122]. The electronic structure is described by the density functional theory using the WIEN2k code [123, 124]. Diagonalizing $H_0$, we obtain the non-interacting band structure and the Fermi surface shown in Fig. 3.1. A large density of the $xy$ orbital on inner hole Fermi surface [red lines in Fig. 3.1(b)-(f)] indicates that the antiferromagnetic spin fluctuation of the $xy$ orbital is strongly enhanced in RPA as will be shown in Fig. 3.3(a).

The on-site Coulomb interaction part on Fe site is given as

$$\begin{aligned} H_{dd} &= \sum_i \sum_l U_{ll} d^\dagger_{il\uparrow} d^\dagger_{il\downarrow} d_{il\downarrow} d_{il\uparrow} \\ &+ \sum_i \sum_{l>l'} \sum_{\sigma,\sigma'} U'_{ll'} d^\dagger_{il\sigma} d^\dagger_{il'\sigma'} d_{il'\sigma'} d_{il\sigma} \\ &+ \sum_i \sum_{l>l'} \sum_{\sigma,\sigma'} J_{ll'} d^\dagger_{il\sigma} d^\dagger_{il'\sigma'} d_{il\sigma'} d_{il'\sigma} \\ &+ \sum_i \sum_{l>l'} \sum_{\sigma\neq\sigma'} J'_{ll'} d^\dagger_{il\sigma} d^\dagger_{il\sigma'} d_{il'\sigma'} d_{il'\sigma}, \end{aligned} \tag{3.2}$$

where $d^{(\dagger)}_{il\sigma}$ is the annihilation (creation) operator of $3d$ electron with orbital $l$ spin $\sigma$ on site $i$, and $U_{ll}, U'_{ll'}, J_{ll'}, J'_{ll'}$ are the Coulomb interaction matrix of the intra- and inter-orbital direct terms, the Hund's rule coupling, and the pair transfer, respectively. From the first principles downfolding scheme given by the constrained-random phase approximation (cRPA) method, Ref. [32] revealed that $U_{ll}, U'_{ll'}, J_{ll'}, J'_{ll'}$ in $H_{dd}$ are orbital dependent and the average of $U_{ll}$ is $\bar{U}_d = 7.2\,\mathrm{eV}$ for FeSe.

The on-site Coulomb interaction part on Se site is given as

$$\begin{aligned} H_{pp} &= \sum_i \sum_m U_{mm} p^\dagger_{im\uparrow} p^\dagger_{im\downarrow} p_{im\downarrow} p_{im\uparrow} \\ &+ \sum_i \sum_{m>m'} \sum_{\sigma,\sigma'} U'_{mm'} p^\dagger_{im\sigma} p^\dagger_{im'\sigma'} p_{im'\sigma'} p_{im\sigma} \\ &+ \sum_i \sum_{m>m'} \sum_{\sigma,\sigma'} J_{mm'} p^\dagger_{im\sigma} p^\dagger_{im'\sigma'} p_{im\sigma'} p_{im'\sigma} \\ &+ \sum_i \sum_{m>m'} \sum_{\sigma\neq\sigma'} J'_{mm'} p^\dagger_{im\sigma} p^\dagger_{im\sigma'} p_{im'\sigma'} p_{im'\sigma}, \end{aligned} \tag{3.3}$$

where $p^{(\dagger)}_{im\sigma}$ is the annihilation (creation) operator of $4p$ electron with orbital $m$ spin $\sigma$ on site $i$, and $U_{mm}, U'_{mm'}, J_{mm'}, J'_{mm'}$ are the Coulomb interaction matrix. $\bar{U}_p = 4.7\,\mathrm{eV}$ was estimated from cRPA study [32] for FeSe. Unfortunately, explicit orbital dependence was not detected so far. Hence, we assume $(U_{mm}, U'_{mm'}, J_{mm'}, J'_{mm'}) = (U_p, U'_p, J_p, J'_p)$, $U_p = U'_p + 2J_p$, $J_p = J'_p$, and $J_p/U_p = 0.1$.

The intersite Coulomb interaction part is written as

$$H_{dp} = V \sum_{\langle i,j \rangle} n_{di} n_{pj} + V' \sum_{\langle i,j \rangle} (n_{dizx} - n_{diyz})(n_{pjx} - n_{pjy}), \tag{3.4}$$

where $n_{dil}$ ($n_{pjm}$) is the number operator of a $d$ ($p$) electron with orbital $l$ ($m$) on site $i$ ($j$), $n_{di} = \sum_l n_{dil}$ ($n_{pj} = \sum_m n_{pjm}$), and $\langle i,j \rangle$ represents the summation of nearest-neighbor Fe and Se sites. In Eq. (3.4), $V'$ is the $d$-$p$ orbital polarization interaction found to enhance the orbital fluctuation as discussed for the iron-pnictides, originating from the the orbital dependence of the Coulomb integrals $V_{lm}$ between Fe $d$ orbitals and Se $p$ orbitals: $V' = (V_{zx,x} - V_{zx,y})/2$ [62].

In our DMFT with a sublattice degrees of freedom, called two-sublattice DMFT, the original site is mapped onto the effective impurity system for each sublattice. Hence one needs to solve the impurity problem twice on two adjacent sites of the original lattice. Note that the $d$ orbital for the five or ten-orbital model contains considerable selenium $p$ orbital component, and then the

hybridization makes a Wannier function delocalized and anisotropic. This indicates the *d*-*p* model is good starting point of DMFT rather than the *d* model. In the *d*-*p* model, since the Coulomb interaction parameters are almost isotropic, the double counting of the correlation effect considered in local density approximation is expected to be very simple. Hence, we argue that the orbital dependence of the double counting is negligibly small. The self-energy due to the inter-site *d*-*p* Coulomb interaction is omitted in present approximation. To consider this effect efficiently, the cluster approximation or the dual fermion approach is needed and will be discussed later.

The spin (charge-orbital) susceptibility in *d*-*p* model is given by

$$\hat{\chi}^{s(c)}(q) = \hat{\chi}^0(q)\left[\hat{1} - (+)\hat{\Gamma}^{s(c)}(q)\hat{\chi}^0(q)\right]^{-1}, \tag{3.5}$$

where $q = (\boldsymbol{q}, i\omega_n)$ with the wave vector $\boldsymbol{q}$ and bosonic Matsubara frequency $\omega_n = 2n\pi T$. $\hat{\Gamma}^{s(c)}$ is the spin (charge-orbital) vertex, which is given as $\hat{\Gamma}^{s(c)} = \Gamma^{s(c)}_{l_1l_2l_3l_4}(i\omega_n) + \Gamma^{s(c)}_{m_1m_2m_3m_4}(i\omega_n) + \hat{\Gamma}^{c,0}_{llmm}(\boldsymbol{q})$. Here, $\Gamma^{s(c)}_{l_1l_2l_3l_4}(i\omega_n)$ is consistent with Eq. (2.4) in Sec. 2.2. The matrix elements in the *d*-*p* submatrix are $\Gamma^{c,0}_{llmm}(\boldsymbol{q})$=$2(V + V'_{\pm})\phi(\boldsymbol{q})$, where $[l, m] = [zx(yz), x(y)]$ for $V'_{\pm} = V'$, $[l, m] = [zx(yz), y(x)]$ for $V'_{\pm} = -V'$, and otherwise $V'_{\pm} = 0$. $\phi(\boldsymbol{q}) = \sum_{\langle i,j\rangle} e^{i\boldsymbol{q}(\boldsymbol{R}_i - \boldsymbol{R}_j)}$ represents the $\boldsymbol{q}$ dependent factor due to intersite Fe-Se contributions, where $\boldsymbol{R}_i - \boldsymbol{R}_j$ denote the lattice vector [62]. Here, we ignored the ladder-type Feynman diagrams for $V'$ in $\hat{\Gamma}^{c,0}(\boldsymbol{q})$. In Eq. (3.5), the irreducible susceptibility $\hat{\chi}^0(q)$ have been defined in Sec. 2.2.

To examine the superconductivity, we solve the linearized Eliashberg equation [see Eq. (2.6) in Sec. 2.2], and obtain the superconducting gap function $\hat{\Delta}(k)$ with the eigenvalue $\lambda$ which becomes unity at the superconducting transition temperature $T_c$, where the effective pairing interaction for the spin-singlet state is given as

$$\begin{aligned}\hat{V}(q) = &\frac{3}{2}\hat{\Gamma}^s(i\omega_n)\hat{\chi}^s(q)\hat{\Gamma}^s(i\omega_n) - \frac{1}{2}\hat{\Gamma}^c(q)\hat{\chi}^c(q)\hat{\Gamma}^c(q)\\ &+ \frac{1}{2}\left(\hat{\Gamma}^{s,0} + \hat{\Gamma}^{c,0}(\boldsymbol{q})\right)\end{aligned} \tag{3.6}$$

where the bare vertex is $\Gamma^{s(c),0}_{llll} = U_{ll}$ $(U_{ll})$, $\Gamma^{s(c),0}_{ll'll'} = U'_{ll'}$ $(-U'_{ll'} + 2J_{ll'})$, $\Gamma^{s(c),0}_{lll'l'} = J_{ll'}$ $(2U'_{ll'} - J_{ll'})$, $\Gamma^{s(c),0}_{ll'l'l} = J'_{ll'}$ $(J'_{ll'})$, $\Gamma^{s(c),0}_{mmmm} = U_p$ $(U_p)$, $\Gamma^{s(c),0}_{mm'mm'} = U'_p$ $(-U'_p + 2J_p)$, $\Gamma^{s(c),0}_{mmm'm'} = J_p$ $(2U'_p - J_p)$, and $\Gamma^{s(c),0}_{mm'm'm} = J'_p$ $(J'_p)$ in the Fe and Se submatrix. We set temperature $T = 0.03\,\mathrm{eV}$. We discuss the Coulomb interaction parameters by multiplying a reduction factor $f_{d(p)}$ so as to suppress the strong spin fluctuation due to the two-dimensionality. For the double-counting correction, we used the fully localized-limit formula [125].

## 3.3 Results

We first show results of DMFT calculation with the on-site Coulomb interaction $f_{d(p)} = 0.75$, that is $U_{xy} = 5.32\,\mathrm{eV}$, $U_{zx/yz} = 5.44\,\mathrm{eV}$, and $U_p = 3.5\,\mathrm{eV}$. Note that the the renormalization factor defined by $Z_l = \left[1 - \frac{d\Sigma_l(\varepsilon)}{d(\varepsilon)}\Big|_{\varepsilon\to 0}\right]^{-1}$ shows $Z_{xy} = 0.57$ and $Z_x = 0.97$. Hence it is the intermediate correlation regime, although we find $Z_{xy} = 0.16$ for $f_d = 1$. We show in Fig. 3.2(a) orbital-averaged, (b) $xy$ orbital, and (c) $zx/yz$ orbital components of the spectral function, which is obtained by the numerical analytic continuation to $i\omega_n \to \omega + i\delta$ using Padé approximation, along high-symmetry

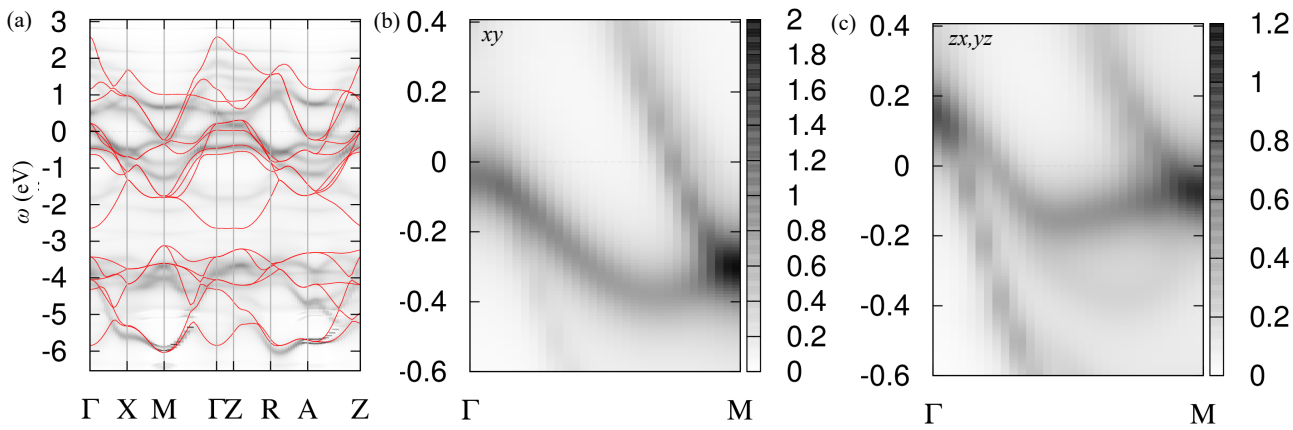


Figure 3.2: Spectral function $A(\boldsymbol{k},\omega)$ for orbital-averaged components (a), $xy$ orbital components (b), and $zx, yz$ orbital components (c). The interpolated-band dispersion with derived tight-binding Hamiltonian is depicted as red solid lines.

directions. The overall renormalizations of quasiparticle bands are observed, even in selenium $p$ bands. We find that a hole Fermi surface of $xy$ orbital character around $\Gamma$ point is pushed downward below Fermi level $E_{xy}(\Gamma) \sim -50\,\mathrm{meV}$. This band structure could not be deduced from rescaling the non-interacting band structure, and is consistent with the experiment. The deviation of the Coulomb repulsion yields the orbital dependence of the self-energy in the real part, resulting in the crystal fields splitting owing to the electronic correlation. Notice that FeTe indicates the larger $U$ of $xy$ orbital than $zx/yz$ orbital due to the weak covalency in contrast to FeSe. Since the fully localized-limit formula omits the orbital-dependent double counting [125], we examined the calculation using the orbital-dependent subtraction of the Hartree-Fock form, but reliable results were not obtained. We confirmed that antiferromagnetic spin susceptibility of $xy$ orbital character is significantly reduced, whereas it is dominantly enhanced in the RPA [Fig. 3.3]. It is recognized that the spin susceptibility is weak within the RPA [110] when the *abinitio* tight-binding model is reconstructed to suit the ARPES and the QO results, and the spin-lattice relaxation rate is weak above $T_s$, consistency with experiments. From our results, this behaver is confirmed from first-principles.

Next, we address the effect of the inter-site Coulomb interaction. In our DMFT, the non-local correlation is considered within the RPA, since the inter-site self-energy correlation is expected to be negligibly small. We show in Fig. 3.4 that the ferro-orbital (nematic) susceptibility defined as $\chi^c_{x^2-y^2}(\mathbf{0},0) = \sum_{l_1,l_2,l_3,l_4} o^{l_1 l_2}_{x^2-y^2} \chi^c_{l_1,l_2;l_3,l_4}(\mathbf{0},0) o^{l_4 l_3}_{x^2-y^2}$ with $o^{zx,zx}_{x^2-y^2} = -o^{yz,yz}_{x^2-y^2} = -(\sqrt{3}/2) o^{3z^2-r^2,x^2-y^2}_{x^2-y^2} = 1$ [51] is enhanced by the orbital polarization interaction $V'$ for $f_d = 0$. Moreover, $V'$ and $f_d$ cooperatively enhance $\chi^c$. Note that the Hund's coupling always suppresses the orbital fluctuation. The raito between the Hund's and Coulomb interaction is $\bar{J}_d/\bar{U}_d = 0.0945$ in FeSe and $\bar{J}_d/\bar{U}_d = 0.134$ in LaFeAsO. The smallness of $\bar{J}_d/\bar{U}_d$ yields that the $\chi^c$ enhancement in FeSe is larger than that of LaFeAsO.

Fig. 3.5 show the superconducting gap function $\Delta$ on Fermi surface at $k_z = 0$ and $i\varepsilon = i\pi T$ for $f_d = 0.5$, $V' = 0$, and $\lambda = 0.859$ in the four-fold symmetry. The nodal-like $s_{\pm}$-wave is realized owing to the antiferromagnetic fluctuation. The outer electron Fermi surface consists of the $xy$ orbital component, and hence indicates nodal-gap behavior in $\Gamma$-$M$ direction.

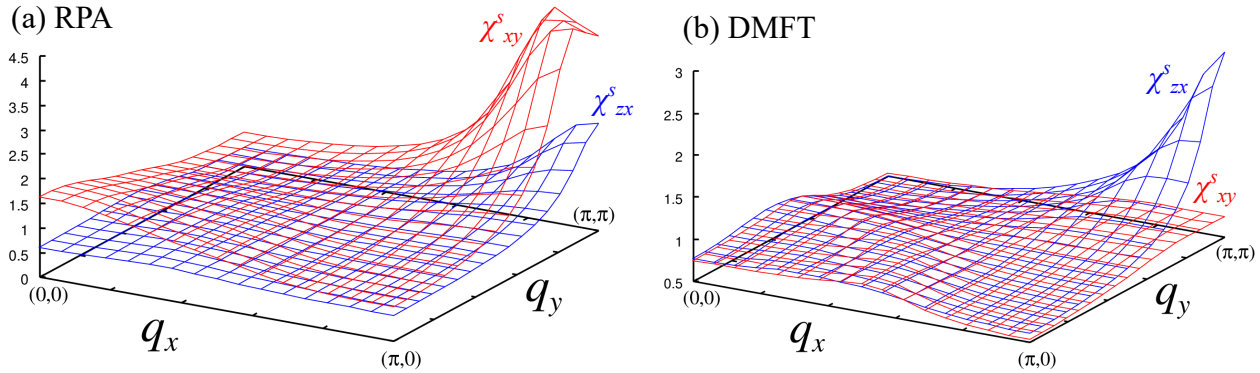


Figure 3.3: Orbital-resolved spin susceptibility in $q_x$-$q_y$ plane for RPA (a) and DMFT (b) at $q_z = 0$ and $i\omega_n = 0$. Here, $f_d = 0.3$ and $\alpha_s = 0.936$ for RPA, and $f_d = 0.5$ and $\alpha_s = 0.953$ for DMFT.

## 3.4 Summary and Discussion

In the present chapter, we investigate 16-band $d$-$p$ model on FeSe in ambient pressure within the dynamical mean-field theory. The correlation effect on the self-energy, the magnetic and orbital fluctuations and its derived superconductivity are revealed. We find that the dissipation of a shallow hole pocket occurs by on-site Coulomb interaction which corresponds to the orbital depend band lifting observed by the recent ARPES and the QO experiments. Furthermore, inter-site orbital-polarization Coulomb interaction between iron $d$ orbital and selenium $p$ orbital drives an electric orbital order in absence of the low-energy commensurate spin response. We also calculate the superconducting gap structure in orbital ordered phase by using the linearized Eliashberg equation, and find that $s_{\pm}$-wave pairing is realized where the $zx/yz$ orbital component of the spin fluctuation is the cause of superconductivity.

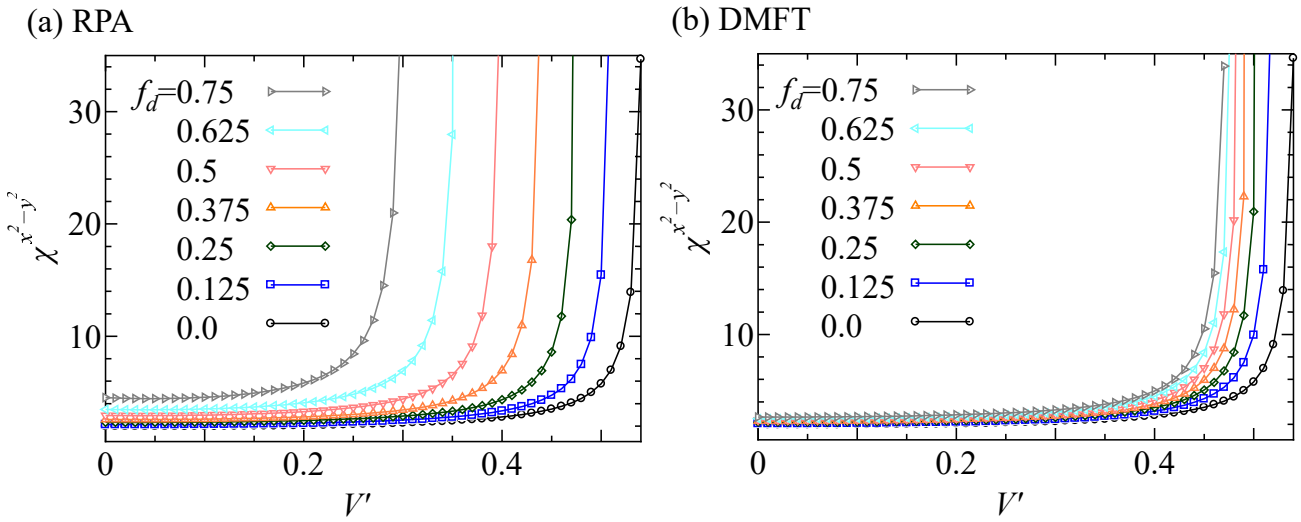


Figure 3.4: Ferro-orbital (nematic) susceptibility for RPA (a) and DMFT (b) at $\boldsymbol{q} = (0, 0, 0)$ and $i\omega_n = 0$. In DMFT, non-local self energy is omitted as mentioned in the text. Thus, the RPA data for $f_d = 0$ coincides with the DMFT one.

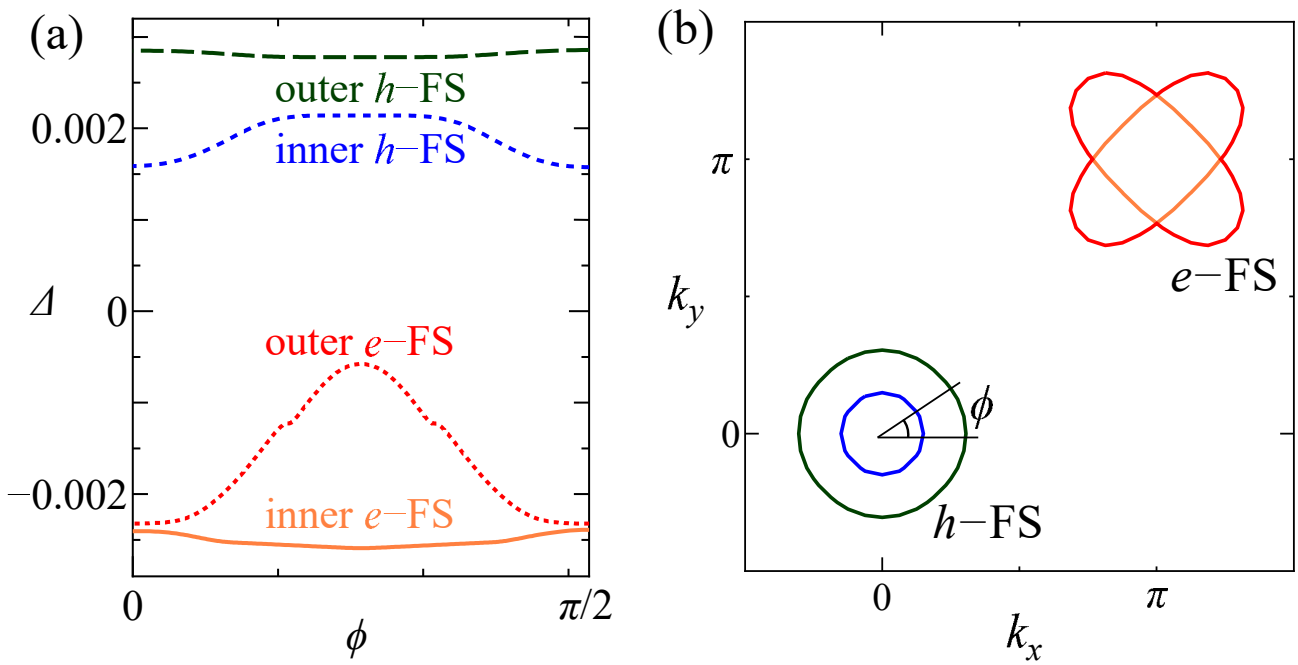


Figure 3.5: (a) Superconducting gap function on Fermi surface at $k_z = 0$ and $i\varepsilon = i\pi T$ for $f_d = 0.5$, $V' = 0$, and $\lambda = 0.859$. (B) Interacting Fermi surface at $k_z = 0$.

# Chapter 4

# Electronic state of FeSe under pressure

Recent experiments have observed that a structural transition temperature $T_s$ is suppressed by applying pressure, whereas a antiferromagnetic transition temperature $T_m$ becomes finite. The antiferromagnetic dome is stabilized in the wide pressure region, partially coexisting with the superconducting temperature at the maximum $T_c \sim 37\,\mathrm{K}$. In order to understand the pressure dependence of $T_s$, $T_m$, and $T_c$ in bulk FeSe, this chapter gives the investigation of realistic low-energy models at ambient and under pressure. The model at ambient pressure reproduces experimental Fermi surface. We reveal that pressure effect on lattice structure from first-principles clearly shows that the height of Se, which is key parameter for the mixing of $xy$ orbital, arise from Fe plane by applying pressure. As a result, a hole Fermi surface, which primarily consists of $xy$ orbital, supersedes the $zx/yz$ hole Fermi surfaces. A hybridization of $zx/yz$ orbital on the Fermi surface affects $T_s$, so that $T_s$ decrease with pressure, consistently with experiments, where $zx/yz$ orbital fluctuation enhancement is governed by the $d$-$p$ orbital polarization interaction. The hybridization of $xy$ orbital strengthens the antiferromagnetic fluctuation from low pressure region. Thus, the origin of the opposite pressure dependence between $T_s$ and $T_m$ is clarified from the topological change of hole Fermi surface derived by the lattice parameter. The enhancement of spin fluctuation and the spread of total bandwidth affect $T_c$, resulting in the double-dome pressure dependence of eigenvalue $\lambda$ in the Eliashberg equation.

The organization of this chapter is as follows. Sec. 4.1 gives a review of FeSe under pressure. Sec. 4.2 studies the specific electronic structure from first-principles band calculation. The effective low-energy tight-binding model is derived in this section. Sec. 4.3 gives a calculation result of the RPA in tetragonal and orthorhombic phase. This section gives our main results that experimentally observed temperature/pressure phase diagram is almost perfectly described. Summarization of the present chapter is in Sec. 4.4.

## 4.1 Introduction

The discovery of iron-based superconductors [1] is one of the highlights of condensed matter physics and offer us a place to understand fundamental phenomena of electronic properties. In most iron-based superconductors, the superconductivity is found in the proximity of a magnetic ordered state. Just above the magnetic ordered state (in the 1111 systems such as LaFeAsO and 122 system such as $BaFe_2As_2$), a structural (nematic) transition from the tetragonal to the orthorhombic is realized, that spontaneously breaks the four-fold symmetry $C_4$. The relation between the structural transition and the magnetic ordered phase has been a controversial issue, whose understanding may provide

the insights into the pairing mechanisms and symmetries [33, 34, 39, 126, 127, 51, 54]. To elucidate the origin of the structural transition above the magnetic order, the spin-nematic theory [9, 49] and the orbital order theory [128, 55] has been proposed intensively. The microscopic pictures of these theories are the spin-quadrupole order induced by the spin fluctuation [9] and the orbital-spin mode-coupling characterized by the Aslamazov-Larkin vertex correction [55]. On the other hand, another candidate of the orbital order mechanism was suggested in Ref. [62] by taking into account an orbital polarization interaction, which is derived from the orbital dependence of the intersite $d$-$p$ Coulomb integrals between Fe $d_{zx/yz}$ orbitals and As $p_{x/y}$ orbitals.

FeSe is a curious material among the iron-based superconductors, that give us a remarkable phase diagram as a function of pressure. The early powder sample study [106] shows that the superconducting transition temperature $T_c \sim 9\,\mathrm{K}$ at ambient pressure can be enhanced by $T_c \sim 37\,\mathrm{K}$ at the pressure $\sim 9\,\mathrm{GPa}$. The polycrystalline sample of $\mathrm{FeSe}_{1-x}$ was investigated in the early NMR measurements and the muon-spin rotation ($\mu$SR) experiments [129, 130, 131]. According to these results, the spin fluctuation is enhanced by pressure up to $\sim$2.2 GPa [129] and a pressure-induced antiferromagnetic ordered state is stabilized above $\sim$1 GPa [130, 131]. More recent studies on single crystals revealed comprehensive and complex $T$-$P$ phase diagram from macro- and microscopic measurements under high pressure [132, 21, 133, 134, 135, 136]. There is a consensus on the pressure-induced magnetic transition temperature in transport measurements [132, 21]. Although the deviation of transition temperature $T_m$ is observed between $\mu$SR and resistivity, the discrepancy is explained by a local magnetic volume fraction [132]. Remarkably, a non-magnetic structural transition $T_s$ is quickly suppressed by pressure up to $P \sim 1\,\mathrm{GPa}$ [133] and the antiferromagnetic ordered state is stabilized in a wide pressure region ($1 < P < 6\,\mathrm{GPa}$) with a dome shape at the maximum value of $T_m \sim 45\,\mathrm{K}$ ($P \sim 4.8\,\mathrm{GPa}$) [21]. Thus, the superconductivity meets three quantum critical points with increasing $P$. One is nematic quantum critical point, the others are magnetic one accompanied by the enhancement of $T_c$. It is noteworthy that the stripe-type antiferromagnetic order breaks not only time-reversal symmetry but $C_4$ symmetry. Simultaneous first-order magnetic and structural transitions was observed in recent transport measurement [134].

In contrast to the 1111 and 122 systems, FeSe at ambient pressure shows a very weak antiferromagnetic fluctuation above $T_s$. The absence of the low-energy spin response seems to be consistent with orbital polarization interaction mechanism[62] which merely relies on the orbital degrees of freedom in principle, as mentioned above. In this mechanism, the ferro-orbital fluctuation mediates an attractive pairing within each of an electron- and a hole-Fermi surfaces almost independently of each other, while the antiferromagnetic fluctuation causes the pair scattering between the electron and hole Fermi surfaces resulting in the $s_{\pm}$-wave pairing. Then, the antiferromagnetic and ferro-orbital fluctuations cooperatively enhance $T_c$ without any competition by the $\boldsymbol{q}$-space segregation of the two fluctuations. Furthermore, the average value of the intersite Coulomb integrals are large for the FeSe relative to those for the 1111 and the 122 systems[32]. Thus, by considering suitable intersite $d$-$p$ Coulomb integrals, the FeSe is expected to have larger orbital polarization interaction than the 1111 and 122 systems.

## 4.2 Construction of the $d$-$p$ model under pressure

In this section, we present a detailed analysis of pressure dependence of FeSe in paramagnetic phase. To predict accurately the electronic structure from the first principles, we employ a downfolding scheme in the following. We construct the global band structure using the density functional theory

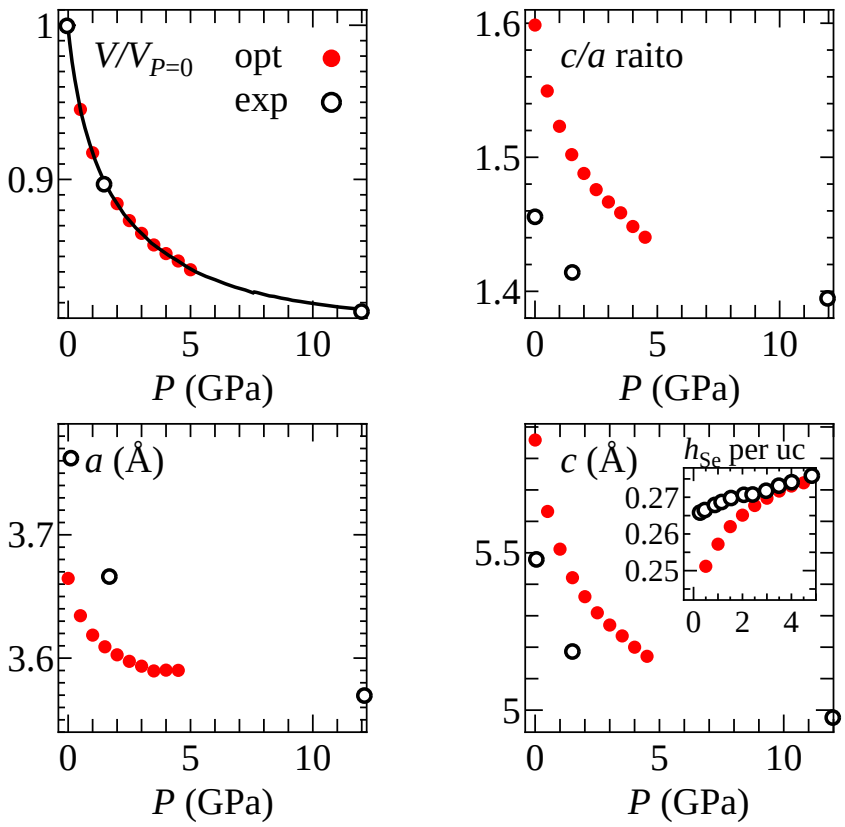


Figure 4.1: Experimental [106, 137] and optimized structural parameters. The optimization is done for internal coordinates $h_{\mathrm{Se}}$ and $c/a$ ratio with constant unit-cell volume.

within the generalized gradient approximation [123, 124]. To minimize the lattice energy from first principles, we start with the structural optimization on internal coordinates $h_{\mathrm{Se}}$ and $c/a$ ratio in each pressure with the space group $P4/nmm$ and experimental crystal parameters of FeSe [106, 137]. Figure 4.1 shows the optimized and the experimental crystal parameters. We have optimized the structure requiring Se atomic force to be less than 0.5 mRy/bohr. The optimized lattice parameter $a$ is 2 % smaller (and $c$ is 2 % larger) than these in experiments at ambient pressure. The pressure dependence of these parameters is qualitatively consistent with experiments. We construct a tight-binding Hamiltonian exploiting the maximally localized Wannier functions including Fe-3$d$ orbitals and Se-4$p$ orbitals using the WANNIER90 code [121] through the WIEN2WANNIER interface [122]. From the angular resolved photoemission spectroscopy (ARPES) and the quantum oscillation experiments at ambient pressure [19], the quasi two-dimensional hole pocket with $zx/yz$ character and two electron pockets with $zx/yz$ and $xy$ character was observed. Since the experimentally observed Fermi surfaces even at ambient pressure give the deviation with the band calculation of FeSe, we introduce the additional hopping shift $\delta t_l$ for $l = zx/yz$ and $xy$ orbitals as $(\delta\varepsilon_{zx/yz}, \delta t^{\mathrm{nn}}_{zx/yz}, \delta t^{\mathrm{nnn}}_{zx/yz}) = (0, -0.03, -0.03)$ and $(\delta\varepsilon_{xy}, \delta t^{\mathrm{nn}}_{xy}, \delta t^{\mathrm{nnn}}_{xy}) = (-0.025, +0.0125, -0.06625)$ [eV] in order to reproduce the Fermi surfaces [113, 110, 138]. Since the experimental Fermi surface under pressure has not been detected clearly, we introduce the same $\delta t_l$ for each pressure as a simplified approximation.

Figure 4.2 shows the band structures together with orbital weight at $P = 0.0, 1.5, 3.0$, and 4.5 GPa. The low-energy band structure of $P = 0.0$ GPa is in good agreement with the ARPES results above $T_s$ [19]. It seems that the band structure of 4.5 GPa resembles that of 0.0 GPa, but total bandwidth is widen ∼1 eV by usual pressure effect. Furthermore, by comparing the band structure near the Fermi level at Γ point [see Fig. 4.2(e)], one sees a characteristic orbital energy shift. Namely, a hole band of mainly $xy$ orbital character at $E_\Gamma \sim -50$ meV is pushed upward to ∼25 meV and two-degenerated hole bands of mainly $zx/yz$ orbital character at $E_\Gamma \sim 60$ meV are pushed downward to ∼−25 meV, which indicates topological transition induced by pressure effect from the first-principles band calculation. It is worth noting that the consequences of transfer integrals between $xy$ orbitals together with the Se height are significant for orbital energy shift[37] and this will be discussed later in detail. To get more insight about the low energy property, the Fermi surfaces at $P = 0.0, 1.5, 3.0$, and 4.5 GPa with $zx/yz$ and $xy$ orbital weights are shown in Fig. 4.3. The Fermi surfaces at 0.0 GPa which consist of two-hole and two electron pockets are consistent with experiment at ambient pressure. In this case, the electron($zx/yz$)-hole($zx/yz$) Fermi surface nesting with wave vector $\boldsymbol{q} = (\pi, \pi)$ is most important. By applying pressure, one can see that the two small hole pockets deform and shrink, and then new hole pocket of mainly $xy$ orbital character arises, while two electron pockets slightly change the shape. In the configuration of $P = 3.0$ and 4.5 GPa, the electron($xy$)-hole($xy$) Fermi surface nesting with wave vector $\boldsymbol{q} = (\pi, \pi)$ is most important in contrast to that of 0.0 GPa.

Now let us turn to discuss why the hole band of $xy$ orbital character pushed upward by increasing pressure. This is attributable to the lattice parameter of Se height obtained from first principles [see also Fig. 4.1(b) and 4.4(d)] which tend to increase as $P$ increase. This has been recognized from an early stage of the study on the 1111 system, that the lattice parameter of the pnictogen hight determines the mixture of $xy$ orbital contribution, and in turn, the construction of the hole Fermi surface at Γ point[37]. To examine this effect on FeSe under pressure, Figure 4.4(a)-(c) show the pressure dependences of intra-orbital hopping integrals $t_l$ and $t_{lm}$ between the lattice vector illustrated in the inset of the Figure 4.4(a)-(c) for $(l, m) = (zx/xy, x)$. These hopping integrals tend to upward with increasing $P$ owing to the decrease in unit-cell volume. The $xy$ hopping integrals has considerably large pressure dependence than the $zx$ one. The difference increases as $P$ increases in the low pressure region, and for further increasing $P$, it becomes to diminish for $P > 3.5$ GPa.

## 4.3 RPA calculation of spin and orbital fluctuation and superconductivity

### 4.3.1 Calculation method

Next, we address the interacting part of the Hamiltonian $H_{\rm int}$ which consists of the multi-orbital Coulomb interaction $H_{dd}$ between $3d$ electrons on Fe site and the inter-site Coulomb interaction $H_{dp}$ between Fe and Se sites

$$H_{int} = H_{dd} + H_{pp} + H_{dp} \tag{4.1}$$

which have been defined in the previous Chapter [see Eqs. (3.2)-(3.4) in Sec. 3.2]. We apply random phase approximation (RPA) to each model where the self energy correction was neglected. The spin (charge-orbital) susceptibility in RPA is given by

$$\hat{\chi}^{s(c)}(q) = \hat{\chi}^0(q) \left[\hat{1} - (+)\hat{\Gamma}^{s(c)}(\boldsymbol{q})\hat{\chi}^0(q)\right]^{-1}, \tag{4.2}$$

where $q = (\boldsymbol{q}, i\omega_n)$ with the wave vector $\boldsymbol{q}$ and bosonic Matsubara frequency $\omega_n = 2n\pi T$. $\hat{\Gamma}^{s(c)}(\boldsymbol{q}) = \hat{\Gamma}^{s(c),0}(\boldsymbol{q})$ is the spin (charge-orbital) vertex. The bare vertex $\hat{\Gamma}^{s(c),0}$ has been defined in Sec. 3.2. In Eq. (4.2), the irreducible susceptibility $\hat{\chi}^0(q)$ has been defined in Sec. 2.2.

To examine the superconductivity, we solve the linearized Eliashberg equation [see Eq. (2.6) in Sec. 2.2], and obtain the superconducting gap function $\hat{\Delta}(k)$ with the eigenvalue $\lambda$ which becomes unity at the superconducting transition temperature $T_c$, where the effective pairing interaction for the spin-singlet state is given as

$$\begin{aligned} \hat{V}(q) &= \frac{3}{2}\hat{\Gamma}^s\hat{\chi}^s(q)\hat{\Gamma}^s - \frac{1}{2}\hat{\Gamma}^c(\boldsymbol{q})\hat{\chi}^c(q)\hat{\Gamma}^c(\boldsymbol{q}) \\ &+ \frac{1}{2}\left(\hat{\Gamma}^s + \hat{\Gamma}^c(\boldsymbol{q})\right). \end{aligned} \tag{4.3}$$

We perform RPA calculations for each model with fixed temperature $T = 0.03\,\mathrm{eV}$. We employ the Coulomb interaction parameters on Fe site $U_{ll}, U'_{ll'}, and J_{ll'} = J'_{ll'}$ obtained from cRPA method [32] by multiplying a reduction factor $f_d = 0.279$ ($\bar{U}_d = 2.0\,\mathrm{eV}$), since the RPA overestimates the magnetic fluctuation and the magnetic ordered state. We introduce $V' = 0.464\,\mathrm{eV}$, which was found to be smaller than $U_{pd} = 1.7\,\mathrm{eV}$ from Ref. [32], and slightly larger than $V'$ of Ref. [62]. $V'$ is just a parameter to adjust the orbital fluctuation strength, which was determined to reproduce the experimental observations at ambient pressure, i.e. to satisfy the condition that the orbital fluctuation is larger than the spin fluctuation. We use $32 \times 32$ $\boldsymbol{k}$-meshes and 512 Matsubara frequencies. Hereafter, we mainly discuss the total spin susceptibility $\chi^s(\boldsymbol{q}, 0) = \sum_{l,l'} \chi^s_{l,l;l',l'}(\boldsymbol{q}, 0)$ at Fe site, and the orbital susceptibility $\chi^c_{x^2-y^2}(\boldsymbol{q}, 0) = \sum_{l_1,l_2,l_3,l_4} o^{l_1 l_2}_{x^2-y^2} \chi^c_{l_1,l_2;l_3,l_4}(\boldsymbol{q}, 0) o^{l_4 l_3}_{x^2-y^2}$ with $o^{zx,zx}_{x^2-y^2} = -o^{yz,yz}_{x^2-y^2} = -(\sqrt{3}/2) o^{3z^2-r^2,x^2-y^2}_{x^2-y^2} = 1$ [51]. The spin (charge) Stoner factor $\alpha_{s(c)}$ is given by the maximum eigenvalue of $\hat{\Gamma}^{s(c)}(\boldsymbol{q})\hat{\chi}^0(\boldsymbol{q}, 0)$, which is taken as a measure of $T_{m(s)}$. In a previous study of Ref. [139], the RPA was adopted in the five-orbital model, where both $\alpha_s$ and the eigenvalue of the Eliashberg equation was found to be monotonically diminished by applying pressure which does not agree with the experimental observations. Also, the pressure dependence of $\alpha_c$ was not clarified.

### 4.3.2 Spin and orbital fluctuation in tetragonal state

Figure 4.5(a) and 4.5(b) show the $\boldsymbol{q}$ dependences of the orbital and spin susceptibility $\chi^c_{x^2-y^2}$ and $\chi^s$, respectively, for $P = 0.0, 0.5, 1.5, 2.5, 3.5$, and $4.5\,\mathrm{GPa}$. One observes that the orbital susceptibility for $\boldsymbol{q} = (0, 0)$ is enhanced owing to the $d$-$p$ orbital polarization interaction at ambient pressure. It decreases as $P$ increases, since the shrink of the two hole Fermi surfaces yields the reduction of $zx/yz$ orbital contribution on the Fermi energy. Conversely, the spin susceptibility for $\boldsymbol{q} = (\pi, \pi)$ is strongly enhanced by applying pressure for $P < 3.5\,\mathrm{GPa}$, and drops down moderately for $P > 3.5\,\mathrm{GPa}$.

In order to understand this behavior, we study the orbital resolved spin susceptibility. In low $P$, the total spin fluctuation $\chi^s$ is composed of mainly $\chi^s_{l,l;l,l}$ of $l = zx/yz$, while the one of $l = xy$ is very weak. This is due to the Fermi surface nesting of the $zx/yz$ orbitals with the wave vector $\boldsymbol{q} = (\pi, \pi)$. However, the spin fluctuation is not so strong owing to the smallness of Fermi surfaces. In high $P$, the hole Fermi surface, which primarily consists of $xy$ orbital, supersedes the $zx/yz$ hole Fermi surfaces, and then the $xy$ orbital component of $\chi^s_{l,l;l,l}$ is dominant, which originates from the $xy$ intra-orbital nesting between the electron and hole Fermi surfaces. In contrast to $\chi^s$, $\chi^c_{x^2-y^2}$ is primary composed of $\chi^c_{l,l;l',l'}$ of $(l, l') = (zx/yz, zx/yz)$ with $\boldsymbol{q} = (0, 0)$ in all pressure. This component does not rely on the electron-hole Fermi surface nesting of $zx/yz$ orbital with $\boldsymbol{q} = (\pi, \pi)$ and also the $xy$ orbital

contribution on Fermi surface. In other words, the $d$-$p$ orbital polarization interaction only enhances the ferro-orbital fluctuation owing to the the $zx/yz$ orbital contribution on Fermi surfaces. Note that the charge susceptibility $\sum_{l,l'} \chi^c_{l,l;l',l'}$ with $\boldsymbol{q} = (0,0)$ is also enhanced owing to the $d$-$p$ Coulomb interaction $V$.

Figure 4.5(c) shows the spin and charge Stoner factors $\alpha_s$ and $\alpha_c$ as a function of pressure. Similarity to the spin and orbital susceptibility, in low pressure region up to 3.5 GPa, $\alpha_s$ largely increases while $\alpha_c$ is diminished, leading to remarkable opposite pressure dependence between the spin and orbital fluctuations due to the reasons as mentioned above. In high pressure region, both $\alpha_s$ and $\alpha_c$ are diminished and $\alpha_s$ exhibits a single-dome shape at 3.5 GPa. These results are in good agreement with the experimental phase diagram of $T_{s(m)}$ vs $P$ in Ref. [21] [shown in Fig. 4.5(d)].

### 4.3.3 Superconductivity in orthorhombic state

In this subsection, we address the pressure-induced superconductivity mediated by the pressure-induced spin fluctuation in orthorhombic phase. We study uniform orbital order and $\boldsymbol{k}$-dependent orbital order states proposed so far. In the latter case, we assume $\delta\Sigma_{zx(yz)} = -(+)\frac{1}{4}(\delta E^{\Gamma}_{\rm nem} + \delta E^{M}_{\rm nem}) + (-)\frac{1}{8}(\delta E^{M}_{\rm nem} - \delta E^{\Gamma}_{\rm nem})(\cos k_x + \cos k_y)$, namely a sign reversing orbital splitting, which is observed in ARPES study. Here, $\delta E_{\rm nem}$ is the orbital energy splitting $E_{zx} - E_{yz}$ at the $\Gamma$ and M point. We set $\delta E^{\Gamma}_{\rm nem} = -0.05\,\mathrm{eV}$ and $\delta E^{M}_{\rm nem} = 0.15\,\mathrm{eV}$. This orbital order yields a good nesting of the Fermi surface for the $yz$ and $xy$ orbital components, but ill nesting for $zx$ component. Therefore, The $yz$ and $xy$ spin fluctuation is enhanced. Thus, the eigenvalue $\lambda$ of the Eliashberg equation exhibits broad enhancement with a double-dome shape [see Figure 4.6(a)]. The acute peak at $P = 3.5\,\mathrm{GPa}$ is due to the proximity to the antiferromagnetic order. Indeed, this peak shifts to low pressure as $f_d$ increases [see Fig. 4.6(b)]. The non-monotonous increase such as double-dome $\lambda$ is in good agreement with the experimental $T_c$. The nodal-like $s_{\pm}$-wave pairing is stabilized, and then indicates the consistency with the STM and the ARPES experiments.

## 4.4 Summary and Discussion

In summary, we have investigated the spin-charge-orbital fluctuation under pressure in the 16-band $d$-$p$ Hubbard model for iron-based superconductor FeSe in paramagnetic tetragonal phase by using the random phase approximation with respect to the Fe $3d$ Coulomb interaction and Fe and Se $d$-$p$ orbital polarization interaction. A pressure effect on electronic states was derived from first principles band calculation by optimizing the experimental lattice parameters. It has been found that the optimized lattice parameters are qualitatively consistent with these in experiments as a function of pressure. The Fermi surfaces obtained from the effective tight-binding model clearly indicates the signature of the topological transition with increasing pressure. Furthermore, we have explained the spin and orbital orders in bulk FeSe under pressure. The ferro-orbital order is monotonically suppressed with pressure and the antiferromagnetic order is robustly realized with a dome shape at 3.5 GPa, in good agreement with experiments.

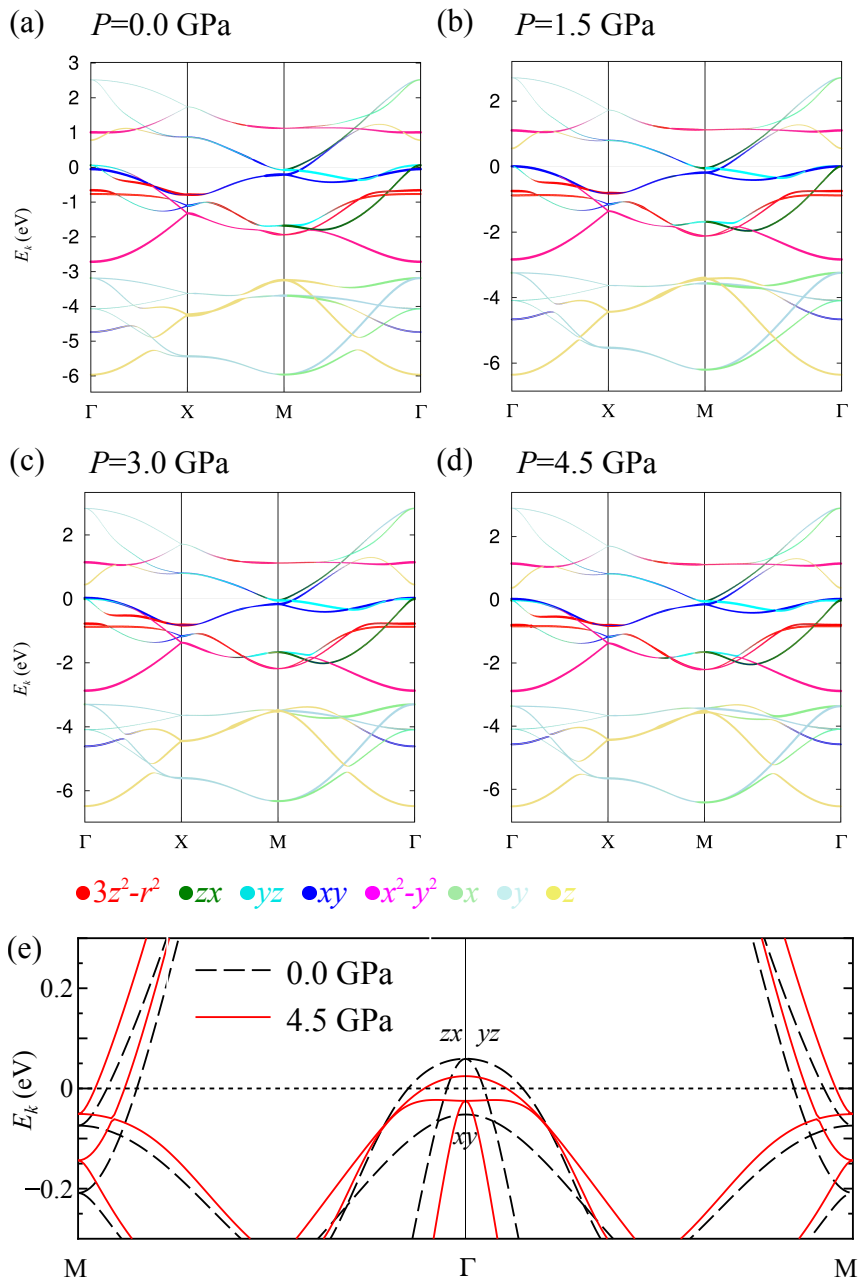


Figure 4.2: Band structures of FeSe at $P = 0.0, 1.5, 3.0$, and $4.5\,\mathrm{GPa}$ obtained by effective tight-binding models, where orbital weights are plotted as $3z^2 - r^2$ (red), $zx$ (green), $yz$ (cyan), $xy$ (blue), $x^2 - y^2$ (pink), $x$ (light-green), $y$ (light-blue), $z$ (light-goldenrod).

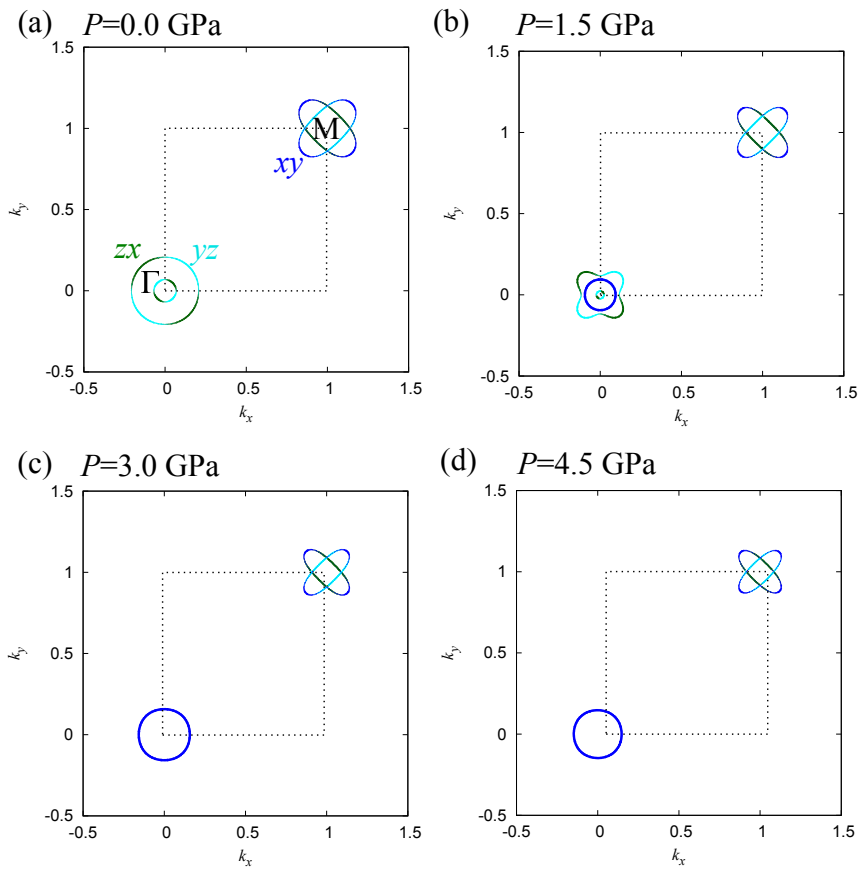


Figure 4.3: Fermi surfaces of FeSe at $P = 0.0, 1.5, 3.0$, and 4.5 GPa obtained by effective tight-binding models, where orbital weights are plotted as $zx$ (green), $yz$ (cyan), $xy$ (blue).

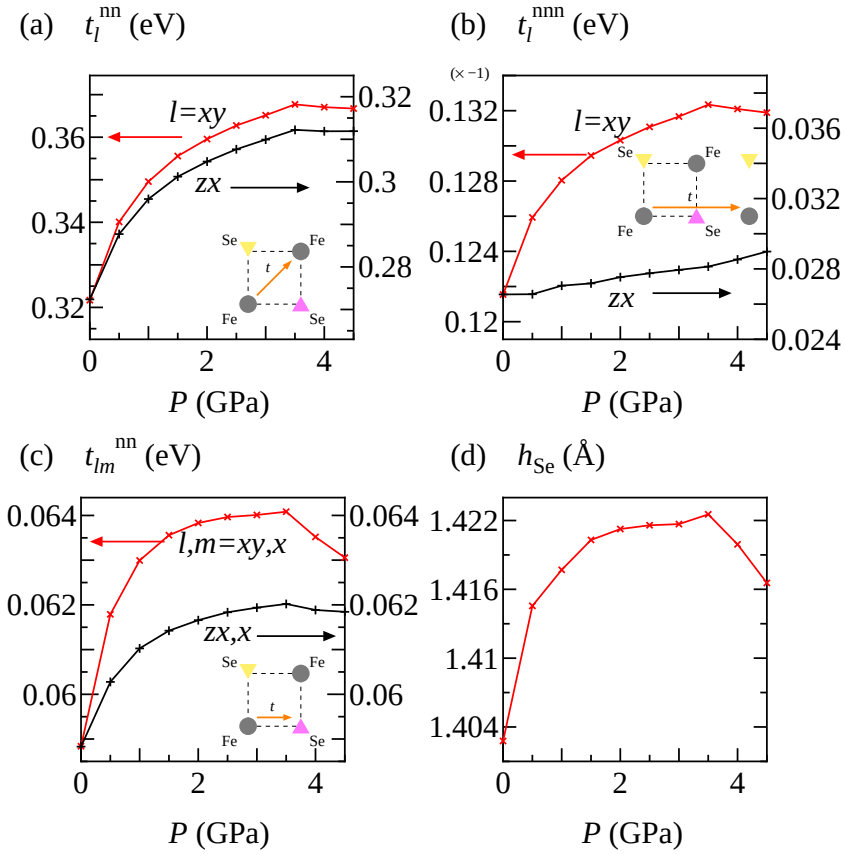


Figure 4.4: Hopping integrals for (a) intra-orbital nearest neighbor transfer, (b) intra-orbital next nearest neighbor transfer between Fe atoms, and (c) inter-orbital nearest neighbor transfer between an Fe and a Se atoms with $l = zx, xy$ and $m = x$ as a function of pressure. (d) Se height above the Fe plane.

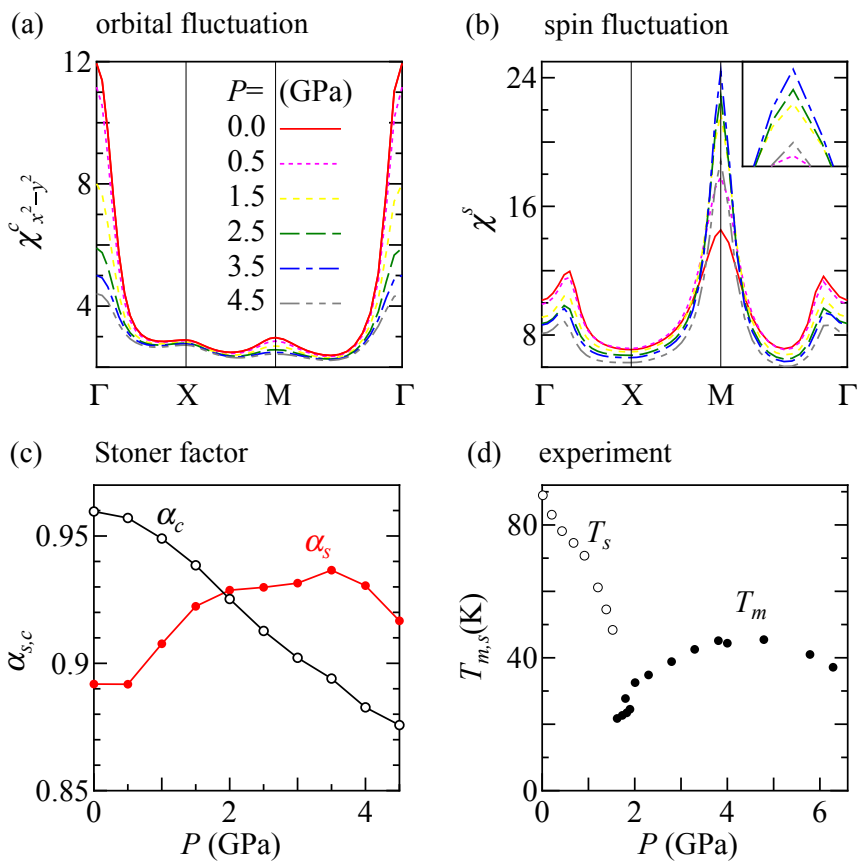


Figure 4.5: $\boldsymbol{q}$ dependence of (a) orbital and (b) spin susceptibilities of FeSe at $P = 0.0, 0.5, 1.5, 2.5, 3.5,$ and 4.5 GPa. (c) Pressure dependence of charge and spin Stoner factors, which is taken as a measure of $T_s$ and $T_m$, respectively. (d) Experimental result of $T_{m(s)}$ vs $P$ from Ref. [21].

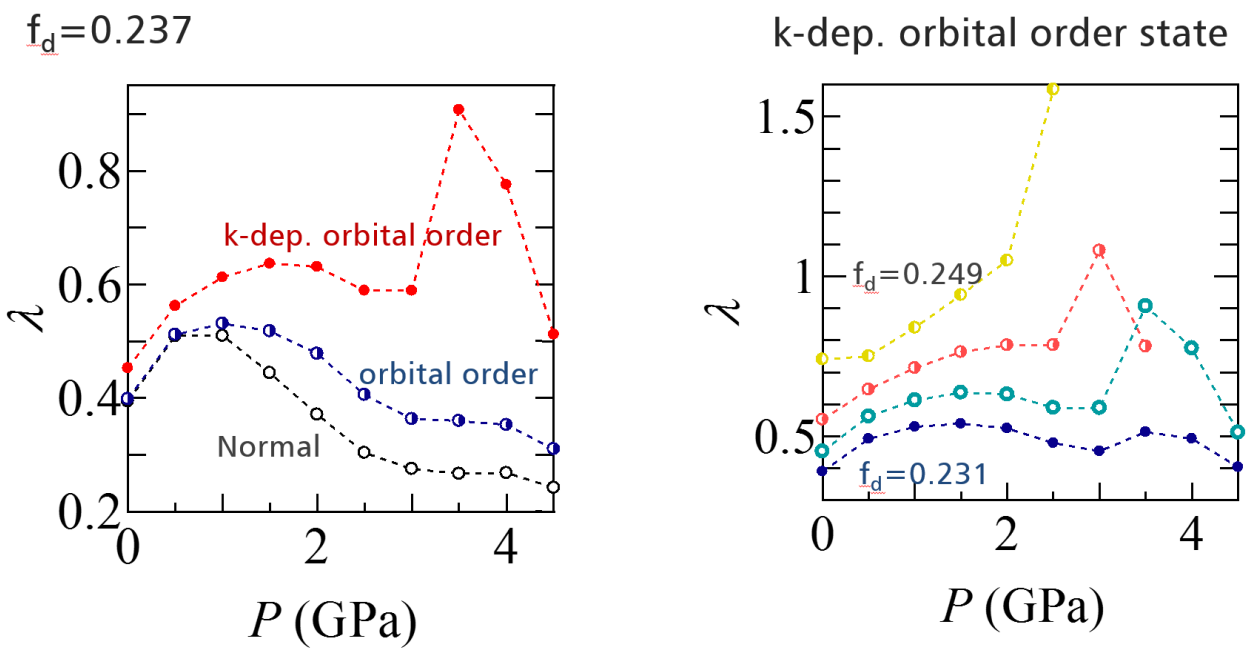


Figure 4.6: (a) Pressure dependence of the superconducting eigenvalue for $f_d = 0.237$ in tetragonal, orbital order, and $k$-dependent orbital order states. (b) Pressure dependence of the superconducting eigenvalue for several $f_d$ values in $k$-dependent orbital order states

# Chapter 5

# Conclusion

This thesis reported some theoretical studies on iron-based superconductors.

In Chap. 1, we reviewed basic properties of iron-based superconductors. The recently discovered iron-based superconductors $LaFeAsO_{1-x}F_x$ exhibits the antiferromagnetic transition and the structural transition at low temperature. The iron-based compounds are multi-orbital system of a semimetal phase, differently from the copper oxide superconductors. The spin fluctuation and the orbital fluctuation are enhanced toward two transition temperatures, and hence two distinct pairing mechanisms: (I) the $s_{\pm}$-wave mediated by the spin fluctuation and (II) the $s_{++}$-wave mediated by the orbital fluctuation were proposed. Moreover, the distinct phase diagramss are one of the characteristic feature of the iron-based superconductors. Hence it is also an important issue why the iron-based family shows such remarkable material dependence, despite having the analogous crystal structure. For instance, FeSe shows a structural transition at $\sim$ 90K and the superconducting transition at $\sim$ 9K without long-range magnetic order. Phase diagram as a function of pressure in FeSe shows that the structural transition is quickly suppressed by pressure, while the antiferromagnetic transition is stabilized in a wide pressure region with a dome shape. The superconducting transition temperature can be first enhanced by pressure, and then drops down slightly before arising again, and finally reaches to $\sim 37\,\mathrm{K}$ at pressure $\sim 6.5\,\mathrm{GPa}$.

Chap. 2 presented the analysis of electronic state coexisting the spin and orbital fluctuations in the five-orbital Hubbard model for iron-pnictides. We pointed out the vertex function is largely renormalized with significant orbital dependence, owing to the competition of the spin and orbital fluctuations. Solving the linearized Eliashberg equation with the derived effective pairing interaction, the gap function with the sign change between two-hole Fermi surfaces, in addition to the sign change between a hole and an electron ones, namely "hole-$s_{\pm}$-wave", is stabilized. Comparing the hole-$s_{\pm}$-wave with experimental results, it was explained that the hole-$s_{\pm}$-wave may occur in such specific compound as LiFeAs. Several authors [77, 75, 78] proposed the orbital antiphase $s_{\pm}$-wave and hole-$s_{\pm}$-wave symmetries as promising pairing states for LiFeAs, but the relative signs of the gap function on the FSs are different from the present result. The most significant difference between the previous and present hole-$s_{\pm}$-wave states was the pairing mechanism: the most dominant pairing interaction in the present theory is between the inner and the outer hole FSs at $\boldsymbol{q} \sim (0,0)$ mediated by the largely enhanced FM fluctuation, which was not taken into account in the previous theories but was observed in the $\mu$SR experiment [73].

Chap. 3 gave a detailed analysis of 16 band $d$-$p$ model for FeSe. One-particle spectral function was derived from the dynamical mean-filed theory, including the Fe-3$d$ Coulomb interaction together

with the Se-4$p$ Coulomb interaction. The spectral function of $xy$ orbital exhibits the deviation from first-principles calculation, owing to the orbital dependence of the 3$d$ Coulomb interaction. The absence of a hole band composed of $xy$ orbital agrees with the experiments with the ARPES and the quantum oscillation. The experimental results of the NMR spin-relaxation rate, in which the spin fluctuation is very weak above the structural transition, was verified by calculating spin susceptibility. Furthermore, we have studied the effect of the inter-site Coulomb interaction between Fe-$d$ orbital and Se-$p$ orbital within the random phase approximation, and the orbital fluctuation was found to be enhanced owing to the orbital-dependent interaction. The enhancement explains the elastic constants in the ultrasonic experiments and the susceptibility in the Raman scattering experiments. These results not only reproduce the key properties in FeSe well, but also provide a helpful perspective to investigate the strongly correlated multi-orbital system, that is the evidence of the orbital-dependent Coulomb interaction.

The theme of Chap. 4 was about the issue, what state is stabilized by applying pressure on FeSe, where the electronic state in the ambient pressure was revealed in Chap. 3. The pressure dependences of several physical quantities are clarified by analyzing the effective model derived from the first-principles calculation, using lattice parameters under pressure. The results show that the hole Fermi surface originating from $xy$ orbital is induced by pressure, and the spin fluctuation is strongly enhanced owing to the nesting between that and electron Fermi surface. It is elucidated that Se atoms height (distance from the Fe plane) is crucial for these pressure effects. Moreover, superconducting eigenvalue in orbital ordered state shows double-dome shape as a function of pressure, consistent with the experimental phase diagram. Here, the nodal-like $s_{\pm}$-wave pairing is stabilized, and is consistent with the STM and the ARPES experiments. As mentioned above, this study explains pressure/temperature phase diagram by means of the spin and orbital fluctuation theory.

Finally, we briefly comment on a evaluation of the orbital polarization interaction. Our estimation with the use of hydrogenlike atomic wave functions yields a considerably large value of the orbital polarization interaction $\sim 0.3 - 0.5\,\mathrm{eV}$. However, other estimation using the realistic Wannier orbital indicates a small value $\sim 0.1\,\mathrm{eV}$ at most [140]. Considerably small value of the orbital polarization interaction cannot enhance the orbital fluctuation sufficiently than the spin fluctuation, but vertex correction for this interaction is neglected in this thesis. Thus, to get more conclusive evidence, we need to obtain the vertex functions with precise $k$-dependence beyond the single-site DMFT, and these treatment remains an open and very challenging problem.

# Acknowledgment

First, I would like to express my sincere gratitude to Prof. Y. Ōno for his enormous help and support during my five years graduate course. He supported my study in all aspects such as consultations of the research tasks, sharing the valuable problems, discussion about the results, and suggestions to give a presentation and write in English. I would like to acknowledge Dr. T. Yamada on the early stage of my research. Through the investigations with his support, I acquired basic knowledges and questions on condensed matter of physics, which was the basis of my Doctoral study. I would like to appreciate Dr. Y. Yanagi for helping me in my postdoctoral application and collaboration. I am impressed with his ingenuity and deep knowledges of physics. I would like to thank Prof. R. Settai, Prof. T. Takimoto, Prof. A. Yoshimori, and Prof. K. Okunishi for giving me insightful comments and advices on my thesis. I would also like to acknowledge financial support I have received over the past one year from the Japan Society for the Promotion of Science (JSPS). Finally, I would like to thank my parents for their support and encouragement during my Master and Doctoral courses.

# List of publications

## Published papers related to the thesis

1. J. Ishizuka and T. Yamada and Y. Yanagi and Y. Ōno

   *Hole-$s_{\pm}$ state induced by coexisting ferro- and antiferromagnetic and antiferro-orbital fluctuations in iron pnictides*

   J. Phys. Soc. Jpn. **85**, 114709 (2016)

## Published papers not included in the thesis

2. J. Ishizuka and T. Yamada and Y. Yanagi and Y. Ōno

   *Local correlation effects on the $s_{\pm}$- and $s_{++}$-wave superconductivities mediated by magnetic and orbital fluctuations in the five-orbital Hubbard model for iron pnictides*

   J. Phys. Soc. Jpn. **82**, 123712 (2013)

3. J. Ishizuka and T. Yamada and Y. Yanagi and Y. Ōno

   *Dynamical mean-field study on the superconductivity mediated by spin and orbital fluctuations in the 5-orbital Hubbard model for iron pnictides*

   J. Conf. Proc. **3**, 015020 (2014)

4. T. Yamada and J. Ishizuka and Y. Ōno

   *A high-$T_c$ mechanism of iron pnictide superconductivity due to cooperation of ferro-orbital and antiferromagnetic fluctuations*

   J. Phys. Soc. Jpn. **83**, 043704 (2014)

5. T. Yamada and J. Ishizuka and Y. Ōno

   *Metal-insulator transition and superconductivity in the two-orbital Hubbard-Holstein model for iron-based superconductors*

   J. Phys. Soc. Jpn. **83**, 044711 (2014)

6. J. Ishizuka and T. Yamada and Y. Ōno

   *Novel s-wave due to coexisting ferro- and antiferromagnetic fluctuations in iron pnictides*

   J. Phys. Conf. Ser. **592**, 012077 (2015)

# Bibliography


[1] Y. Kamihara, H. Hiramatsu, M. Hirano, R. Kawamura, H. Yanagi, T. Kamiya, and H. Hosono, J. Am. Chem. Soc. **128**, 10012 (2006).

[2] T. Hanna, Y. Muraba, S. Matsuishi, N. Igawa, K. Kodama, S. Shamoto, and H. Hosono, Phys. Rev. B **84**, 024521 (2011).

[3] N. Fujiwara, S. Tsutsumi, S. Iimura, S. Matsuishi, H. Hosono, Y. Yamakawa, and H. Kontani, Phys. Rev. Lett. **111**, 097002 (2013).

[4] F. L. Ning, K. Ahilan, T. Imai, A. S. Sefat, M. A. McGuire, B. C. Sales, D. Mandrus, P. Cheng, B. Shen, , and H.-H. Wen, Phys. Rev. Lett **104**, 037001 (2010).

[5] H. F. Fong, P. Bourges, Y. Sidis, L. P. Regnault, A. Ivanov, G. D. Guk, N. Koshizuka, and B. Keimer, Nature **398**, 588 (1999).

[6] M. Ito, H. Harashina, Y. Yasui, M. Kanada, S. Iikubo, M. Sato, A. Kobayashi, and K. Kakurai, J. Phys. Soc. Jpn. **71**, 265 (2002).

[7] S. Iikubo, M. Ito, A. Kobayashi, M. Sato, and K. Kakurai, J. Phys. Soc. Jpn. **74**, 275 (2005).

[8] D. S. Inosov, J. T. Park, P. Bourges, D. L. Sun, Y. Sidis, A. Schneidewind, K. Hradil, D. Haug, C. T. Lin, B. Keimer, and V. Hinkov, Nature Materials **6**, 178 (2009).

[9] R. M. Fernandes, L. H. VanBebber, S. Bhattacharya, P. Chandra, V. Keppens, D. Mandrus, M. A. McGuire, B. C. Sales, A. S. Sefat, and J. Schmalian, Phys. Rev. Lett. **105**, 157003 (2010).

[10] T. Goto, R. Kurihara, K. Araki, K. Mitsumoto, M. Akatsu, Y. Nemoto, S. Tatematsu, , and M. Sato, J. Phys. Soc. Jpn. **80**, 073702 (2011).

[11] Zvyagina, G. A., Gaydamak, T. N., Zhekov, K. R., Bilich, I. V., Fil, V. D., Chareev, D. A., and Vasiliev, A. N., EPL **101**, 56005 (2013).

[12] M. Yoshizawa, D. Kimura, T. Chiba, A. Ismayil, Y. Nakanishi, K. Kihou, C. Lee, A. Iyo, H. Eisaki, M. Nakajima, , and S. Uchida, J. Phys. Soc. Jpn. **81**, 024604 (2012).

[13] J. L. Niedziela, D. Parshall, K. A. Lokshin, A. S. Sefat, A. Alatas, and T. Egami, Phys. Rev. B **84**, 224305 (2011).

[14] R. Mittal, L. Pintschovius, D. Lamago, R. Heid, K.-P. Bohnen, D. Reznik, S. L. Chaplot, Y. Su, N. Kumar, S. K. Dhar, A. Thamizhavel, and T. Brueckel, Phys. Rev. Lett. **102**, 217001 (2009).

[15] H. Ding, K. Nakayama, P. Richard, S. Souma, T. Sato, T. Takahashi, M. Neupane, Y.-M. Xu, Z.-H. Pan, A. V. Fedorov, Z. Wang, X. Dai, Z. Fang, G. F. Chen, J. L. Luo, and N. L. Wang, J. Phys.: Condens. Matter **23**, 135701 (2011).

[16] M. Yi, D. H. Lu, R. Yu, S. C. Riggs, J.-H. Chu, B. Lv, Z. K. Liu, M. Lu, Y.-T. Cui, M. Hashimoto, S.-K. Mo, Z. Hussain, C. W. Chu, I. R. Fisher, Q. Si, and Z.-X. Shen, Phys. Rev. Lett. **110**, 067003 (2013).

[17] S.-H. Baek, D. V. Efremov, J. M. Ok, J. S. Kim, J. van den Brink, and B. Büchner, Nat Mater. **14**, 210 (2015).

[18] P. Massat, D. Farina, I. Paul, S. Karlsson, P. Strobel, P. Toulemonde, M.-A. Masson, M. Cazayous, A. Sacuto, S. Kasahara, T. Shibauchi, Y. Matsuda, and Y. Gallais, Proceedings of the National Academy of Sciences **113**, 9177 (2016).

[19] M. D. Watson, T. K. Kim, A. A. Haghighirad, N. R. Davies, A. McCollam, A. Narayanan, S. F. Blake, Y. L. Chen, S. Ghannadzadeh, A. J. Schofield, M. Hoesch, C. Meingast, T. Wolf, and A. I. Coldea, Phys. Rev. B **91**, 155106 (2015).

[20] Y. Suzuki, T. Shimojima, T. Sonobe, A. Nakamura, M. Sakano, H. Tsuji, J. Omachi, K. Yoshioka, M. Kuwata-Gonokami, T. Watashige, R. Kobayashi, S. Kasahara, T. Shibauchi, Y. Matsuda, Y. Yamakawa, H. Kontani, and K. Ishizaka, Phys. Rev. B **92**, 205117 (2015).

[21] J. P. Sun, K. Matsuura, G. Z. Ye, Y. Mizukami, M. Shimozawa, K. Matsubayashi, M. Yamashita, T. Watashige, S. Kasahara, Y. Matsuda, J.-Q. Yan, B. C. Sales, Y. Uwatoko, J. G. Cheng, and T. Shibauchi, Nat. Commun. **7**, 12146 (2016).

[22] S. Lebegue, Phys. Rev. B **75**, 035110 (2007).

[23] D. J. Singh and M. H. Du, Phys. Rev. Lett. **100**, 237003 (2008).

[24] K. Haule, J. H. Shim, and G. Kotliar, Phys. Rev. Lett. **100**, 226402 (2008).

[25] G. Xu, W. Ming, Y. Yao, X. Dai, S.-C. Zhang, and Z. Fang, Europhys. Lett. **82**, 67002 (2008).

[26] L. Boeri, O. V. Dolgov, and A. A. Golubov, Phys. Rev. Lett. **101**, 026403 (2008).

[27] D. J. Singh and M. H. Du, Phys. Rev. B **78**, 094511 (2008).

[28] I. A. Nekrasov, Z. V. Pchelkina, and M. V. Sadovskii, JETP Lett. **88**, 144 (2008).

[29] I. A. Nekrasov, Z. V. Pchelkina, and M. V. Sadovskii, JETP Lett. **88**, 543 (2008).

[30] A. Subedi, L. Zhang, D. J. Singh, and M. H. Du, Phys. Rev. B **78**, 134514 (2008).

[31] F. Ma, W. Ji, J. Hu, Z.-Y. Lu, and T. Xiang, Phys. Rev. Lett. **102**, 177003 (2009).

[32] T. Miyake, K. Nakamura, R. Arita, and M. Imada, J. Phys. Soc. Jpn. **79**, 0447105 (2010).

[33] I. I. Mazin, D. J. Singh, M. D. Johannes, and M. H. Du, Phys. Rev. Lett. **101**, 057003 (2008).

[34] K. Kuroki, S. Onari, R. Arita, H. Usui, Y. Tanaka, H. Kontani, and H. Aoki, Phys. Rev. Lett. **101**, 087004 (2008).

[35] K. Kuroki, S. Onari, R. Arita, H. Usui, Y. Tanaka, H. Kontani, and H. Aoki, New J. Phys. **11**, 025017 (2009).

[36] K. Kuroki, H. Usui, S. Onari, R. Arita, and H. Aoki, Phys. Rev. B **79**, 224511 (2009).

[37] K. Kuroki, Solid State Communications **152**, 711 (2012). Special Issue on Iron-based Superconductors.

[38] T. Nomura, J. Phys. Soc. Jpn. **78**, 034716 (2009).

[39] H. Ikeda, J. Phys. Soc. Jpn. **77**, 123707 (2008).

[40] H. Ikeda, R. Arita, and J. Kuneš, Phys. Rev. B **81**, 054502 (2010).

[41] F. Wang, H. Zhai, Y. Ran, A. Vishwanath, and D. H. Lee, Phys. Rev. Lett. **102**, 047005 (2009).

[42] S. Graser, T. A. Maier, P. J. Hirschfeld, and D. J. Scalapino, New J. Phys. **11**, 025016 (2009).

[43] T. A. Maier, S. Graser, D. J. Scalapino, and P. J. Hirschfeld, Phys. Rev. B **79**, 224510 (2009).

[44] Z. J. Yao, J. X. Li, and Z. D. Wang, New J. Phys. **11**, 025009 (2009).

[45] T. D. Stanescu, V. Galitski, and S. Das Sarma, Phys. Rev. B **78**, 195114 (2008).

[46] V. Cvetkovic and Z. Tesanovic, Europhys. Lett. **85**, 37002 (2009).

[47] K. Seo, B. A. Bernevig, and J. Hu, Phys. Rev. Lett. **101**, 206404 (2008).

[48] K. Sano and Y. Ōno, J. Phys. Soc. Jpn. **78**, 124706 (2009).

[49] R. M. Fernandes, A. V. Chubukov, and J. Schmalian, Nature Materials **10**, 97 (2014).

[50] H. Kontani and S. Onari, Phys. Rev. Lett. **104**, 157001 (2010).

[51] H. Kontani, T. Saito, and S. Onari, Phys. Rev. B **84**, 024528 (2011).

[52] Y. Yanagi, Y. Yamakawa, and Y. Ōno, Phys. Rev. B **81**, 054518 (2010).

[53] Y. Yanagi, Y. Yamakawa, N. Adachi, and Y. Ōno, Phys. Rev. B **82**, 064518 (2010).

[54] Y. Yanagi, Y. Yamakawa, N. Adachi, and Y. Ōno, J. Phys. Soc. Jpn. **79**, 123707 (2010).

[55] S. Onari and H. Kontani, Phys. Rev. Lett. **109**, 137001 (2012).

[56] S. Onari, H. Kontani, and M. Sato, Phys. Rev. B **81**, 060504 (2010).

[57] S. Onari and H. Kontani, Phys. Rev. Lett. **103**, 177001 (2009).

[58] Y. Ōno, Y. Yanagi, Y. Yamakawa, and N. Adachi, Solid State Communications **152**, 701 (2012).

[59] N. Bulut, D. J. Scalapino, and R. T. Scalettar, Phys. Rev. B **45**, 5577 (1992).

[60] K. Kuroki and R. Arita, Phys. Rev. B **64**, 024501 (2001).

[61] The frequency $\omega(\boldsymbol{q})$ of a phonon coupled to a quadrupole $O$ is renormalized as $\omega(\boldsymbol{q})/\omega^0(\boldsymbol{q}) = [\chi_O^{\rm irr}(\boldsymbol{q},0)/\chi_O(\boldsymbol{q},0)]^{1/2}$ and is expected to show a softening for $\boldsymbol{q} \sim \boldsymbol{Q}_{\rm AF}$ due to the enhancement of the AFO fluctuation as observed for the acoustic phonon softened for $\boldsymbol{q} \sim \boldsymbol{0}$ due to the FO fluctuation.

[62] T. Yamada, J. Ishizuka, and Y. Ōno, J. Phys. Soc. Jpn. **83**, 043704 (2014).

[63] C. Ma, L. Wu, W.-G. Yin, H. Yang, H. Shi, Z. Wang, J. Li, C. C. Homes, and Y. Zhu, Phys. Rev. Lett. **112**, 077001 (2014).

[64] Y. Yanagi, Y. Yamakawa, and Y. Ōno, J. Phys. Soc. Jpn **77**, 123701 (2008).

[65] S. Zhou, G. Kotoliar, and Z. Wang, Phys. Rev. B **84**, 14505 (2011).

[66] J. Ishizuka, T. Yamada, Y. Yanagi, and Y. Ōno, J. Phys. Soc. Jpn. **82**, 123712 (2013).

[67] D. C. Johnston, Adv. Phys **59**, 803 (2010).

[68] P. J. Hirschfeld, M. M. Korshunov, and I. I. Mazin, Rep. Prog. Phys **74**, 124508 (2011).

[69] J. H. Tapp, Z. Tang, B. Lv, K. Sasmal, B. Lorenz, P. C. W. Chu, and A. M. Guloy, Phys. Rev. B **78**, 060505(R) (2008).

[70] A. E. Taylor, M. J. Pitcher, R. A. Ewings, T. G. Perring, S. J. Clarke, and A. T. Boothroyd, Phys. Rev. B **83**, 220514 (2011).

[71] N. Qureshi, P. Steffens, Y. Drees, A. C. Komarek, D. Lamago, Y. Sidis, L. Harnagea, H.-J. Grafe, S. Wurmehl, B. Büchner, and M. Braden, Phys. Rev. Lett. **108**, 117001 (2012).

[72] J. Knolle, V. B. Zabolotnyy, I. Eremin, S. V. Borisenko, N. Qureshi, M. Braden, D. V. Evtushinsky, T. K. Kim, A. A. Kordyuk, S. Sykora, C. Hess, I. V. Morozov, S. Wurmehl, R. Moessner, and B. Büchner, Phys. Rev. B **86**, 174519 (2012).

[73] J. D. Wright, M. J. Pitcher, W. Trevelyan-Thomas, T. Lancaster, P. J. Baker, F. L. Pratt, S. J. Clarke, and S. J. Blundell, Phys. Rev. B **88**, 060401 (2013).

[74] P. Wiecki, B. Roy, D. C. Johnston, S. L. Bud'ko, P. C. Canfield, and Y. Furukawa, Phys. Rev. Lett. **115**, 137001 (2015).

[75] T. Saito, S. Onari, Y. Yamakawa, H. Kontani, S. V. Borisenko, and V. B. Zabolotnyy, Phys. Rev. B **90**, 035104 (2014).

[76] P. M. R. Brydon, M. Daghofer, C. Timm, and J. van den Brink, Phys. Rev. B **83**, 060501 (2011).

[77] Z. P. Yin, K. Haule, and G. Kotliar, Nat Phys. **10**, 845 (2014).

[78] F. Ahn, I. Eremin, J. Knolle, V. B. Zabolotnyy, S. V. Borisenko, B. Büchner, and A. V. Chubukov, Phys. Rev. B **89**, 144513 (2014).

[79] S. V. Borisenko, V. B. Zabolotnyy, A. A. Kordyuk, D. V. Evtushinsky, T. K. Kim, I. V. Morozov, R. Follath, and B. Büchner, Symmetry **4**, 251 (2012).

[80] Y. Nomura, K. Nakamura, and R. Arita, Phys. Rev. Lett. **112**, 027002 (2014).

[81] J. Ishizuka, T. Yamada, Y. Yanagi, and Y. 系o, Journal of the Physical Society of Japan **85**, 114709 (2016).

[82] A. Georges, G. Kotliar, W. Krauth, and M. J. Rozenberg, Rev. Mod. Phys **68**, 13 (1996).

[83] J. Ishizuka, T. Yamada, Y. Yanagi, and Y. Ōno, JPS Conf. Proc. **3**, 015020 (2014).

[84] L. de' Medici, S. R. Hassan, and M. Capone, J. Supercond. Nov. Magn. **22**, 535 (2009).

[85] L. de' Medici, S. R. Hassan, M. Capone, and X. Dai, Phys. Rev. Lett. **102**, 126401 (2009).

[86] F. Hardy, A. E. Böhmer, D. Aoki, P. Burger, T. Wolf, P. Schweiss, R. Heid, P. Adelmann, Y. X. Yao, G. Kotliar, J. Schmalian, and C. Meingast, Phys. Rev. Lett. **111**, 027002 (2013).

[87] M. Aichhorn, L. Pourovskii, and A. Georges, Phys. Rev. B **84**, 054529 (2011).

[88] H. Park, K. Haule, and G. Kotliar, Phys. Rev. Lett. **107**, 137007 (2011).

[89] T. Yamada, T. Kasai and Y. Ōno, unpublished.

[90] L. de' Medici, G. Giovannetti, and M. Capone, Phys. Rev. Lett. **112**, 177001 (2014).

[91] A. Koga, N. Kawakami, T. M. Rice, and M. Sigrist, Phys. Rev. B **72**, 045128 (2005).

[92] M. Ferrero, F. Becca, M. Fabrizio, and M. Capone, Phys. Rev. B **72**, 205126 (2005).

[93] G. Rohringer, A. Valli, and A. Toschi, Phys. Rev. B **86**, 125114 (2012).

[94] H. Kusunose, J. Phys. Soc. Jpn. **79**, 094707 (2010).

[95] T. Hänke, S. Sykora, R. Schlegel, D. Baumann, L. Harnagea, S. Wurmehl, M. Daghofer, B. Büchner, J. van den Brink, and C. Hess, Phys. Rev. Lett. **108**, 127001 (2012).

[96] M. P. Allan, A. W. Rost, A. P. Mackenzie, Y. Xie, J. C. Davis, K. Kihou, C. H. Lee, A. Iyo, H. Eisaki, and T.-M. Chuang, Science **336**, 563 (2012).

[97] C. Hess, S. Sykora, T. Hänke, R. Schlegel, D. Baumann, V. B. Zabolotnyy, L. Harnagea, S. Wurmehl, J. van den Brink, and B. Büchner, Phys. Rev. Lett. **110**, 017006 (2013).

[98] Z. Li, Y. Ooe, X.-C. Wang, Q.-Q. Liu, C.-Q. Jin, M. Ichioka, and G.-Q. Zheng, J. Phys. Soc. Jpn. **79**, 083702 (2010).

[99] P. Jeglič, A. Potočnik, M. Klanjšek, M. Bobnar, M. Jagodič, K. Koch, H. Rosner, S. Margadonna, B. Lv, A. M. Guloy, and D. Arčon, Phys. Rev. B **81**, 140511 (2010).

[100] S.-H. Baek, L. Harnagea, S. Wurmehl, B. Büchner, and H.-J. Grafe, J. Phys.: Condens. Matter **25**, 162204 (2013).

[101] P. Morel and P. W. Anderson, Phys. Rev. **125**, 1263 (1962).

[102] Y. Takada, J. Phys. Soc. Jpn. **78**, 013703 (2009).

[103] Y. Mizuguchi, F. Tomioka, S. Tsuda, T. Yamaguchi, and Y. Takano, J. Phys. Soc. Jpn. **78**, 074712 (2009).

[104] M. D. Watson, T. K. Kim, A. A. Haghighirad, S. F. Blake, N. R. Davies, M. Hoesch, T. Wolf, and A. I. Coldea, Phys. Rev. B **92**, 121108 (2015).

[105] Y. Kawasaki, K. Deguchi, S. Demura, T. Watanabe, H. Okazaki, T. Ozaki, T. Yamaguchi, H. Takeya, and Y. Takano, Solid State Communications **152**, 1135 (2012).

[106] S. Medvedev, T. M. McQueen, I. Trojan, T. Palasyuk, M. I. Eremets, R. J. Cava, S. Naghavi, F. Casper, V. Ksenofontov, G. Wortmann, and C. Felser, Nature Materials **8**, 630 (2009).

[107] T. Urata, Y. Tanabe, K. K. Huynh, Y. Yamakawa, H. Kontani, and K. Tanigaki. arXiv:1508.04605.

[108] Y. Gallais, R. M. Fernandes, I. Paul, L. Chauvière, Y.-X. Yang, M.-A. Méasson, M. Cazayous, A. Sacuto, D. Colson, and A. Forget, Phys. Rev. Lett. **111**, 267001 (2013).

[109] A. E. Böhmer, T. Arai, F. Hardy, T. Hattori, T. Iye, T. Wolf, H. v. Löhneysen, K. Ishida, and C. Meingast, Phys. Rev. Lett. **114**, 027001 (2015).

[110] S. Mukherjee, A. Kreisel, P. J. Hirschfeld, and B. M. Andersen, Phys. Rev. Lett. **115**, 026402 (2015).

[111] J. Maletz, V. B. Zabolotnyy, D. V. Evtushinsky, S. Thirupathaiah, A. U. B. Wolter, L. Harnagea, A. N. Yaresko, A. N. Vasiliev, D. A. Chareev, A. E. Böhmer, F. Hardy, T. Wolf, C. Meingast, E. D. L. Rienks, B. Büchner, and S. V. Borisenko, Phys. Rev. B **89**, 220506 (2014).

[112] T. Shimojima, Y. Suzuki, T. Sonobe, A. Nakamura, M. Sakano, J. Omachi, K. Yoshioka, M. Kuwata-Gonokami, K. Ono, H. Kumigashira, A. E. Böhmer, F. Hardy, T. Wolf, C. Meingast, H. v. Löhneysen, H. Ikeda, and K. Ishizaka, Phys. Rev. B **90**, 121111 (2014).

[113] Y. Yamakawa, S. Onari, and H. Kontani, Phys. Rev. X **6**, 021032 (2016).

[114] S. Onari, Y. Yamakawa, and H. Kontani, Phys. Rev. Lett. **116**, 227001 (2016).

[115] A. Lieabsch and H. Ishida, Phys. Rev. B **82**, 155106 (2010).

[116] M. Aichhorn, S. Biermann, T. Miyake, A. Georges, and M. Imada, Phys. Rev. B **82**, 064504 (2010).

[117] Z. P. Yin, K. Haule, and G. Kotliar, Phys. Rev. B **86**, 195141 (2012).

[118] M. Hirayama, T. Miyake, and M. Imada, Phys. Rev. B **87**, 195144 (2013).

[119] N. Marzari and D. Vanderbilt, Phys. Rev. B **56**, 12847 (1997).

[120] I. Souza, N. Marzari, and D. Vanderbilt, Phys. Rev. B **65**, 035109 (2001).

[121] A. A. Mostofi, J. R. Yates, Y.-S. Lee, I. Souza, D. Vanderbilt, and N. Marzari, Computer Physics Communications **178**, 685 (2008).

[122] J. Kuneš, R. Arita, P. Wissgott, A. Toschi, H. Ikeda, and K. Held, Computer Physics Communications **181**, 1888 (2010).

[123] P. Blaha, K. Schwarz, G. Madsen, D. Kvasnicka, and J. Luitz, WIEN2k, An Augmented Plane Wave + Local Orbitals Program for Calculating Crystal Properties (Tech. Univ. Wien, Vienna, 2001).

[124] We used the full-potential linearized augmented plane-wave method within the generalized gradient approximation as implemented in the WIEN2k code. [123] The maximum reciprocal lattice vector $K_{max}$ was chosen as $R_{\mathrm{MT}}K_{\mathrm{max}} = 7.0$ and $25\times25\times15$ $k$-points sampling was used for the self-consistent calculation.

[125] V. I. Anisimov, F. Aryasetiawan, and A. I. Lichtenstein, Journal of Physics: Condensed Matter **9**, 767 (1997).

[126] R. Thomale, C. Platt, W. Hanke, and B. A. Bernevig, Phys. Rev. Lett. **106**, 187003 (2011).

[127] X. C. Wang, Q. Q. Liu, Y. X. Lv, W. B. Gao, L. X. Yang, R. C. Yu, F. Y. Li, and C. Q. Jin, Solid State Commun. **148**, 538 (2008).

[128] F. Krüger, S. Kumar, J. Zaanen, and J. van den Brink, Phys. Rev. B **79**, 054504 (2009).

[129] T. Imai, K. Ahilan, F. L. Ning, T. M. McQueen, and R. J. Cava, Phys. Rev. Lett. **102**, 177005 (2009).

[130] M. Bendele, A. Amato, K. Conder, M. Elender, H. Keller, H.-H. Klauss, H. Luetkens, E. Pomjakushina, A. Raselli, and R. Khasanov, Phys. Rev. Lett. **104**, 087003 (2010).

[131] M. Bendele, A. Ichsanow, Y. Pashkevich, L. Keller, T. Strässle, A. Gusev, E. Pomjakushina, K. Conder, R. Khasanov, and H. Keller, Phys. Rev. B **85**, 064517 (2012).

[132] T. Terashima, N. Kikugawa, S. Kasahara, T. Watashige, T. Shibauchi, Y. Matsuda, T. Wolf, A. E. Böhmer, F. Hardy, C. Meingast, H. v. Löhneysen, and S. Uji, J. Phys. Soc. Jpn. **84**, 063701 (2015).

[133] K. Miyoshi, K. Morishita, E. Mutou, M. Kondo, O. Seida, K. Fujiwara, J. Takeuchi, and S. Nishigori, J. Phys. Soc. Jpn. **83**, 013702 (2014).

[134] K. Kothapalli, A. E. Böhmer, W. T. Jayasekara, B. G. Ueland, P. Das, A. Sapkota, V. Taufour, Y. Xiao, E. E. Alp, S. L. Bud'ko, P. C. Canfield, A. Kreyssig, and A. I. Goldman. arXiv:1603.04135.

[135] T. Terashima, N. Kikugawa, A. Kiswandhi, D. Graf, E.-S. Choi, J. S. Brooks, S. Kasahara, T. Watashige, Y. Matsuda, T. Shibauchi, T. Wolf, A. E. Böhmer, F. Hardy, C. Meingast, H. v. Löhneysen, and S. Uji, Phys. Rev. B **93**, 094505 (2016).

[136] P. Wang, S. Sun, Y. Cui, W. Song, T. Li, R. Yu, H. Lei, and W. Yu. arXiv:1603.04589.

[137] S. Margadonna, Y. Takabayashi, Y. Ohishi, Y. Mizuguchi, Y. Takano, T. Kagayama, T. Nakagawa, M. Takata, and K. Prassides, Phys. Rev. B **80**, 064506 (2009).

[138] We introduce the intra-orbital hopping parameters $(\delta\varepsilon_{xy}, \delta t_{xy}^{\rm nn}, \delta t_{xy}^{\rm nnn}) = (-0.025, +0.0125, -0.06625)$ [eV] into tight-binding Hamiltonian obtained by maximally localized Wannier functions, which is corresponding to the energy shift of $xy$ orbital band with $(\delta E_\Gamma, \delta E_{\rm M}, \delta E_{\rm X}) = (-0.24, -0.34, +0.24)$ [eV] for unfolded Brillouin zone. We also introduce the intra-orbital hopping parameters $(\delta\varepsilon_{zx/yz}, \delta t_{zx/yz}^{\rm nn}, \delta t_{zx/yz}^{\rm nnn}) = (0, -0.03, -0.03)$ [eV], where the energy shift of $zx/yz$ orbital band is $(\delta E_\Gamma, \delta E_{\rm M}, \delta E_{\rm X}) = (-0.24, 0, +0.12)$ [eV]. These parameters are determined so as to reproduce the ARPES experiment [19].

[139] H. Usui and K. Kuroki, Physica C: Superconductivity **470, Supplement 1**, S382 (2010).

[140] Y. Yamakawa. private communication.